

**DETERMINATION OF FORMING LIMIT CURVES OF STEEL PIPES FOR  
HYDROFORMABILITY EVALUATION OF AUTOMOTIVE PARTS**

**RAMIL KESVARAKUL**



**A THESIS SUBMITTED IN PARTIAL FULFILLMENT  
OF THE REQUIREMENT FOR THE DEGREE OF  
MASTER OF ENGINEERING IN AUTOMOTIVE ENGINEERING  
(INTERNATIONAL PROGRAM)  
INTERNATIONAL COLLEGE  
KING MONGKUT'S INSTITUTE OF TECHNOLOGY LADKRABANG**

**2010**

**KMITL-2010-IC-M-004-007**



**COPYRIGHT 2010**

**INTERNATIONAL COLLEGE**

**KING MONGKUT'S INSTITUTE OF TECHNOLOGY LADKRABANG**

**NATIONAL SCIENCE AND DEVELOPMENT AGENCY**

This material is reserved for educational use only, not allowed for commercial use.

Forbidden to modify the content, and cite the document when use.

**Thesis Title:** Determination of forming limit curves of steel pipes for hydroformability evaluation of automotive parts

**Student:** Ramil Kesvarakul

**Student ID:** 51061914

**Degree:** Master of Engineering

**Programme:** Automotive Engineering

**Year:** 2010

**Thesis Advisor:** Dr. Monsak Pimsarn  
Dr. Suwat Jirathearanat  
Assoc.Prof. Naoto Ohtake

### ABSTRACT

The aims of this research are to establish the forming limit curve (FLC) of tubular material low carbon steels commonly used in Thai industry, verify these FLCs with real part forming experiments, and compare these experimentally obtained FLCs against analytical ones available in FEA software database. A self-designed bulge forming apparatus of fixed bulge length and a hydraulic test machine with axial feeding are used to carry out the bulge tests. Loading paths resulting to linear strain paths at the apex of the bulging tube are determined by FE simulations in conjunction with a self-compiled subroutine. These loading paths are used to control the internal pressure and axial feeding punch of the test machine. In this work a common low carbon steel tubing grade STKM 11A, with 28.6 mm outer diameter and 1.2 mm thick is studied. Circular grids are electro chemically etched onto the surface of tube samples. Subsequently, the tube samples are bulge-formed. The forming process is stopped when a burst is observed on the forming sample. After conducting the bulge tests, major and minor strains of the grids located beside the bursting line on the tube surface are measured to construct the forming limit curve (FLC) of the tubes. The forming limit curves determined for these tubular materials are put to test in formability evaluations of test parts forming in real experiment.

It was found that the tool geometry can keep the strain ratio constant is not dependent on the thickness but only on OD of the tube, as in equations  $L = OD$  and  $r_d = \frac{15 \times OD}{25.4}$ . The experimental FLDs have predicted failures in forming process consistently with the real experiments. The experimentally obtained forming limit curves (determined following STKM 11A) differ from

This material is reserved for educational use only, not allowed for commercial use.

Forbidden to modify the content, and cite the document when use.

empirical one (from FEA software) and analytical one by about 0.02339 and 0.15736 true strain respectively at  $FLD_0$ , the corresponding plane strain values.

## **ACKNOWLEDGEMENT**

This thesis could not be completed without the assistance of many persons to whom I would like to express my sincere appreciation.

First, I would like to sincerely thank my advisor, Dr. Suwat Jirathearanat, who has given me many helpful suggestions, useful advice during the undertaken research.

I would also like to sincerely thank Asst. Prof. Dr.Monsak Pimsarn for kind advising and helping, and Assoc. Prof. Naoto Ohtake for the suggestion of oxide analysis.

Moreover, I would like to show gratitude to the National Metal and Materials Technology Center (MTEC) laboratory for providing the laboratory equipments and instruments as well as financial supporting.

I am grateful to the National Science and Technology Development Agency (NSTDA), which provided the full scholarship for studying in the master program.

Finally, I am very grateful to my family for all love, caring, understanding and motivation throughout my life.

**Ramil Kesvarakul**

# CONTENTS

	Page
ABSTRACT.....	I
ACKNOWLEDGMENTS.....	II
CONTENTS.....	III
LIST OF TABLES.....	VII
LIST OF FIGURES.....	VIII
 <b>CHAPTER 1 INTRODUCTION</b>	
1.1 Significance and Background.....	1
1.2 Objectives.....	2
1.3 Scopes.....	2
1.4 Expected Results.....	2
 <b>CHAPTER 2 THEORY AND LITERATURE REVIEWS</b>	
2.1 Introduction to Tube Hydroforming (THF).....	3
2.2 Material Property.....	5
2.2.1 Stress.....	5
2.2.2 Strain.....	5
2.2.3 Tensile Test.....	6
2.2.4 The Engineering Stress-Strain Curve.....	6
2.2.5 Anisotropy.....	9
2.3 Tubular blank.....	10
2.4 Strain-based forming limit curve.....	11
2.4.1 Formulation of plastic instability criteria.....	14
2.4.2 FLC obtained by Finite Element software: DYNAFORM.....	20
2.5 Ductile fracture criterion.....	21
2.6 Effect of non-linearity of strain path.....	24

This material is reserved for educational use only, not allowed for commercial use.

Forbidden to modify the content, and cite the document when use.

## CONTENTS (CONT.)

Page

### CHAPTER 3 RESEARCH METHODOLOGY

3.1 Numerical Investigation.....	27
3.1.1 Test die insert design.....	27
3.1.2 Determination of loading paths by FE-simulations.....	31
3.2 Experimental Investigation .....	36
3.2.1 FLC testing apparatus.....	36
3.2.2 THF Test Specimens.....	37
3.2.3 Hydraulic press.....	38
3.2.4 Pressure system, Hydraulic cylinders and punches.....	39
3.3 Grid measurement.....	39
3.3.1 Digital Microscope.....	39
3.3.2 Grid Curvature.....	40

### CHAPTER 4 EXPERIMENTATION AND RESULTS

4.1 Tube Hydraulic Bulge Test.....	43
4.1.1 Forming limit experiments with axial feeding.....	44
4.1.2 Forming limit experiments without axial feeding.....	49
4.1.3 Forming limit of welded seam.....	51
4.2 Grid Measurement.....	52
4.3 Construction of the Forming Limit Curve(FLC).....	53

### CHAPTER 5 COMPARISON AND VERIFICATION

5.1 Empirical FLC, Analytical FLC and Experimental FLC.....	59
5.2 Verification of Experimental FLC.....	62
5.2.1 Verification of Experimental FLC with actual bulge test load path.....	62
5.2.2 Verification of Experimental FLC with a real automotive part.....	64

This material is reserved for educational use only, not allowed for commercial use.

Forbidden to modify the content, and cite the document when use.

## CONTENTS (CONT.)

	Page
<b>CHAPTER 6 CONCLUSION AND SUGGESTIONS</b>	
6.1 Conclusions.....	66
6.2 Suggestions for Future Work.....	67
<b>REFERENCES</b> .....	68
<b>APPENDIX</b> .....	70
Appendix A: International Conference: Determination of forming limit curves of tubular materials for hydroformability evaluation of automotive parts.....	70
Appendix B: Determination of forming limit curves of tubular.....	79
Appendix C: Tooling schematic.....	87
<b>BIOGRAPHY</b> .....	95

### LIST OF TABLES

Table	Page
3.1 Design of simulation matrix.....	28
3.2 A series of simulation.....	29
3.3 Simulation results.....	29
3.4 A series of simulation, $L/OD=1$ and $rd/t=15$ .....	30
3.5 Result of Simulation, $L/OD=1$ and $rd/t=15$ .....	31
4.1 Grid curvature.....	52

### LIST OF FIGURES

Figures	Page
2.1 Schematic illustration of the hydroforming of a bulge in a tube.....	3
2.2 Example tube hydroformed parts: a 2004 Ford F-150, chassis frame.....	4

This material is reserved for educational use only, not allowed for commercial use.

Forbidden to modify the content, and cite the document when use.

## LIST OF FIGURES (CONT.)

Figures	Page
2.3 Components of stress on element (Hosford and Caddell, 2007).....	5
2.4 Typical tensile specimen (Marciniak et al., 2002).....	6
2.5 Load-extension diagram for tensile test (Marciniak et al., 2002).....	6
2.6 Engineer stress-strain curve (Marciniak, Z.et al. 2002).....	7
2.7 The elastic behavior of typical tensile test (Marciniak, Z.et al. 2002).....	8
2.8 Diagram used to determine the proof stress in a material (Marciniak, Z.et al. 2002).....	8
2.9 Measurement of r value by tensile specimen from three directions (ASTM, 1998).....	9
2.10 Electric resistance welded pipe process. (PIPING HANDBOOK, 2000).....	10
2.11 Electric Resistance Welding (ERW) Tube.....	11
2.12 Three basic zones - red, yellow, and green of Forming limit diagram.....	12
2.13 FLD with different principle strain ratio.....	12
2.14 Schematic figure of the subtangent of a stress strain curve as necking occurs. (Yeong-Maw Hwang. 2009).....	15
2.15 Flow chart for determining the critical major and minor principal strains.....	18
2.16 The forming limit curve and yield locus with Hill's non-quadratic yield function.....	19
2.17 The forming limit curve with Keeler's formula.....	20
2.18 Forming limit diagram obtained experimentally for a STKM-11A tube (Li-Ping Lei, 2002).....	22
2.19 Variations of $\sigma_m/\bar{\sigma}$ and $d\bar{\epsilon}/d\epsilon_1$ with respect to strain ratio $\beta$ (Li-Ping Lei, 2002).....	23
2.20 Determination of C1 and C2 for a STKM-11A tube (Li-Ping Lei, 2002).....	23
2.21 Influence of strain path on the FLC (adapted from Graf and Hosford, 1993).....	24
3.1 Schematic diagram of the test die insert parameters.....	27
3.2 The formed part show in half model.....	28
3.3 testing die insert geometry.....	31
3.4 Feeding distance (mm) with time(s).....	32
3.5 Internal Pressure (bar) with time (s).....	33
3.6 Feeding distance (mm) with Internal Pressure (bar).....	34
3.7 Simulation results with four strain ratios ( $\xi = \epsilon_2/\epsilon_1$ ) -0.1, -0.2, -0.3, -0.4 and no feeding.....	35

This material is covered by educational use only, not allowed for commercial use.

Forbidden to modify the content, and cite the document when use.

## LIST OF FIGURES (CONT.)

Figures	Page
3.8 Different strain paths investigated.....	36
3.9 The experimental apparatus for bulge tests without axial feeding.....	36
3.10 The experimental apparatus for bulge tests with axial feeding.....	37
3.11 Schematic diagram of the experimental apparatus for bulge tests.....	37
3.11 Circular grids with a diameter of 2.5mm.....	38
3.12 THF Test Specimens.....	38
3.13 Hydraulic press and CNC controller.....	38
3.14 CNC controller used to control internal pressure and axial punches.....	39
3.15 Digital Microscope (Dino-Lite).....	39
3.16 The deformed grids measured using Dino Capture Software.....	40
3.17 $r_{\phi P}$ is meridian radius of curvature at the pole.....	40
3.18 $r_{\theta P}$ is circumferential radius of curvature at the pole.....	40
3.19 A photo of bulged tube for curvature measurement.....	41
3.20 Approximation of the curve by CAD software.....	41
4.1 Apparatus with feeding tooling set.....	42
4.2 Apparatus without feeding tooling set.....	42
4.3 Loading path, Feeding distance (mm) and Internal pressure (bar) with time(s).....	43
4.4 Loading path, Feeding distance (mm) with Internal Pressure (bar).....	43
4.5 Loading path, Feeding distance (mm) with Internal Pressure (bar).....	44
4.6 Results of the formed product for different strain paths.....	44
4.7 loading path and Results of the formed product of different deformed state-Set1.....	45
4.8 loading path and Results of the formed product of different deformed state-Set2.....	46
4.9 loading path and Results of the formed product of different deformed state-Set3.....	47
4.10 loading path and Results of the formed product of different deformed state-Set4.....	48
4.11 Loading path, Internal Pressure (bar) with times(s).....	49
4.12 Results of the formed product without axial feeding.....	49
4.13 loading path and Results of the formed product of different deformed state-Set5.....	50
4.14 The specimens that burst at welded seam and corresponding load path.....	51
4.15 Measure zone covering $\pm 45$ degrees from welding seam.....	53

This material is reserved for educational use only, not allowed for commercial use.

Forbidden to modify the content, and cite the document when use.

## LIST OF FIGURES (CONT.)

Figures	Page
4.16 FLC with the major and minor strains of all specimens covering $\pm 45$ degrees from welding seam.....	52
4.17 The major and minor strain with degree from welding line of Set4.....	54
4.18 Set1 strain path at 30 degree.....	55
4.19 Set2 strain path at 20 degree.....	56
4.20 Set3 strain path at 22.5 degree.....	56
4.21 Set4 strain path at 27.5 degree.....	57
4.22 Set5 strain path at 25 degree.....	57
4.23 The Experimental FLD and forming limit curves (FLC) of STKM 11A tubes.....	58
5.1 Comparison of predicted forming limit strains with the experimental forming limit strains for low carbon steels STKM 11A.....	59
5.2 Effects of the r value on the forming limit curve with Hill's non-quadratic yield function.....	60
5.3 Effects of the n value on the forming limit curve with Hill's non-quadratic yield function.....	60
5.4 Effects of the t value on forming limit curve with Keeler's formula.....	61
5.5 Effects of the n value on the forming limit curve with Keeler's formula.....	62
5.6 Results of Comparison for experiment and numerical simulation.....	63
5.7 A fuel filler pipe geometry.....	64
5.8 A final product of fuel filler pipe.....	64
5.9 A simulation model of fuel filler pipe.....	65
5.10 Comparison of predicted forming limit strains with measured experimental data.....	65

This material is reserved for educational use only, not allowed for commercial use.

Forbidden to modify the content, and cite the document when use.

# CHAPTER 1

## INTRODUCTION

### 1.1 Significance and Background

Transportation of people and goods has always been one of the sectors that consume most of energy resources and continuing to increase the consumption level at a rapid rate. Design and production of high strength-to-weight ratioed automotive parts is now encouraged or even enforced in most developed countries. Tube hydroforming technology is a promising new forming process that produces tubular automotive parts with significant weight reduction.

Tube hydroforming is a tubular material-forming process that uses a pressurized fluid in place of hard tooling, i.e. punch, to plastically deform a given blank material into a desired shape. With this technique, more complex shapes with increased strength and reduced weight can be manufactured as compared with stamping, forging or casting processes.

The forming limit diagram (FLD) of tubular materials should be established, because it clearly shows the formability of the hydraulic forming processes. A few studies concerning the loading paths or the forming limit of tubes and sheets have been reported. For example, Jieshi Chen (2009) study Sheet metal forming limit prediction based on plastic deformation energy, the sheet metal forming limit is calculated by fitting curve from experimental data. The forming limit curves determined for these sheet materials were put to test in formability evaluations of test parts forming in both real experiment and numerical simulation that in this study he selected sheet material ST14 with 0.8 and 0.85 mm thick. Yeong-Maw Hwang (2008) used bulge tests to establish the forming limit diagram (FLD) of tubular material AA6011. Then he compared it with the forming limits from analytical FLCs using the  $n$  values obtained by tensile tests and bulge tests. E. Chu and Yu Xu (2008) showed work done by investigators who investigated the prediction of forming limit diagrams (FLDs) for tube hydroforming of 6061-T4 seamless extruded tubes.

From the literatures reviewed, it is clear that experimental determination of FLC using a hydraulic bulging tube apparatus is necessary for accurate tube hydroforming part and process design. So far, a consistent conclusion for forming limit theorems of tubular materials has not been established and the forming limit diagram for STKM 11A tubes has not been found.

This material is reserved for educational use only, not allowed for commercial use.

Forbidden to modify the content, and cite the document when use.

Therefore, this work aims to develop a capability to experimentally determine forming limit curves (FLC) of tubular materials available in Thailand. In this work, hydraulic forming machines are developed, experiments of bulge tests with and without axial feeding are carried out, loading paths leading to the linear strain paths at the pole of the forming tube are determined by FEA and are used to control the internal pressure and axial feeding in the forming limit experiments. The experimentally obtained forming limits are later compared with some analytical and empirical FLCs. A commonly available low carbon steel tubing, STKM 11A, is chosen to be the target material in this study.

## 1.2 Objectives

- 1.2.1 To design a tube bulge forming apparatus to carry out tube hydraulic bulge test.
- 1.2.2 To determine the forming limit curve (FLC) of tubular material low carbon steels commonly used in Thai industry
- 1.2.3 To verify the forming limit curve (FLC) with real part forming experiments for actual applications.

## 1.3 Scopes

- 1.3.1 The designed bulge forming apparatus is to be used with MTEC hydroforming system, maximum pressure 1000 bars, 200 tons hydraulic press.
- 1.3.2 The test tooling is to be designed for a material low carbon steel tubing commonly used in Thai industry, namely STKM 11A with 1.2 mm thickness and 28.6 mm outer diameter.
- 1.3.3 Finite element software (DYNAFORM) is to be used for design tooling and loading curve.
- 1.3.4 A real tubular part hydroforming experiments (Fuel filler) is to be used to verify FLCs

## 1.4 Expected Benefits

- 1.4.1 Being able to use the forming limit curve (FLC) for tubular formability evaluations accurately.
- 1.4.2 Useful the forming limit curve (FLC) that can be used to further develop THF processes in the automotive industries.

## CHAPTER 2

# LITERATURE REVIEWS

### 2.1 Introduction to Tube Hydroforming (THF)

Tube hydroforming is a tubular material-forming process that uses a pressurized fluid in place of hard tooling, i.e. punch, to plastically deform a given blank material into a desired shape as depicted in Figure 2.1. During a hydroforming process, a tube is placed in the closed cavity of a forming die. The ends of the tube are sealed by the axial punches. The axial punches are necessary to seal the end of the tube to avoid pressure losses and to feed material into expansion regions. After the ends of the tube are sealed, the hydraulic fluid is injected into the inner of the tube and the tube is formed to conform the shape of the die cavity. They should feed the material into the deformation zone in a controlled way, and in synchronization with internal pressure, i.e. pressure versus time and axial force versus time should be controlled and coordinated. Tube hydroforming process has drawn increasing attention in the automotive industries due to its several advantages comparing with the conventional forming process (stamping, forging or casting processes), such as reduction of the weight of components and overall number of processes and more complex shapes with increased strength as show in Figure 2.2.

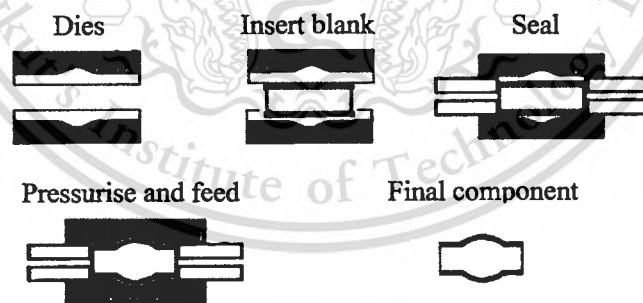


**Figure 2.1** Schematic illustration of the hydroforming of a bulge in a tube

The first patented hydroforming application was obtained by Milton Garvin of the Schaible Company of Cincinnati, Ohio, for producing kitchen spouts in the 1950s. Since the 1990s, hydroforming has made an impactful comeback due to the advancements in computer controls, hydraulic systems and recently developed process and part design guidelines, and various forged or stamped structural parts have been replaced by parts formed with tube

This material is reserved for educational use only, not allowed for commercial use.

Forbidden to modify the content, and cite the document when use.

hydroforming technology (THF). Substantial weight and cost savings were realized with hydroformed steel parts because of the part consolidation, less post-forming processes (i.e., joining such as welding and piercing) and initial thinner material thickness opportunities (Dohmann, 1991; Koç, 2001; Murray, 1996 and Morphy, 1997).

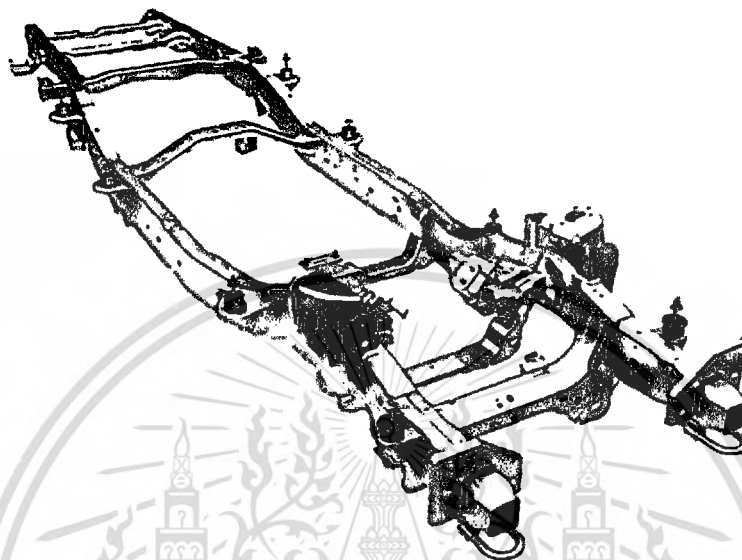


**Figure 2.2** Example tube hydroformed parts: a 2004 Ford F-150, chassis frame

In this study, focus is placed on the straight tube hydroforming process. In the straight tube hydroforming process, axial force is always applied at the ends of the tube simultaneously with the internal hydraulic pressure. Therefore, the material is fed into the deformation zone during the forming process more expansion and less thinning. For the straight tube hydroforming process, three characteristic failure modes, i.e., buckling, wrinkling, and bursting, are involved. Buckling failure, which induces if high axial force acts on the beginning of the process, is a function of the tube parameters and it is easy to be estimated in theoretical terms. Wrinkling failure, which occurs in the expansion zone if the axial feeding is too high, sometimes can be eliminated again by increasing the internal pressure during the final stage of the hydroforming process. Bursting failure occurs as a result of excessive high internal pressure. By contrast with buckling and wrinkling failure, bursting failure is irrecoverable. In order to obtain the final sound hydroformed product, it is necessary to study the forming limit diagram of the straight tube hydroforming process to optimize the forming process, and to reduce and finally eliminate the costly die try-out in hydroforming process design.

## 2.2 Material property

For the sheet material, the ability to transform shaped, it called “formability”, should also be considered. To assess formability, we can know behavior of the sheet from mechanical tests. In sheet metal forming, we are interest two principles that are elastic and plastic deformation.

### 2.2.1 Stress

Stress is define as force,  $F$ , at a point

$$\sigma = \frac{F}{A} \quad (2.1)$$

Where  $A$  is the area at force action

In Figure 2.3 as show the components of stress. The normal stress is the force acting normal to the plane. It may be tensile or compressive. The shear stress component is the force acts parallel to the plan (Hosford and Caddell, 2007).

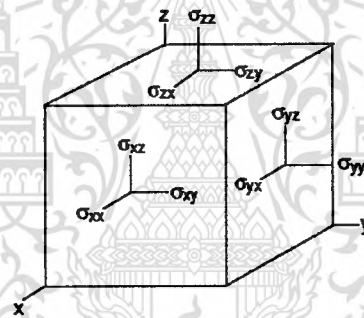


Figure 2.3 Components of stress on element (Hosford and Caddell, 2007).

### 2.2.2 Strain

Strain is total deformation in body, when the points in body are displaced by deformation, which can be divided 2 types that are elastic strain and plastic strain. The elastic strain means when the shape is deformed no force acting, element in body will move back to origin shape. But for the plastic strain when unloading material holds permanent deformation. We identify the plastic deformation by equation (2.2)

$$\varepsilon = \ln \frac{l}{l_0} \quad (2.2)$$

Where  $l =$  Final length

$l_0 =$  Original length

### 2.2.3 Tensile Test

This is typical of a number of standard test specimens. A tensile test specimen is shown in Figure 2.4. The initial thickness is  $t_0$  and the length of tensile test specimen that is a smallest amount four times the width,  $w_0$ . The load on the specimen,  $F$ , is measured by a load cell in the testing machine. The gauge length  $l_0$  is monitored by an extensometer in the middle of the specimen and the change in width is measured by a transverse extensometer. During the test, load and extension will be recorded in a data acquisition system. (Marciniak et al., 2002).

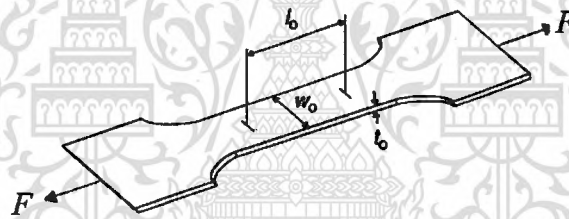
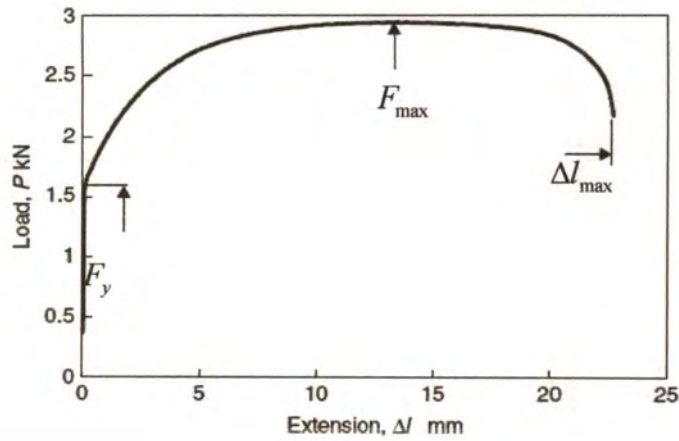


Figure 2.4 Typical tensile specimen (Marciniak et al., 2002).

### 2.2.4 The Engineering Stress-Strain Curve

Figure 2.5 shows load-extension diagram for a tensile test. The elastic extension is so small that it can't be seen. The initial yield load,  $F_y$ , is plastic deformation commence begin. During this part of the test, the cross-sectional area of specimen decreases while the length increases; the load maximum,  $F_{max}$ , was a point reached when the strain-hardening effect balanced the rate of decrease in area.



**Figure 2.5** Load-extension diagram for tensile test (Marciniak et al., 2002).

The engineering stress-strain curve obtained by the initial cross-sectional area,  $A_0 = w_0 \cdot t_0$ , and the extension by  $l_0$ . The engineering stress-strain curve is still widely used and a number of properties are derived from it. Figure 2.6 shows the engineering stress strain curve calculated from the load, extension diagram

Engineering stress can be calculated by this equation

$$\sigma_{eng} = \frac{F}{A_0} \quad (2.3)$$

And engineering strain as

$$e_{eng} = \frac{\Delta l}{l_0} \times 100\% \quad (2.4)$$

In Figure 2., the initial yield stress is

$$(\sigma_f)_0 = \frac{F_y}{A_0} \quad (2.5)$$

The maximum of engineering stress is called tensile strength and calculated as

$$TS = \frac{P_{max}}{A_0} \quad (2.6)$$

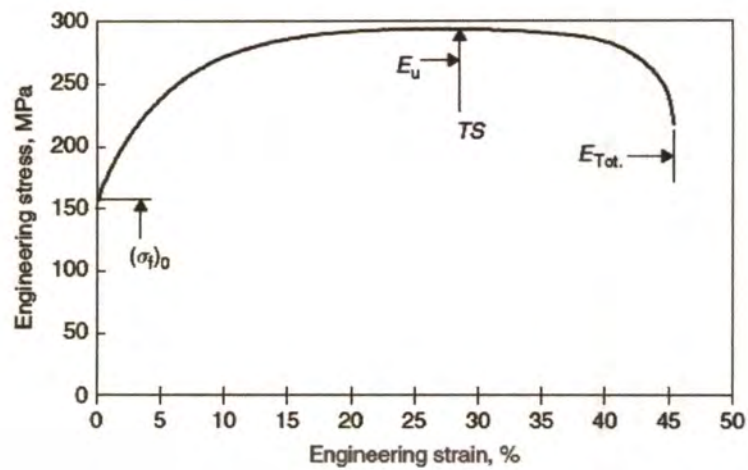


Figure 2.6 Engineer stress-strain curve (Marciniak, Z. et al. 2002).

The maximum uniform elongation,  $E_u$ , is the elongation at maximum load at maximum load as the cross-sectional area is no longer  $A_0$ .

If the strain scale near the origin is greatly increased, the elastic part of the curve would be seen, as shown in Figure 2.7. The strain at initial yield,  $e_y$ , is very small, typically about 0.1%. The slope of the elastic part of the curve is the elastic modulus, also called Young's modulus:

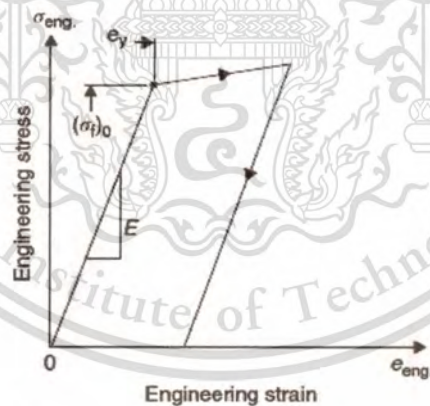


Figure 2.7 The elastic behavior of typical tensile test (Marciniak, Z. et al. 2002).

In some materials, the transition from elastic to plastic deformation is not sharp and it is difficult to establish an accurate yield stress. This is the stress to produce a specified small plastic strain 0.2%, i.e. the elastic strain at yield. Proof stress is determined by drawing a

line parallel to the elastic loading line which is offset by the specified amount, as shown in Figure 2.8.

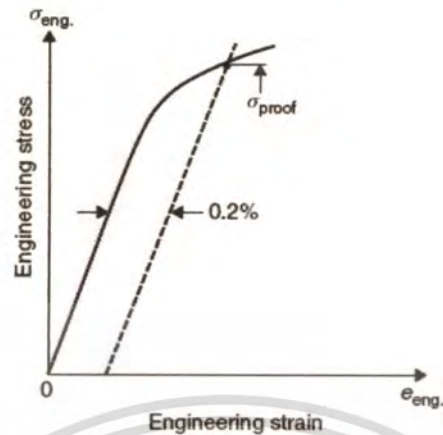


Figure 2.8 Diagram used to determine the proof stress in a material (Marciniak, Z. et al. 2002).

### 2.2.5 Anisotropy

In the principles of Anisotropy properties of the material is not equal in all directions. Therefore the values of  $r$  necessary to average in each direction ( $0^\circ$ ,  $45^\circ$ ,  $90^\circ$ ) as shown in Figure 2.9 and the  $r$  value in each direction will be average to use.

$$\bar{R} = \frac{R_0 + 2R_{45} + R_{90}}{4} \quad (2.7)$$

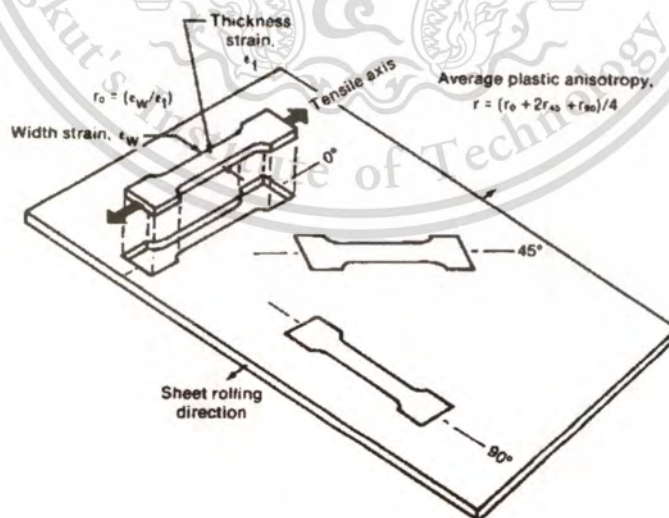


Figure 2.9 Measurement of  $r$  value by tensile specimen from three directions (ASTM, 1998).

### 2.3 Tubular blank

Tubing and Pipe are considered to be separate products, although geometrically they are quite similar. “Tubular products” infers cylindrical products which are hollow, and the classification of “pipe” or “tube” is determined by the end use. ASTM and the American Petroleum Institute (API) provide specifications for the many categories of pipe according to the end use. Other classifications within the end use categorization refer to the method of manufacture of the pipe or tube, such as seamless, cast, and electric resistance welded. Pipe and tube designations may also indicate the method of final finishing, such as hot finished and cold finished.

Structural tubing is used for general structural purposes related to the construction industry. ASTM provides specifications for this type of tubing. Mechanical tubing is produced to meet particular dimensional, chemical, and mechanical property and finish specifications which are a function of the end use, such as machinery and automotive parts. This category of tubing is available in welded (ERW) and seamless form.

In the electric resistance-welded (ERW) pipe process (Figure 2.10), upon exiting the forming mill, the longitudinal edges of the cylinder formed are welded by flash-welding, low-frequency resistance-welding, high-frequency induction-welding, or high-frequency resistance-welding. All processes begin with the forming of the cylinder with the longitudinal seam butt edges ready to be welded.

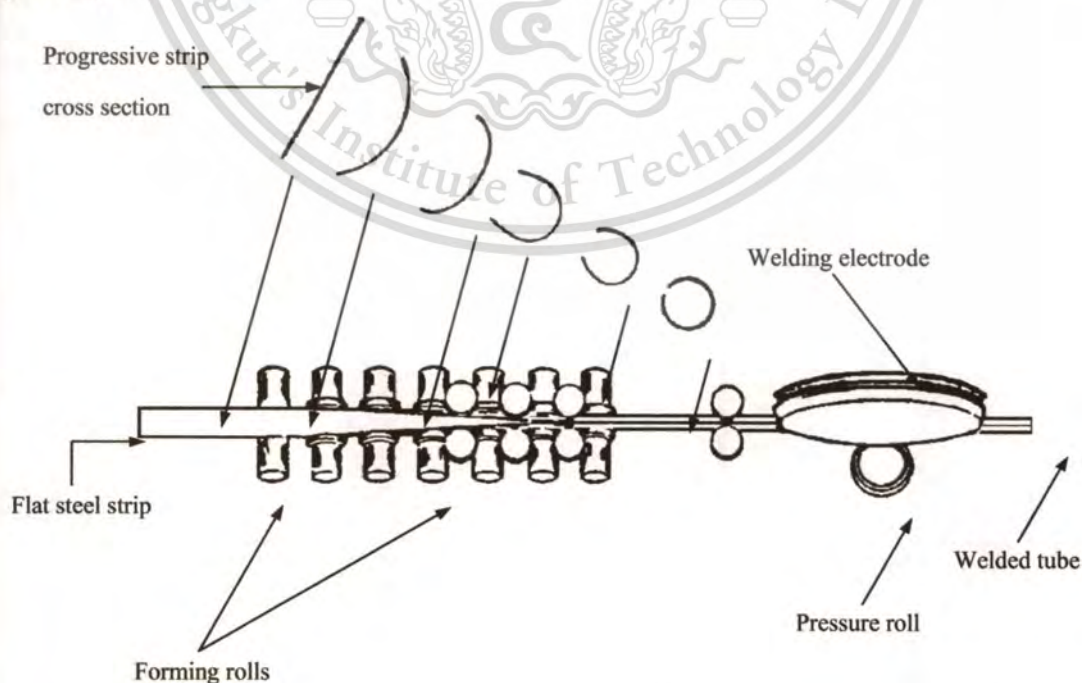


**Figure 2.10** Electric resistance welded pipe process. (PIPING HANDBOOK, 2000)

This material is reserved for educational use only, not allowed for commercial use.

Forbidden to modify the content, and cite the document when use.

It is important to select the optimum tube material for hydroforming in order to achieve successful THF. In this study focus on electric resistance welding (ERW) tube (Figure 2.11) commonly used in Thai industry, a common carbon steel tubing commonly grade STKM 11A, with 28.6 mm outer diameter and 1.2 mm thick is studied

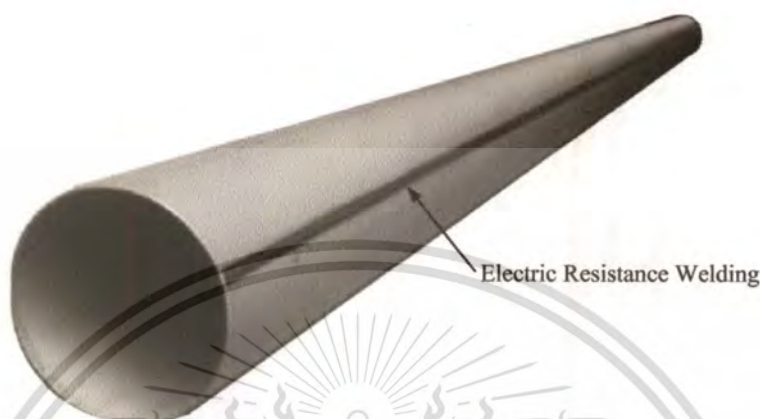


**Figure 2.11** Electric Resistance Welding (ERW) Tube

#### **2.4 Strain-based forming limit curve**

The concept of a forming limit for sheet metal alloys was pioneered by Keeler and Backofen (1963) and Goodwin (1968). They experimentally determined forming limits by measuring the principal surface strains on sheet specimens formed to the onset of localized necking. Keeler and Goodwin also generated forming limit diagrams (FLD) in principal strain space in which a forming limit curve (FLC) represents the boundary beyond which there is a risk of necking for a given sheet metal. Therefore, combinations of principal surface strains that place below the FLC lead to a safe forming operation, whereas those that place above it lead to failure (Muammer Koç, 2008). Figure 2.12 represents a typical FLD for has three basic zones-red, yellow, and green. Any points plotting in the red zone indicate that the part have failed. Visible defects such as split necks fall in the red zone.

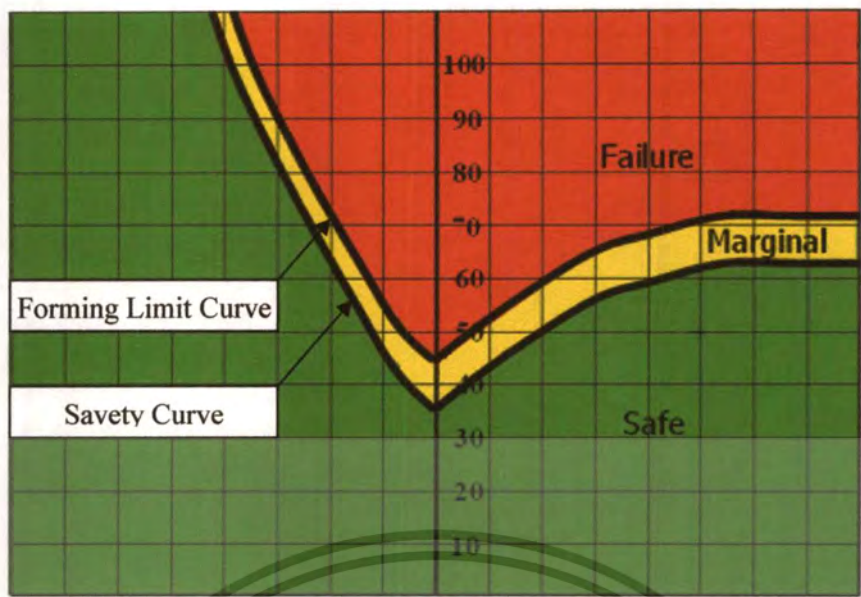


Figure 2.12 Three basic zones - red, yellow, and green of Forming limit diagram.

Circular grids are electrochemically etched onto the surface of sheet steel samples. After the tests, Dimensions of the grid circles at the pole will be measured to calculate true major and minor strains by Equations (2.8)-(2.9), Figure 2.13. The critical major and minor strains are plotted to construct the forming limit curve (FLC) for sheet steel material.

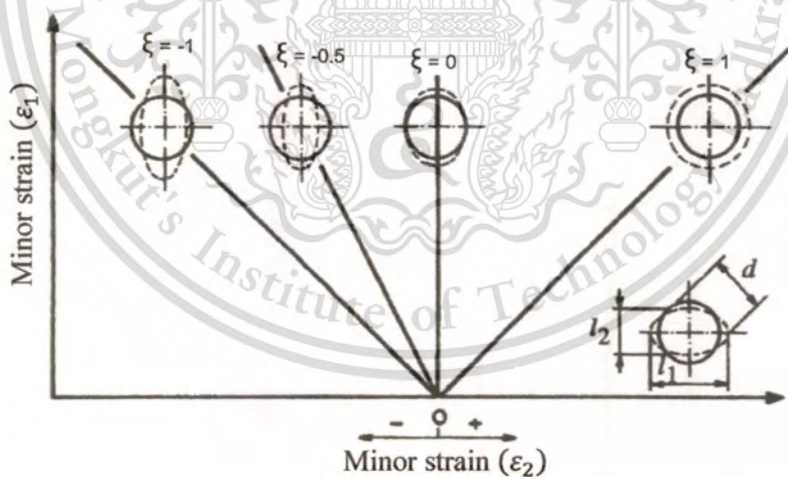


Figure 2.13 FLD with different principle strain ratio

$$\epsilon_1 = \ln \frac{l_1}{d} \tag{2.8}$$

$$\epsilon_2 = \ln \frac{l_2}{d} \tag{2.9}$$

Since many tubes used for hydroforming applications are roll-formed from rolled sheet, it was argued that the concept of the FLD (i.e. from sheet steel) equally applies to tubes. There are important reasons why the standard FLC is not generally applicable to tubular hydroformed parts. One of them being the fact that the roll – forming process of a sheet steel into a tube will incur pre – strained conditions onto the fresh tube. This is known to affect FLC even in the steel sheet forming

The forming limit diagram (FLD) of tubular materials should be established, because it directly influences the formability of the hydraulic forming processes. A few studies concerning the loading paths or the forming limit of tubes and sheets have been reported. For example, Yeong-Maw Hwang (2008) uses bulge tests to establish the forming limit diagram (FLD) of tubular material AA6011 are compared with the forming limits from the analytical FLCs using the  $n$  values obtained by tensile tests and bulge tests. Nefussi and Combescure (2002) used Swift's criteria for sheets and tubes and took into account the buckling induced by axial loading in order to predict plastic instability for tube hydroforming. Korkolis and Kyriakides (2008) studied anisotropic aluminum tubes (Al-6260-T4 tubes) for hydroforming applications. Then investigated the performance of Hosford and Karafillis-Boyce non-quadratic anisotropic yield functions in predicting the response and bursting of tubes loaded under combined internal pressure and axial load. Comparison between numerical simulations and hydroforming experiments on aluminum tubes have indicated that localized wall thinning and burst can be very sensitive to the constitutive description employed for the material. Tirosh et al. (1996) explored an optimized loading path for maximizing the bulge strain between necking and buckling experimentally with aluminum A5052 tubes. Xing and Makinouchi (2001) investigated the differences in forming limits of tubes under internal pressure, independent axial load or torque based on Yamada's plastic instability criteria and Hill's quadratic yield function. The above theory coupled with an in-house finite element code ITAS3d was used to control the material flow and to prevent the final failure modes from occurring. They concluded that the two Swift's criteria are applicable to predict necking and that a special attention has to be paid to plastic buckling, because the critical strains corresponding to buckling are much smaller than the critical strains predicted by the necking criteria. However, experiments are required to validate their theoretical results. So far, a consistent conclusion for forming limit theorems of tubular materials has not been established and the forming limit diagram for STKM 11A tubes has not been found.

This material is reserved for educational use only, not allowed for commercial use.

Forbidden to modify the content, and cite the document when use.

In this study, hydraulic forming apparatus are developed. Experiments of bulge tests with and without axial feeding are accomplished. Loading paths, which correspond to the strain paths with constant strain ratios at the pole of the forming tube, are determined by “LS-DYNA” software and result are the internal pressure and axial feeding are used to control the forming apparatus in the forming limit experiments. The experimentally obtained forming limits are compared with analytically obtained FLCs using Finite Element software.

#### 2.4.1 Formulation of plastic instability criteria

Swift’s diffused necking criterion (Swift, 1952) for thin sheets and Hill’s localized necking criterion (Hill, 1952) associated with the Hill’s non-quadratic yield function (Hill, 1979) are used to construct the FLC for the bi-axial tensile strain zone and tensile-compressive strain zone, respectively. The subtangents of the stress-strain curve,  $Z_d$ , and  $Z_l$ , as diffused necking and localized necking occur, respectively, are given as below,

$$\frac{d\bar{\sigma}}{d\bar{\epsilon}} = \frac{\bar{\sigma}}{Z_d} \quad (2.10)$$

$$\frac{d\bar{\sigma}}{d\bar{\epsilon}} = \frac{\bar{\sigma}}{Z_l} \quad (2.11)$$

$$Z_d = \left[ \frac{\sigma_1(\partial g/\partial \sigma_1) + \sigma_2(\partial g/\partial \sigma_2)}{\sigma_1(\partial g/\partial \sigma_1)^2 + \sigma_2(\partial g/\partial \sigma_2)^2} \right] \frac{dg}{d\bar{\sigma}} \quad (2.12)$$

$$Z_l = \frac{dg/d\bar{\sigma}}{(\partial g/\partial \sigma_1) + (\partial g/\partial \sigma_2)} \quad (2.13)$$

Where  $\bar{\sigma}$  and  $\bar{\epsilon}$  are the effective stress and effective strain, respectively.  $g$  is the plastic potential function. The physical meaning of subtangents  $Z_d$  and  $Z_l$  is shown in Figure 2.14. It is clear that  $Z$  increases as the strain at necking increases. For the detailed derivation of  $Z_d$  and  $Z_l$ , please refer to appendixes A1 and A2.

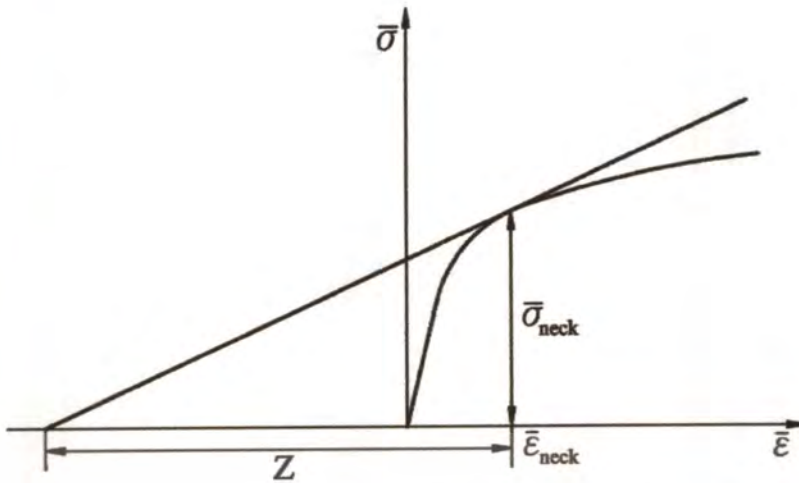


**Figure 2.14** Schematic figure of the subtangent of a stress strain curve as necking occurs.

(Yeong-Maw Hwang, 2009)

For consideration of the effects of normal anisotropy of the material, the Hill's non-quadratic yield function (Hill, 1979) is used to derive the critical strains for diffused necking and localized necking. At first, let the plastic potential function equal the Hill's non-quadratic yield function with a plane stress state:

$$g = \bar{\sigma}^m = \frac{1}{2(1+r)} [(1+2r)|\sigma_1 - \sigma_2|^m + |\sigma_1 + \sigma_2|^m] \quad (2.14)$$

where  $m$  is the exponent of the yield function and  $r$  the normal anisotropy of the material. Then, substituting Equation (2.14) into Equation (2.12) and (2.13), the subtangents for diffused necking and localized necking, respectively, are expressed as

$$Z_d = [2(1+r)]^{1/m} \left\{ \frac{(1+2r)(1-\alpha)|1-\alpha|^{m-1} + (1+\alpha)|1+\alpha|^{m-1}}{(1+\alpha)[(1+2r)^2|1-\alpha|^{2m-2} + |1+\alpha|^{2m-2}] + 2(1+2r)(1-\alpha)|1-\alpha|^{m-1}} \right\} \\ \times [(1+2r)|1-\alpha|^m + |1+\alpha|^m]^{(m-1)/m} \quad (2.15)$$

$$Z_l = \frac{[2(1+r)]^{1/m} [(1+2r)|1-\alpha|^m + |1+\alpha|^m]^{(m-1)/m}}{2|1+\alpha|^{m-1}} \quad (2.16)$$

where  $\alpha$  is the principal stress ratio ( $\alpha = \sigma_2/\sigma_1$ )

Let the effective stress of the material be expressed by a power law of its equivalent strain:

$$\bar{\sigma} = K\bar{\epsilon}^n \quad (2.17)$$

This material is reserved for educational use only, not allowed for commercial use.

Forbidden to modify the content, and cite the document when use.

where  $K$  and  $n$  are the strength coefficient and strain-hardening exponent, respectively, of the material. Substituting Equation (2.17) into Equation (2.10) and (2.11), the critical effective strains for diffused necking and localized necking can be obtained respectively as

$$\bar{\varepsilon}_{cd} = nZ_d, \bar{\varepsilon}_{cl} = nZ_l \quad (2.18)$$

From the flow rule (Chen and Han, 1995),

$$d\varepsilon_1 = \frac{\partial g}{\partial \sigma_1} d\lambda = \frac{m}{2(1+r)} [(1+2r)|\sigma_1 - \sigma_2|^{m-1} + |\sigma_1 + \sigma_2|^{m-1}] d\lambda \quad (2.19)$$

$$d\varepsilon_2 = \frac{\partial g}{\partial \sigma_2} d\lambda = \frac{m}{2(1+r)} [-(1+2r)|\sigma_1 - \sigma_2|^{m-1} + |\sigma_1 + \sigma_2|^{m-1}] d\lambda \quad (2.20)$$

where  $d\lambda$  is a positive scalar factor of proportionality. The principal strain increment ratio can be obtained as

$$\xi = \frac{d\varepsilon_2}{d\varepsilon_1} = \frac{-(1+2r)|1-\alpha|^{m-1} + |1-\alpha|^{m-1}}{(1+2r)|1-\alpha|^{m-1} + |1-\alpha|^{m-1}} \quad (2.21)$$

After arrangement of the above equation, the stress ratio can be obtained as

$$\alpha = \frac{[(1+2r)|1+\xi|]^{1/(m-1)} - |1-\xi|^{1/(m-1)}}{[(1+2r)|1+\xi|]^{1/(m-1)} + |1-\xi|^{1/(m-1)}} \quad (2.22)$$

From the plastic work increment  $W_p = \sigma_{ij} d\varepsilon_{ij} = \bar{\sigma} d\bar{\varepsilon}$ , it follows that

$$d\bar{\varepsilon} = \frac{\sigma_1 d\varepsilon_1 + \sigma_2 d\varepsilon_2}{\bar{\sigma}} = \frac{[2(1+r)]^{1/m} (1+\alpha)/(1-\alpha) (d\varepsilon_1 - d\varepsilon_2)}{2 \left[ (1+2r) + \frac{1+\alpha}{1-\alpha} \right]^{1/m}} \quad (2.23)$$

After combining with Equations (2.19) and (2.20), the major principal strain increment can be expressed as a function of the effective strain increment as below.

$$d\varepsilon_1 = \frac{2}{[2(1+r)]^{1/m}} \times \frac{d\bar{\varepsilon}}{[|1+\xi|^{m/(m-1)} + (1/1+2r)^{1/(m-1)} |1-\xi|^{m/(m-1)}]^{(m-1)/m}} \quad (2.24)$$

During the forming process the stress ratio  $\alpha$  is assumed to be constant; accordingly, the strain increment ratio,  $\xi$ , equal to the strain ratio is a constant. The forming limit for the major principal strain  $\epsilon_{1c}$  can be obtained by integration on both sides of Eq. (2.24), as given below:

$$\begin{aligned}\epsilon_{1c} &= \frac{2}{[2(1+r)]^{1/m}} \times \frac{\bar{\epsilon}}{[|1+\xi|^{m/(m-1)} + (1/1+2r)^{m/(m-1)} |1+\xi|^{m/(m-1)}]^{(m-1)/m}} \\ &= \frac{2}{[2(1+r)]^{1/m}} \times \frac{nZ}{[|1+\xi|^{m/(m-1)} + (1/1+2r)^{m/(m-1)} |1+\xi|^{m/(m-1)}]^{(m-1)/m}}\end{aligned}\quad (2.25)$$

Where  $Z$  is equal to  $Z_d$  and  $Z_p$ , as given in Equations (2.15) and (2.16), for diffused necking and localized necking, respectively. The critical minor principal strain can be obtained from  $\epsilon_{2c} = \xi \epsilon_{1c}$ . A flow chart for determining the forming limit strains is shown in Figure 2.15. At first, the exponent of the yield function,  $m$ , the strain-hardening exponent,  $n$ , and the normal anisotropy,  $r$ , of the material are input. After the strain ratio  $\xi$  is given, the stress ratio can be calculated by Equation (2.22). If,  $\xi > 0$  diffused necking criterion is used. Otherwise, localized necking criterion is used. The critical major strains corresponding to different obtained critical strain pairs ( $\epsilon_{2c}$ ,  $\epsilon_{1c}$ ) for  $1 > \xi > -0.5$ .

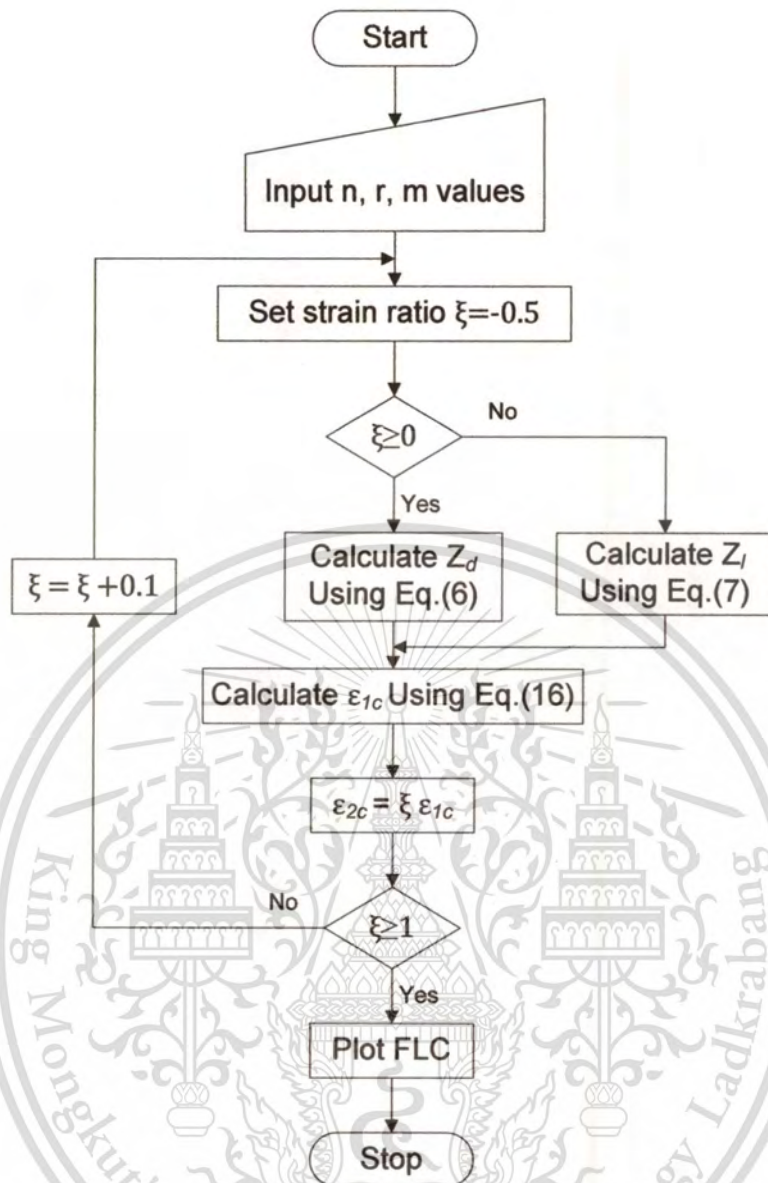
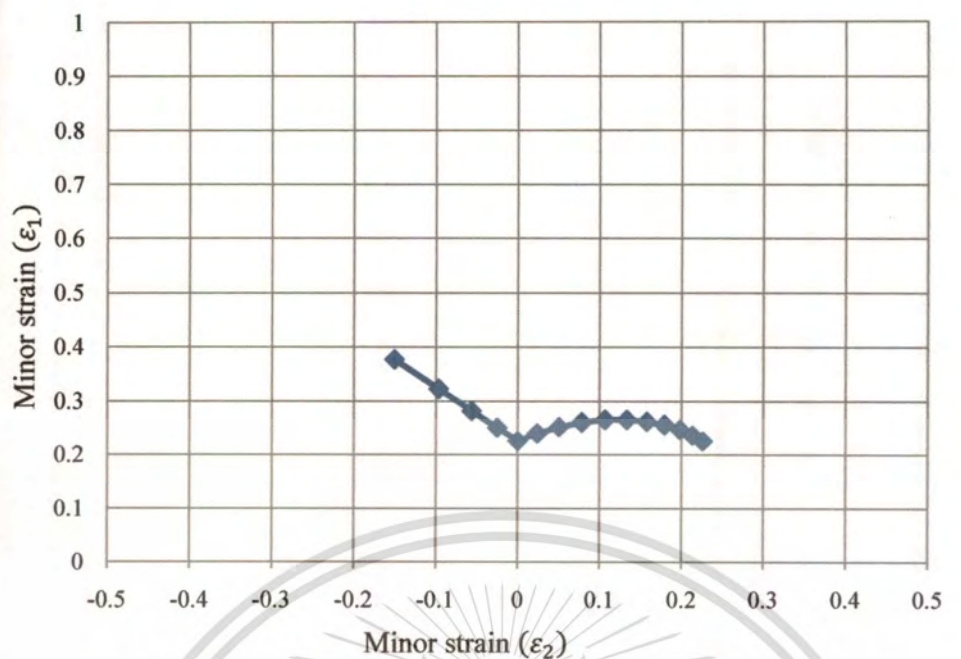
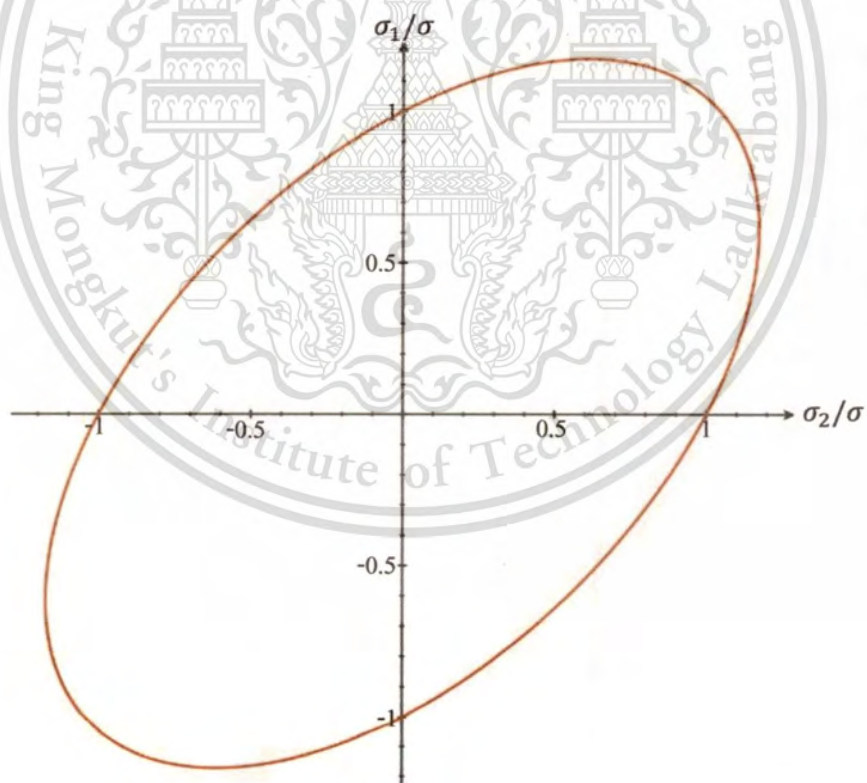


**Figure 2.15** Flow chart for determining the critical major and minor principal strains.

Figure 2.16(a) and (b) shows the forming limit curve and the yield locus, respectively, using Hill's non-quadratic yield function with  $r = 1.856$  and  $n = 0.226$ . The region for stress ratios ( $\alpha = \sigma_2/\sigma_1$ ) from 0.5 to 0 in the yield locus figure corresponds to that for strain ratios ( $\xi = \epsilon_2/\epsilon_1$ ) from 0 to -0.5 in FLC figure.



(a) Forming limit curve



(b) Yield locus

**Figure 2.16** The forming limit curve and yield locus with Hill's non-quadratic yield function.

This material is reserved for educational use only, not allowed for commercial use.

Forbidden to modify the content, and cite the document when use.

**2.4.2 FLC obtained by Finite Element software: DYNAFORM**

FE simulations (Dynaform) are used to determine the loading paths in this study. The analytical FLCs using the n and r values obtained by tensile tests. The FLC curve approximately according to Keeler’s formula as given below:

$$FLD_0 = \frac{n(23.3+14.134t)}{21}, \quad 0 < t < 2.54 \text{ mm}; \quad (2.26)$$

$$FLD_0 = \frac{n[20+(20.669-1.938t)t]}{21}, \quad 2.54 \leq t \leq 5.33 \text{ mm}; \quad (2.27)$$

The shape of FLC is determined by the formulas below:

$$\epsilon_{maj} = FLD_0 + \epsilon_{min}(0.027254\epsilon_{min} - 1.1965) \quad \epsilon_{min} < 0 \quad (2.28)$$

$$\epsilon_{maj} = FLD_0 + \epsilon_{min}(-0.008565\epsilon_{min} - 0.784854) \quad \epsilon_{min} < 0 \quad (2.29)$$

The critical major and minor strains are calculated Keeler’s formula and plotted to construct the forming limit curve (FLC), as show in Figure 2.17.

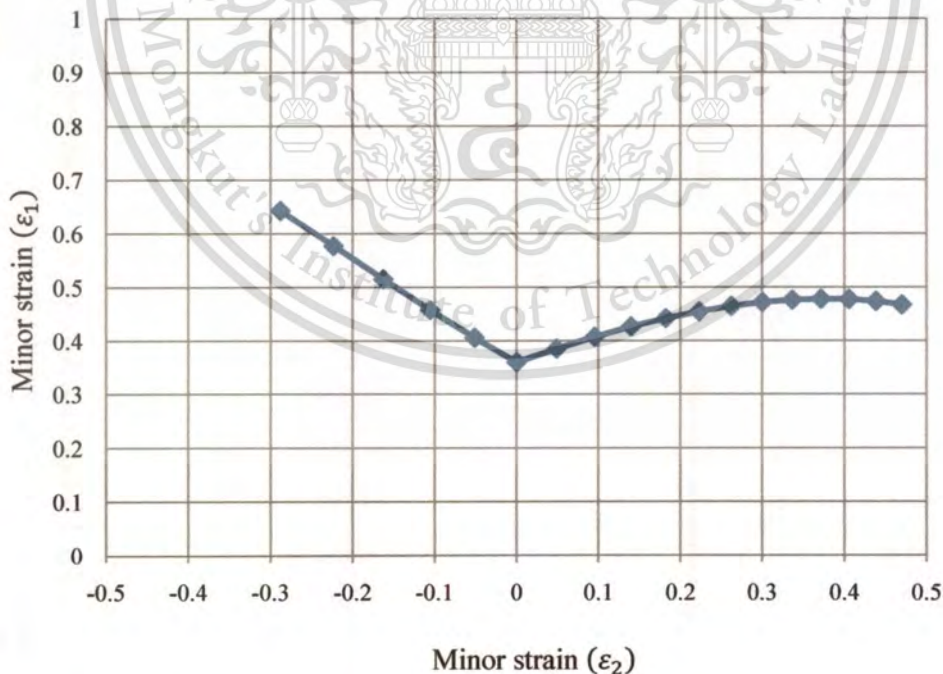


**Figure 2.17** The forming limit curve with Keeler’s formula.

## 2.5 Ductile fracture criterion

A metal that plastically deforms extensively without the onset of fracture is normally termed as ductile. Ductile fracture occurs when a material is subjected to large deformation. In a metal forming process, the ductile fracture is so complicated that many experimental investigations as well as theoretical predictions have been performed to determine that of the metal, and various criteria have been proposed to evaluate the forming limit (Cockroft M. 1968, Norris DM. 1978, Brozzo P. 1972, McClintock FA. 1968, Oyane M. 1980). Unfortunately, it appears that the various criteria have a number of validity restrictions and there are no universal criteria for metal forming process. It is well known that the forming limit of hydroforming process depends greatly upon the deformation history. Therefore, the histories of stress and strain may have to be considered in the criteria. Among these criteria, the ductile fracture criterion proposed by Oyane (1980) was successfully introduced in prediction of forming limit of a sheet metal forming process by Takuda and others (Takuda H. 1999, Takuda H. 1999, Mori K. 1996, Takuda H. 2000). The past researches show that Oyane's ductile fracture criterion can be applied to evaluate the forming limit in a wide range of metal forming processes, including aluminum alloy material which does not have evident localized necking before fracture. Oyane's ductile fracture criterion assumes that the history of hydrostatic stress affects the occurrence of the ductile fracture;

$$\int_0^{\bar{\epsilon}_f} \left( \frac{\sigma_m}{\bar{\sigma}} + C_1 \right) d\bar{\epsilon} = C_2 \quad (2.30)$$

where  $\bar{\epsilon}_f$  is the equivalent strain at fracture,  $\sigma_m$  the mean stress,  $\bar{\sigma}$  the equivalent stress,  $\bar{\epsilon}$  the equivalent strain, and  $C_1, C_2$  the material constants. In Equation (2.30), it is represented that the fracture occurs when the value of the left-hand side reaches that of the right-hand side. Oyane's criterion requires two material constants  $C_1$  and  $C_2$ , which can be obtained from limit strains corresponding to uniaxial tensile test and plane-strain tensile test.

Equation (2.30) can be rewritten as follows:

$$I = \frac{1}{C_2} \int_0^{\bar{\epsilon}_f} \left( \frac{\sigma_m}{\bar{\sigma}} + C_1 \right) d\bar{\epsilon} \quad (2.31)$$

The histories of stress and strain in each element during forming are calculated by the FEM, and

This material is reserved for educational use only, not allowed for commercial use.

Forbidden to modify the content, and cite the document when use.

the ductile fracture integral  $I$  in Equation (2.31) is obtained for each element. When the integral value  $I$  of Equation (2.31) reaches 1.0, the fracture will occur. This ductile fracture value  $I$  can be calculated for every finite element during the forming process.

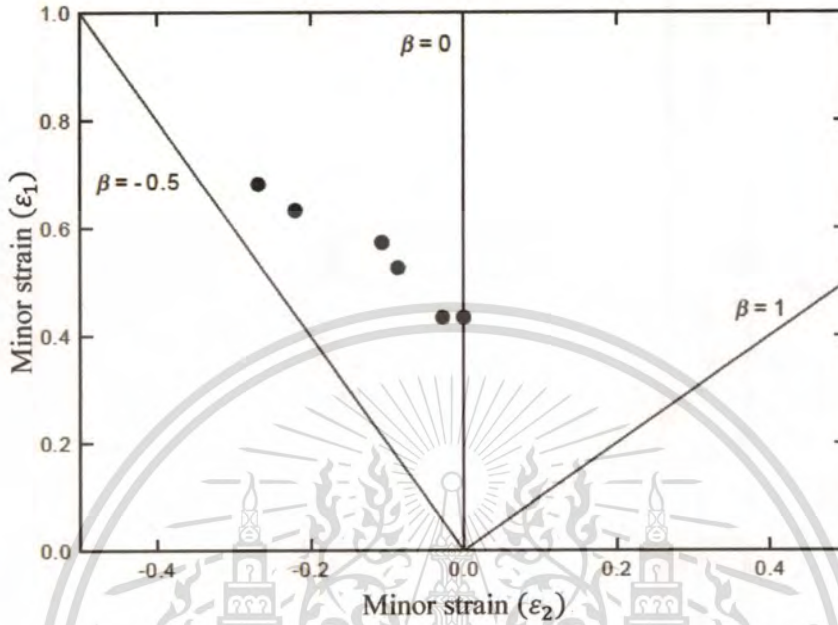


**Figure 2.18** Forming limit diagram obtained experimentally for a STKM-11A tube (Li-Ping Lei, 2002).

Figure 2.18 shows the experimentally obtained forming limit diagram from bulge test of a STKM-11A tube (Li-Ping Lei, 2002). The black dots indicate the strains just at the fracture site. Namely, the ultimate strains for fracture are distributed in the figure. After the localized necking occurs, the plastic deformation almost ceases outside of the necking, while the deformation at the necking region progresses under plane-strain condition to fracture. It is found that the strains after the localized necking tend to decrease with increase in the strain ratio,  $\beta = \varepsilon_2/\varepsilon_1$ , where  $\varepsilon_1$  and  $\varepsilon_2$  are the major and the minor strains on the tube. As a result, the solid circles are linearly distributed as shown in Figure 2.18.

According to the Mises yield criterion and the Levy–Mises stress–strain increment relationship, the terms in Equation (2.30) are expressed by the strain ratio,  $\beta$ , as

$$\frac{\sigma_m}{\bar{\sigma}} = \frac{1+\beta}{\sqrt{3(1+\beta+\beta^2)}} = A(\beta), \quad (2.32)$$

$$d\bar{\varepsilon} = \sqrt{\frac{4}{3}(1+\beta+\beta^2)}d\varepsilon_1 = B(\beta)d\varepsilon_1 \quad (2.33)$$

This material is reserved for educational use only, not allowed for commercial use.

Forbidden to modify the content, and cite the document when use.

Figure 2.19 depicts the above relations. The ratios  $\sigma_m/\bar{\sigma}$  and  $d\bar{\epsilon}/d\epsilon_1$  increase with  $\beta$ . Since the unknowns are two material constants  $C_1$  and  $C_2$ , two arbitrary fracture strains  $\epsilon_{1f}(\beta_1), \epsilon_{1f}(\beta_2)$  in Figure 2.18 should be chosen to get these values. Provided that the strain ratios ( $\beta$ ) are constant during the deformation until the fracture initiation, the material constants are simply calculated from Equation (30), (32) and (33) as the following:

$$\begin{bmatrix} B(\beta_1)\epsilon_{1f}(\beta_1) & -1 \\ B(\beta_2)\epsilon_{1f}(\beta_2) & -1 \end{bmatrix} \begin{Bmatrix} C_1 \\ C_2 \end{Bmatrix} = \begin{Bmatrix} -A(\beta_1)B(\beta_1)\epsilon_{1f}(\beta_1) \\ -A(\beta_2)B(\beta_2)\epsilon_{1f}(\beta_2) \end{Bmatrix} \quad (2.34)$$

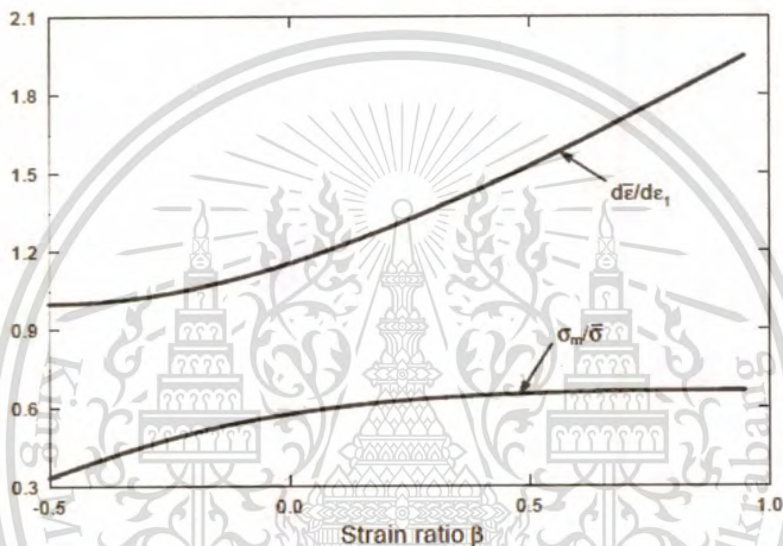


Figure 2.19 Variations of  $\sigma_m/\bar{\sigma}$  and  $d\bar{\epsilon}/d\epsilon_1$  with respect to strain ratio  $\beta$  (Li-Ping Lei, 2002).

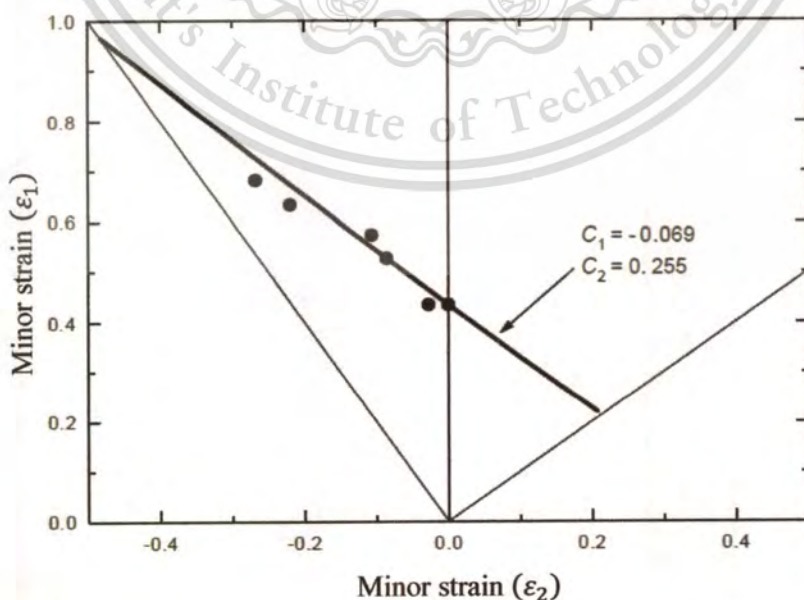


Figure 2.20 Determination of  $C_1$  and  $C_2$  for a STKM-11A tube (Li-Ping Lei, 2002).

This material is reserved for educational use only, not allowed for commercial use.

Forbidden to modify the content, and cite the document when use.

The material constants  $C_1$  and  $C_2$  are determined approximately so that the fracture strains calculated for constant ratios 2t the experimental ones as appeared in Figure 2.20 and then  $C_1 = -0.069$ ,  $C_2 = 0.255$  for STKM-11A material are obtained. The calculated fracture strains are distributed linearly for each pair of material constants. Hence it is found that the distributions of the fracture strains calculated from the ductile fracture criterion are similar to those of the black dots as shown in Figure 2.20.

## 2.6 Effect of non-linearity of strain path.

Several researchers have shown experimentally that a non-linear strain path can change the shape and location of the FLC in strain space. Ghosh and Laukonis (1976) investigated sheet metal forming limit curve based on plastic deformation energy by prestraining stainless steel specimens to various levels of strain and in different deformation. Graf and Hosford (1993a, 1993b) also reported strain-path effects for 2008 T4 aluminium pre-strained in uniaxial, equi-biaxial and near plane-strain tension. The result was a different FLD for each value of prestrain as shown in Figure 2.21. Graf and Hosford (1993a) also attempted to predict the shifted FLD using the Marciniak-Kuczynski (M-K) analysis; however, the predicted FLC did not correlate well with experimental data when the prestrain was in equi-biaxial tension.

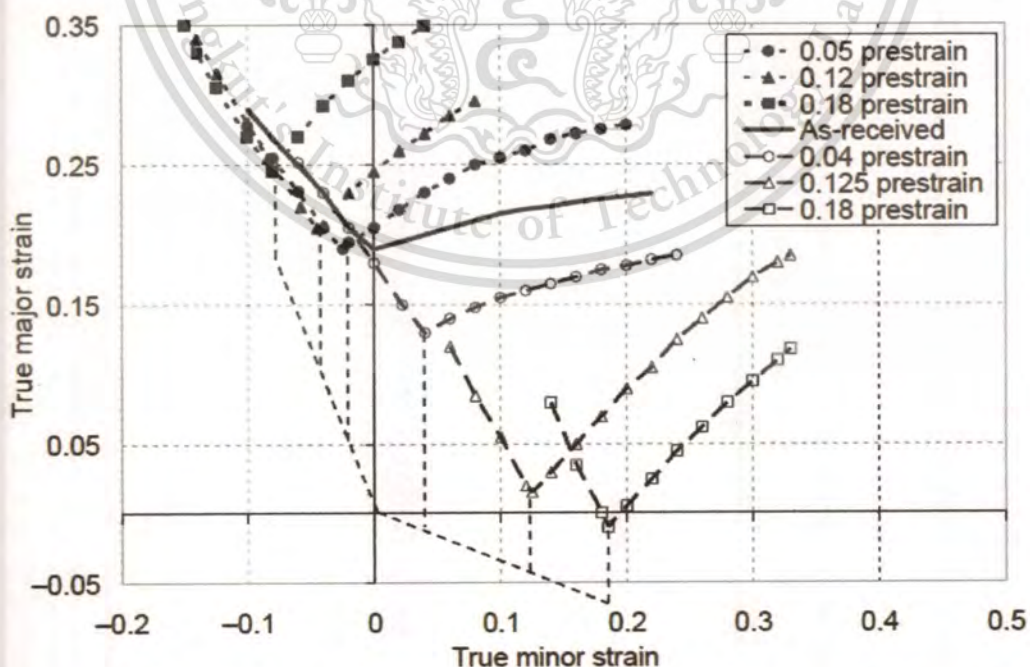
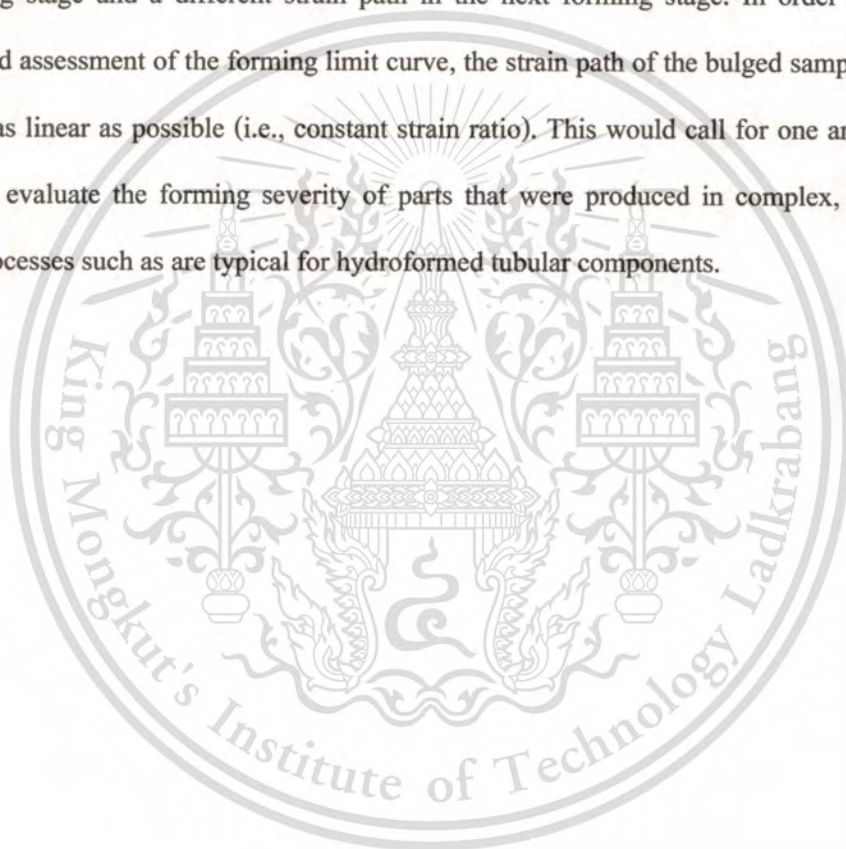


**Figure 2.21** Influence of strain path on the FLC (adapted from Graf and Hosford, 1993).

These experimental observations show that, depending on the loading history, the actual FLC can be significantly different from the as-received FLC. As a result of a change in shape and position, combinations of principal strains that are safe from necking can lie above the as-received FLC, and conversely, failures can take place at strains below the as-received FLC. Furthermore, during any forming operation, different locations on a part undergo different strains and forming modes. If the component is manufactured in two or more forming stages, the overall strain path in each location can be severely non-linear as a result of following one strain path in one forming stage and a different strain path in the next forming stage. In order to obtain a standardized assessment of the forming limit curve, the strain path of the bulged sample has to be controlled as linear as possible (i.e., constant strain ratio). This would call for one and the same material to evaluate the forming severity of parts that were produced in complex, multi-stage forming processes such as are typical for hydroformed tubular components.



## CHAPTER 3

# RESEARCH METHODOLOGY

This research aimed to establish the forming limit curve (FLC) of tubular material low carbon steels commonly used in Thai industry, namely STKM 11A with 1.2 mm thickness and 28.6 mm outer diameter, compare these experimentally obtained FLCs against analytical and empirical ones available in FEA software (Dynaform) and Formulation of plastic instability criteria, and verify these FLCs with real part hydroforming experiments. First, bulge forming apparatus of fixed bulge length and a hydraulic test machine with axial feeding were used to carry out the bulge tests that were able to keep linear strain part at the apex of the bulging tube. FEM was used to determine die proper insert parameters such as free bulge length ( $L$ ), die entry radius ( $r_d$ ). Second, loading paths corresponding to the strain paths with constant strain ratios at the apex of the bulging tube were also determined by FE simulations, which in turn were used to control the internal pressure and axial feeding punch of the test machine. Third, preparing the tube blank, circular grids were electro chemically etched onto the surface of tube samples. Then, after running bulge tests, the major and minor strains of the grids beside the bursting line on the tube surface are measured to construct the forming limit curve. Finally, compare these FLCs against empirical FLCs and verify these FLCs with real part forming experiments to achieve the objectives and scope of this research. The procedure of research is as follows.

1. Study tools and equipment used in research.
2. Study material properties used in the experiments.
3. Study the forming process.
4. Learn how to use Dynaform.
5. Run Tube Hydroforming simulations for test die insert design and process parameter determination.
6. Prepare Tube blank such as cutting, sanding, griding of any sharp edges and electro chemically etched onto the surface of tube samples.
7. Conduct the experiment, collect and analyze the data.
8. Construct the forming limit curve.
9. Compare and verify the obtained FLD's.

This material is reserved for educational use only, not allowed for commercial use.

Forbidden to modify the content, and cite the document when use.

### 3.1 Numerical Investigation

#### 3.1.1 Test die insert design

Several researchers (Jieshi Chen, Xianbin Zhou and Jun Chen, 2009) have shown experimentally that non-linear strain path can change the shape and location of the FLC. Nevertheless, to an extent, this effect on the FLC can be minor if the non-linearity is kept small. In order to obtain a standardized assessment of the forming limit curve, the strain path at the apex of the bulged sample has to be controlled as linear as possible (i.e., constant strain ratio). In this work, it was necessary to design proper testing die insert geometry – 1) die entry radius ( $r_d$ ) and 2) bulge length ( $L$ ), as show in Figure 3.1.

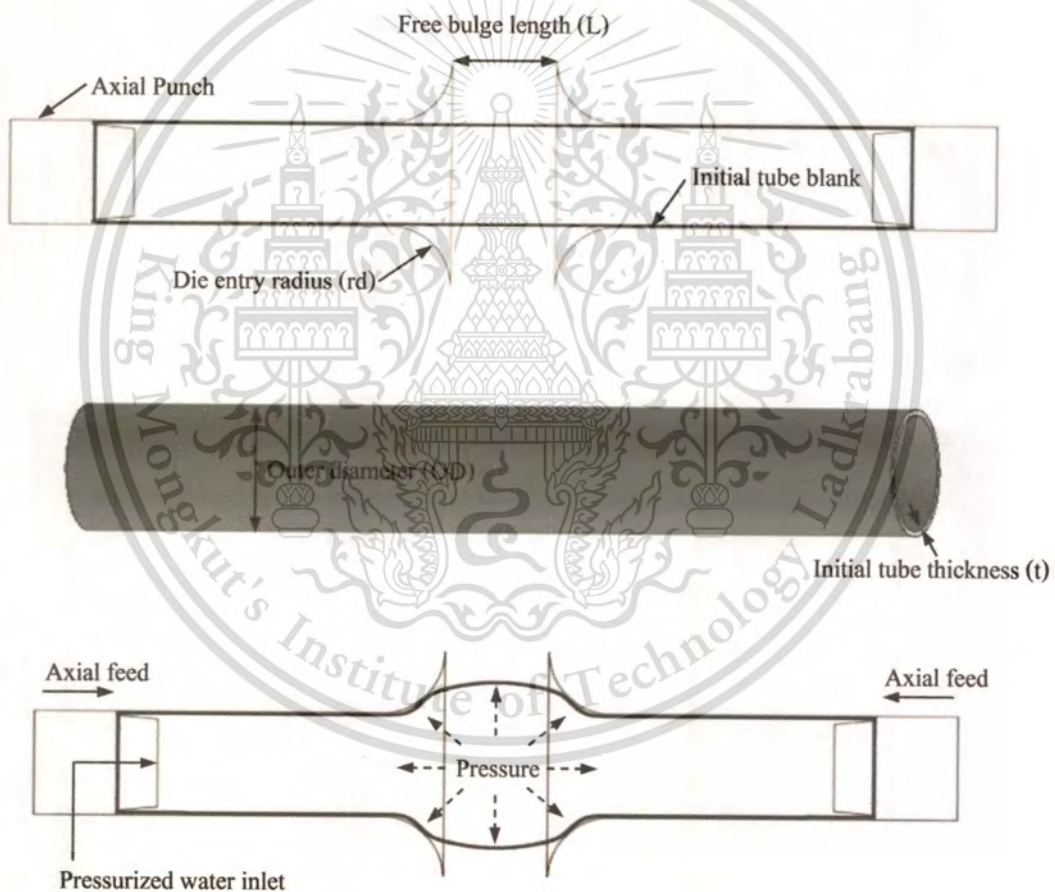


**Figure 3.1** Schematic diagram of the test die insert parameters

An FEA software (DYNAFORM) was used to conduct all the simulations in this work. Due to its symmetry, only one half of the testing a die insert and tube sample were model, see Figure 3.2. In each case of simulation run, several process parameters (i.e. pressure and axial

This material is reserved for educational use only, not allowed for commercial use.

Forbidden to modify the content, and cite the document when use.

feed distance) were tried in an attempt to form the sample with linear strain paths. Any elements in the red indicate that the parts have failed.

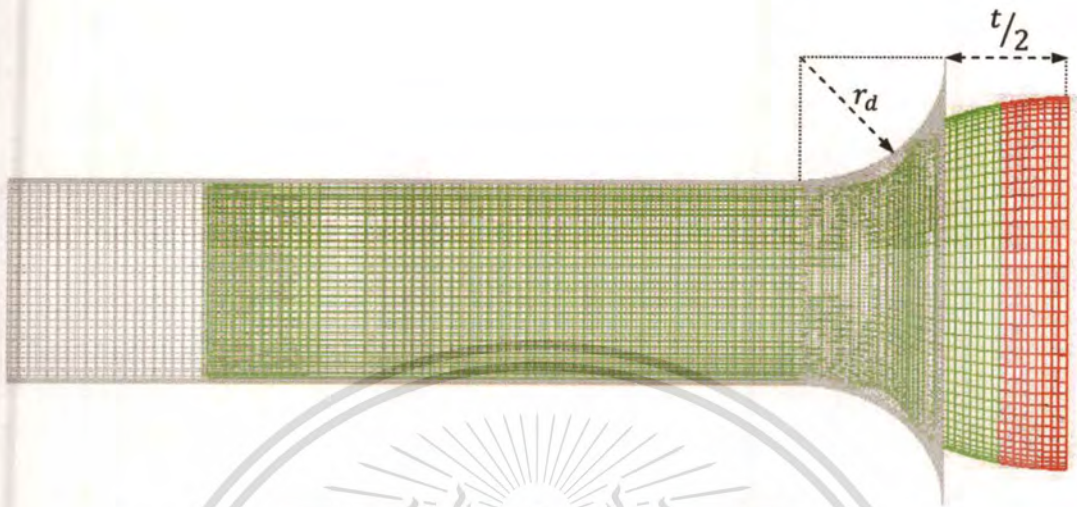


**Figure 3.2** The formed part show in half model

The specimen tubes were modeled with 1 mm thickness and 25.4 mm outer diameter. Two geometry parameters were used to investigate, namely 1) L/OD and 2) rd/t, see table 3.1. A series of simulation were conducted with various die insert geometry and tube sample dimensions, see table 3.2, to determine the proper testing die insert geometer.

**Table 3.1** Design of simulation matrix

L/OD	1	2	3
L	25.4	50.8	76.2
OD	25.4	25.4	25.4
rd/t	5	15	25
rd	5	15	25
t	1	1	1

**Table 3.2** A series of simulation

Model	L/OD	rd/t	L	OD	rd	t
RUN01	1	5	25.4	25.4	5	1
RUN02	1	15	25.4	25.4	15	1
RUN03	1	25	25.4	25.4	25	1
RUN04	2	5	50.8	25.4	5	1
RUN05	2	15	50.8	25.4	15	1
RUN06	2	25	50.8	25.4	25	1
RUN07	3	5	76.2	25.4	5	1
RUN08	3	15	76.2	25.4	15	1
RUN09	3	25	76.2	25.4	25	1

It was found that only properly designed die insert geometry relative to tube sample geometry – 1) tube outer diameter (OD) and 2) tube sample thickness (t) will allow the linear strain path during testing. Four strain ratios ( $\xi = \varepsilon_2/\varepsilon_1$ ) -0.1, -0.2, -0.3 and -0.4 were the slopes of each strain path under investigation in this work. If no possible internal pressure and axial feed distance were found to fulfill the constant strain ratios then it was concluded that the specific die insert geometry is not proper.

**Table 3.3** Simulation results

Model	L/OD	rd/t	L(mm)	OD(mm)	rd(mm)	t(mm)	Resultant strain ratio( $\xi$ )
RUN01	1	5	25.4	25.4	5	1	Non-linear
<b>RUN02</b>	<b>1</b>	<b>15</b>	<b>25.4</b>	<b>25.4</b>	<b>15</b>	<b>1</b>	<b>Linear</b>
RUN03	1	25	25.4	25.4	25	1	Non-linear
RUN04	2	5	50.8	25.4	5	1	Non-linear
RUN05	2	15	50.8	25.4	15	1	Non-linear
RUN06	2	25	50.8	25.4	25	1	Non-linear
RUN07	3	5	76.2	25.4	5	1	Non-linear
RUN08	3	15	76.2	25.4	15	1	Non-linear
RUN09	3	25	76.2	25.4	25	1	Non-linear

Table 3.3 summarizes the results of this simulation finding. Only die insert geometry in simulation RUN02 yields the satisfying linear strain path requirement (i.e. constant strain ratio  $\xi \pm 0.01$ ). It can be seen that only RUN02 is able to keep the strain ratio of -0.4 constant (i.e. linear) all the way to the fracture limit, FLC.

The ratio of Model Run02 ( $L/OD=1$  and  $rd/t=15$ ), were put to test in another outer diameter and thickness of tube sample. A series of simulation were conducted with two geometry ratio to verify, namely 1)  $L/OD=1$  and 2)  $rd/t=15$ , see table 3.4, to verify the proper testing die insert geometer.

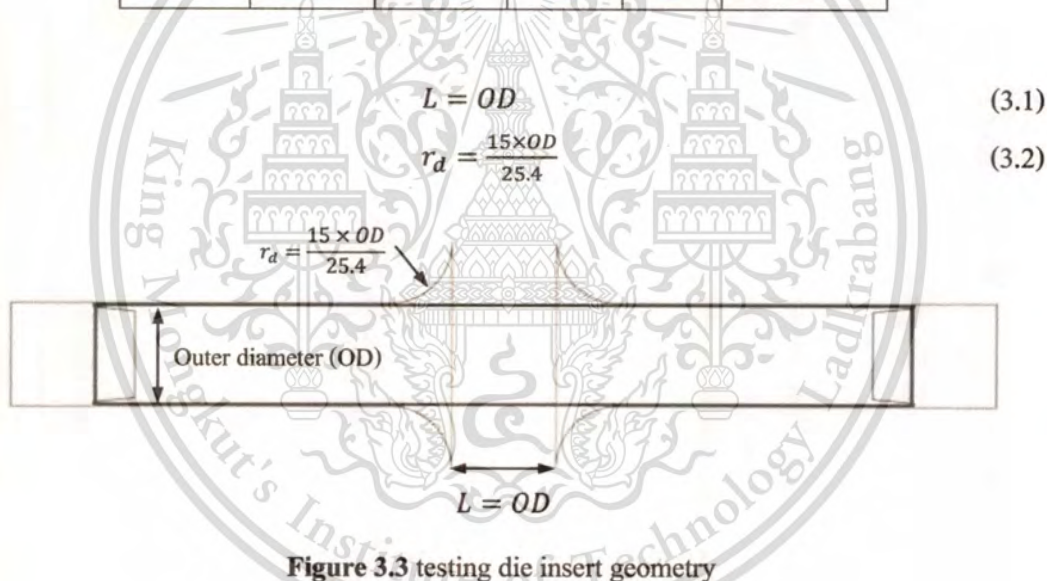
**Table 3.4** A series of simulation,  $L/OD=1$  and  $rd/t=15$

Model	L/OD=1		rd/t=15	
	L(mm)	OD(mm)	rd(mm)	t(mm)
TEST01	12.7	12.7	7.5	0.5
TEST02	12.7	12.7	15	1
TEST03	12.7	12.7	30	2
TEST04	25.4	25.4	7.5	0.5
TEST05	25.4	25.4	15	1
TEST06	25.4	25.4	30	2
TEST07	50.8	50.8	7.5	0.5
TEST08	50.8	50.8	15	1
TEST09	50.8	50.8	30	2

Table 3.5 summarizes the results of second simulation finding. Die insert geometry in simulation TEST01, TEST05 and TEST09 yields the satisfying linear strain path requirement (i.e. constant strain ratio  $\xi \pm 0.01$ ). It was found the tool geometry that can keep the strain ratio constant is not dependent on the thickness but dependent on only OD of the tube, as given in Equations (3.1)-(3.2), see figure 3.3.

**Table 3.5** Result of Simulation, L/OD=1 and rd/t=15

Model	L/OD=1		rd/t=15		Results
	L(mm)	OD(mm)	rd(mm)	t(mm)	
<u>TEST01</u>	<u>12.7</u>	<u>12.7</u>	<u>7.5</u>	<u>0.5</u>	Linear
TEST02	12.7	12.7	15	1	Non-linear
TEST03	12.7	12.7	30	2	Non-linear
TEST04	25.4	25.4	7.5	0.5	Non-linear
<u>TEST05</u>	<u>25.4</u>	<u>25.4</u>	<u>15</u>	<u>1</u>	Linear
TEST06	25.4	25.4	30	2	Non-linear
TEST07	50.8	50.8	7.5	0.5	Non-linear
TEST08	50.8	50.8	15	1	Non-linear
<u>TEST09</u>	<u>50.8</u>	<u>50.8</u>	<u>30</u>	<u>2</u>	Linear

**Figure 3.3** testing die insert geometry

### 3.1.2 Determination of loading paths by FE-simulations

The ratio of Proper Model according to equations (3.1) and (3.2), were put to model with 1.2 mm thickness and 28.6 mm outer diameter tube blank. Internal pressure and axial feed distance under investigation in this work were used to control the four strain ratios ( $\xi = \varepsilon_2/\varepsilon_1$ ) -0.1, -0.2, -0.3 and -0.4 at the apex of the bulged sample as linear as possible. The corresponding loading paths to the four linear strain paths are determined by FE simulations, shown in Figure 3.4, 3.5 and 3.6. Results of the formed simulation with four different strain ratios

( $\xi = \varepsilon_2/\varepsilon_1$ ) -0.1, -0.2, -0.3, -0.4 and no feeding show in half model, see Figure 3.7 and each of strain path are shown in Figure 3.8.

	Feeding Distance			
	$\xi=-0.1$	$\xi=-0.2$	$\xi=-0.3$	$\xi=-0.4$
0	0	0	0	0
1	0.001176	0.002941	0.011765	0.023529
2	0.002353	0.005882	0.023529	0.047059
3	0.003529	0.008824	0.035294	0.070588
4	0.004706	0.011765	0.047059	0.094118
5	0.005882	0.014706	0.058824	0.117647
6	0.007059	0.017647	0.070588	0.141176
7	0.008235	0.020588	0.082353	0.164706
8	0.009412	0.023529	0.094118	0.188235
9	0.010588	0.026471	0.105882	0.211765
10	0.011765	0.029412	0.117647	0.235294
11	0.012941	0.032353	0.129412	0.258824
12	0.014118	0.035294	0.141176	0.282353
13	0.015294	0.038235	0.152941	0.305882
14	0.016471	0.041176	0.164706	0.329412
15	0.017647	0.044118	0.176471	0.352941
16	0.018824	0.047059	0.188235	0.376471
17	0.02	0.05	0.2	0.4
18	0.03	0.08	0.3	0.8
19	0.07	0.15	0.4	1.3
20	1.25	2.5	4.75	9

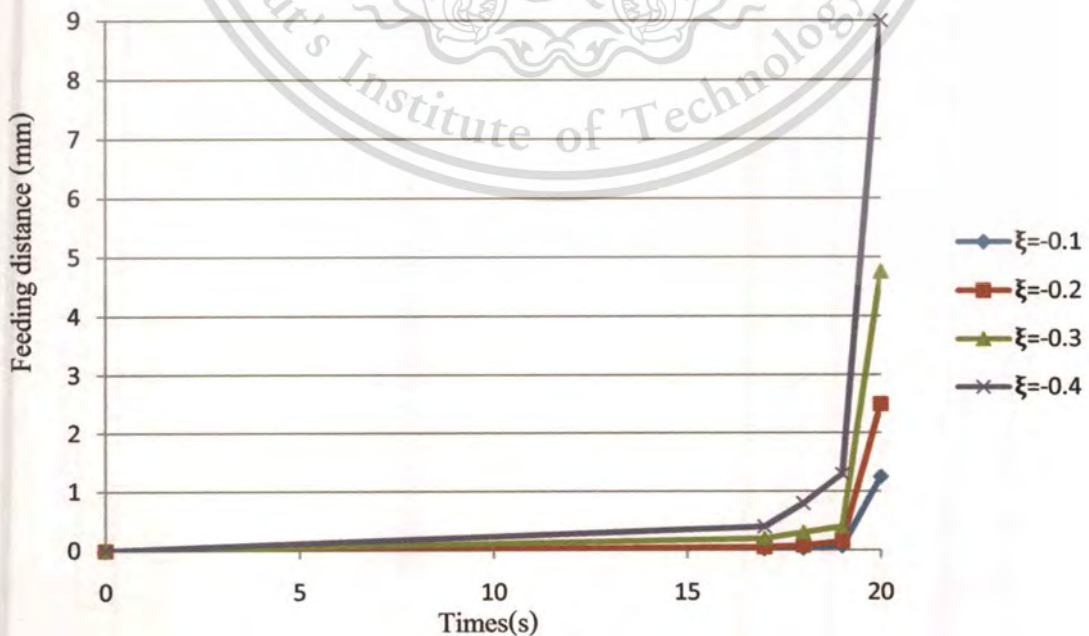


**Figure 3.4** Feeding distance (mm) with time(s)

This material is reserved for educational use only, not allowed for commercial use.

Forbidden to modify the content, and cite the document when use.

Time(s)	Internal Pressure (bar)				
	$\xi=-0.1$	$\xi=-0.2$	$\xi=-0.3$	$\xi=-0.4$	No feeding
0	0	0	0	0	0.000
1	220	220	220	220	13.325
2	221.7737	221.3553	220.8421	220.1579	26.650
3	223.5474	222.7105	221.6842	220.3158	39.975
4	225.3211	224.0658	222.5263	220.4737	53.300
5	227.0947	225.4211	223.3684	220.6316	66.625
6	228.8684	226.7763	224.2105	220.7895	79.950
7	230.6421	228.1316	225.0526	220.9474	93.275
8	232.4158	229.4868	225.8947	221.1053	106.600
9	234.1895	230.8421	226.7368	221.2632	119.925
10	235.9632	232.1974	227.5789	221.4211	133.250
11	237.7368	233.5526	228.4211	221.5789	146.575
12	239.5105	234.9079	229.2632	221.7368	159.900
13	241.2842	236.2632	230.1053	221.8947	173.225
14	243.0579	237.6184	230.9474	222.0526	186.550
15	244.8316	238.9737	231.7895	222.2105	199.875
16	246.6053	240.3289	232.6316	222.3684	213.200
17	248.3789	241.6842	233.4737	222.5263	226.525
18	250.1526	243.0395	234.3158	222.6842	239.850
19	251.9263	244.3947	235.1579	222.8421	253.175
20	253.7	245.75	236	223	266.5

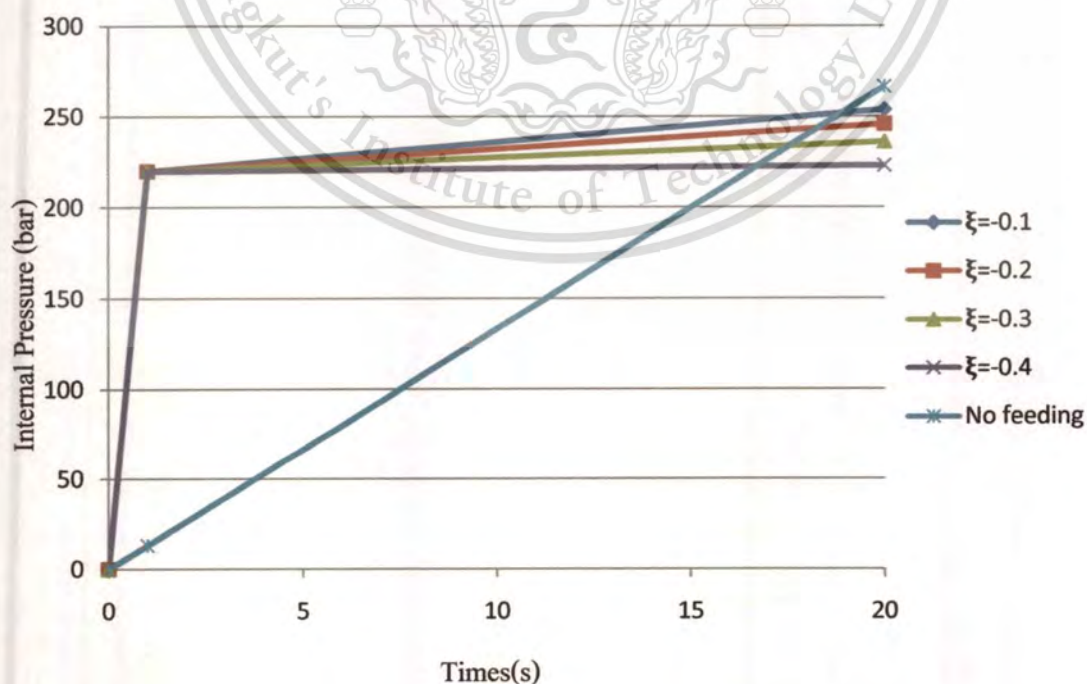


**Figure 3.5 Internal Pressure (bar) with time (s)**

This material is reserved for educational use only, not allowed for commercial use.

Forbidden to modify the content, and cite the document when use.

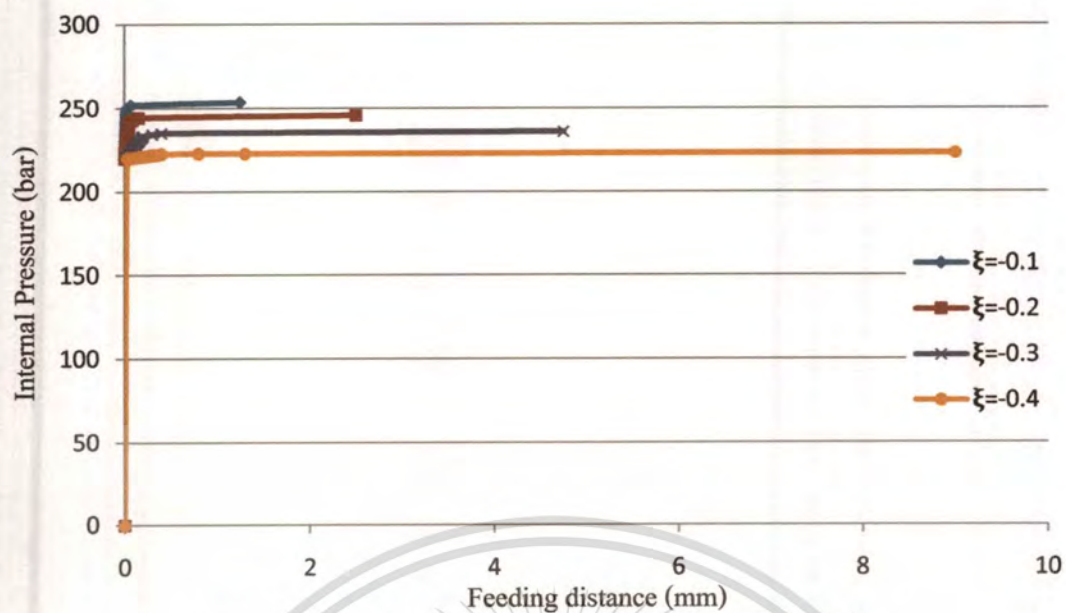


Figure 3.6 Feeding distance (mm) with Internal Pressure (bar)



Figure 3.7 a.) No feeding

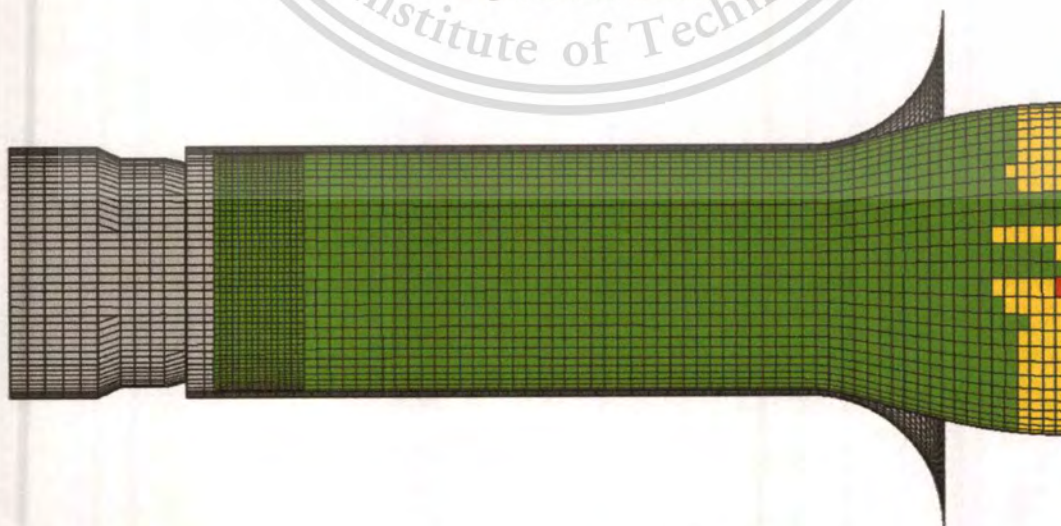


Figure 3.7 b.)  $\xi(\varepsilon_2/\varepsilon_1) = -0.1$

This material is reserved for educational use only, not allowed for commercial use.

Forbidden to modify the content, and cite the document when use.

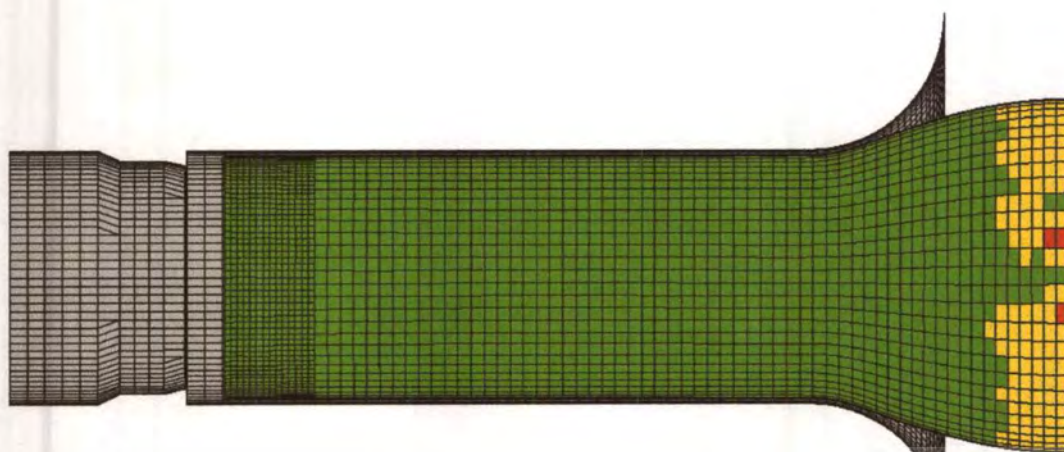


Figure 3.7 c.)  $\xi(\varepsilon_2/\varepsilon_1) = -0.2$

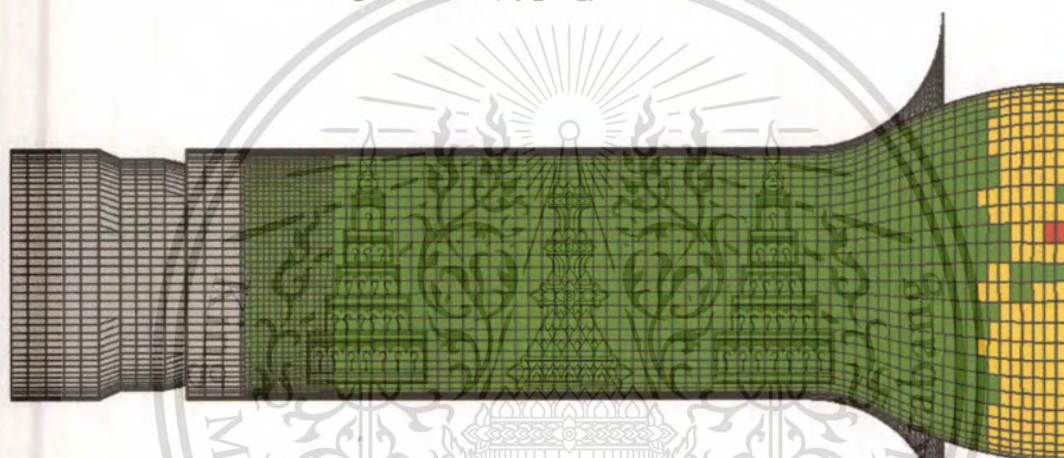


Figure 3.7 d.)  $\xi(\varepsilon_2/\varepsilon_1) = -0.3$

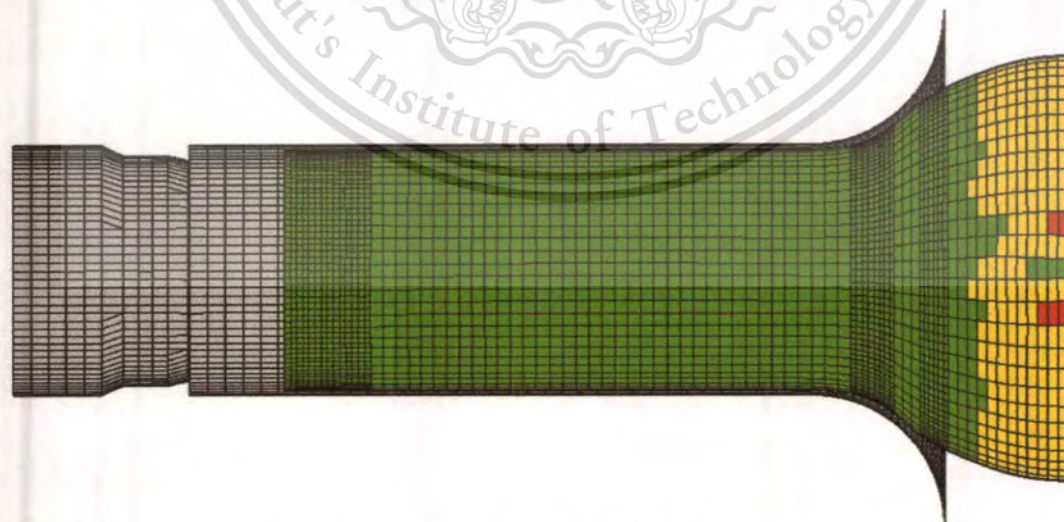


Figure 3.7 e.)  $\xi(\varepsilon_2/\varepsilon_1) = -0.4$

**Figure 3.7** Simulation results with four strain ratios ( $\xi = \varepsilon_2/\varepsilon_1$ ) -0.1, -0.2, -0.3, -0.4 and no feeding

This material is reserved for educational use only, not allowed for commercial use.

Forbidden to modify the content, and cite the document when use.

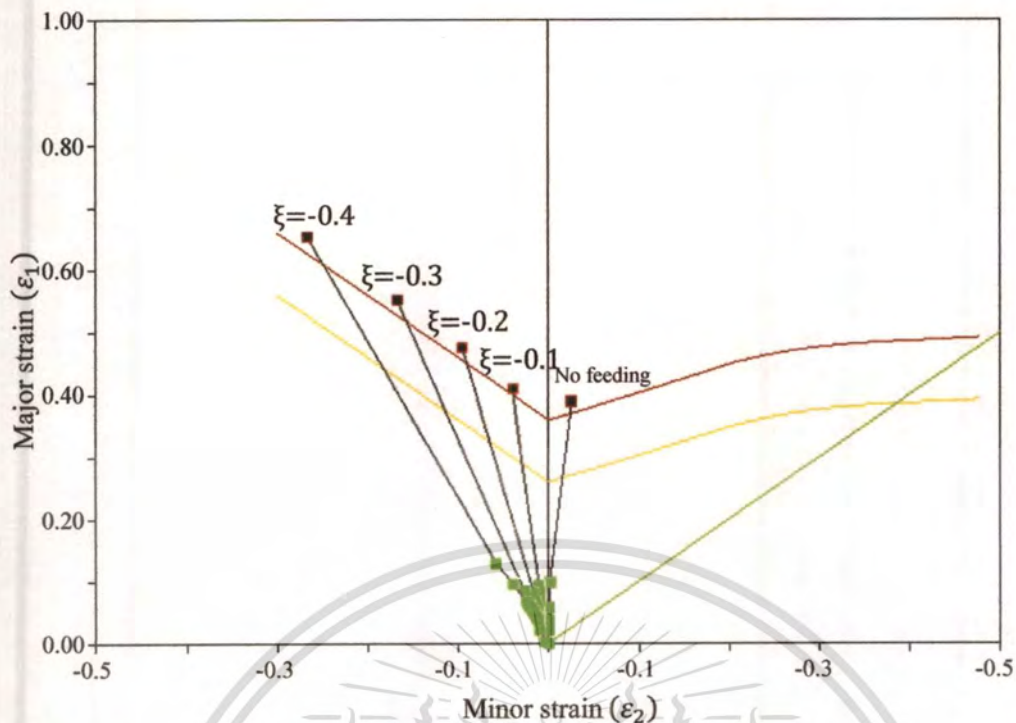


Figure 3.8 Different strain paths investigated

## 3.2 Experimental Investigation

### 3.2.1 FLC testing apparatus

A bulge test apparatus with a fixed bulge length without axial feeding as shown in Figure 3.9 is used to implement the forming limit experiments to obtain the strain path on right side of the FLD. The specimen 300 mm initial tube lengths are expanded at both the end of the tube and fixed by punches during forming.

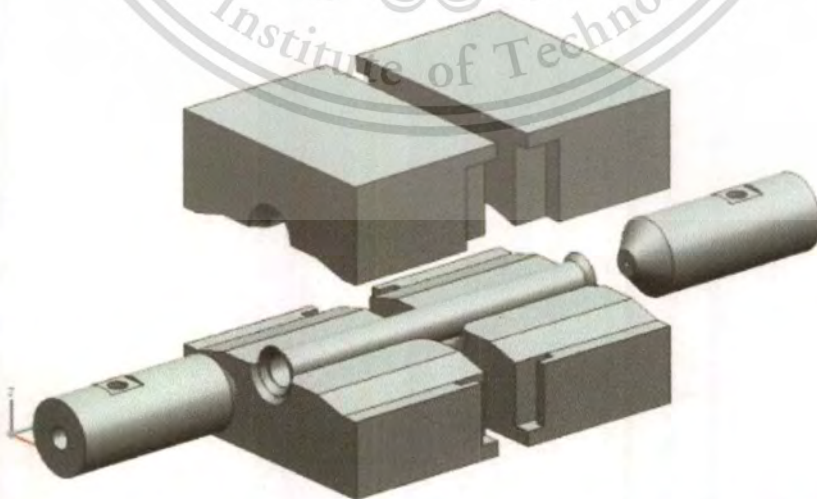
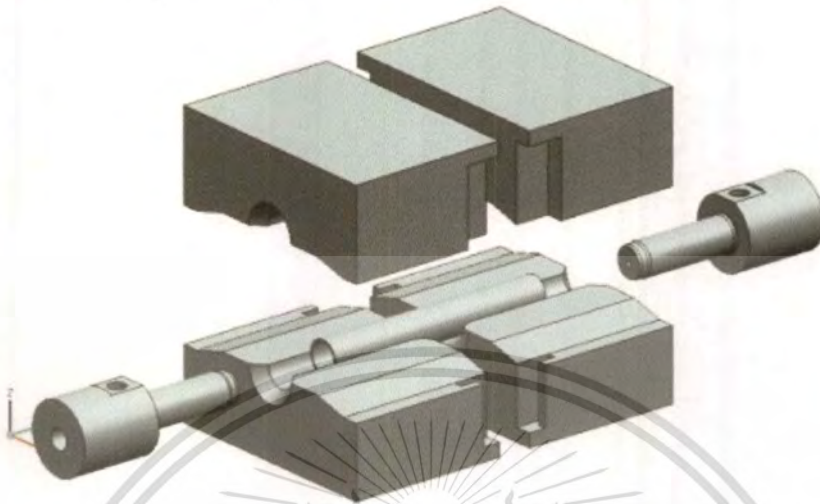


Figure 3.9 The experimental apparatus for bulge tests without axial feeding.

A hydroforming test machine with axial feeding is used to conduct the experiments with 200 mm initial tube length to obtain the strain paths on the left side of the FLD, in which tensile and compressive strains occur as shown in Figure 3.10



**Figure 3.10** The experimental apparatus for bulge tests with axial feeding.



**Figure 3.11** Schematic diagram of the experimental apparatus for bulge tests

### 3.2.2 THF Test Specimens

Before bulge tests, the tubes of STKM low carbon steels are 200 mm (with axial feeding) and 300 mm (without axial feeding) long, 1.2 mm thick, and 25.8 mm in outer diameter. They are rounded off of any sharp edges in the tubular blanks by lathe machine, for the tubes used for the forming limit experiments, circular grids with a diameter of 2.5mm as shown in Figure 3.12 are electrochemically etched on the tube surface before the experiments, see Figure 3.12.

This material is reserved for educational use only, not allowed for commercial use.

Forbidden to modify the content, and cite the document when use.

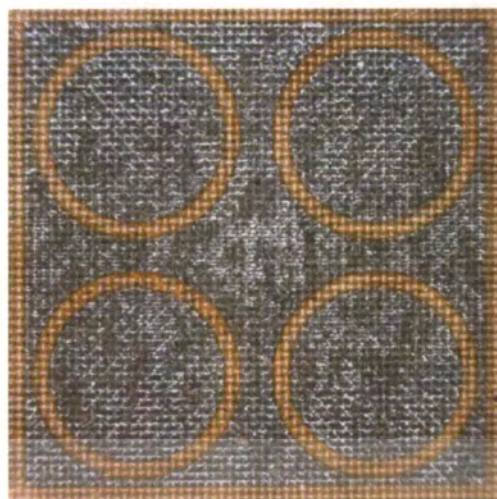


**Figure 3.11** Circular grids with a diameter of 2.5mm



**Figure 3.12** THF Test Specimens

### 3.2.3 Hydraulic Press

In the hydroforming process, hydraulic presses are typically used to open and close the die and to provide enough clamping load during the forming period to prevent die separation. A 200 ton hydraulic press was used in this experiment. The press is controlled by a CNC controller shown in Figure 3.13.



**Figure 3.13** Hydraulic press and CNC controller

### 3.2.4 Pressure system, Hydraulic cylinders and punches

The pressure system (pump, intensifier and control and relief valves, coolers, etc.) provide the required pressure levels, which are controlled by CNC controller, shown in figure 3.14. The axial punches are necessary to seal the end of the tube to avoid pressure losses and to feed material into expansion regions. They should feed the material in a controlled path, and in synchronization with internal pressure.



**Figure 3.14** CNC controller used to control internal pressure and axial punches

### 3.3 Grid measurement

After bulge tests, Dimensions of the grid circles at the pole ( $-45^\circ$  to  $45^\circ$  from welding line) were accurately measured to obtain true major and minor strains by Equations. (2.8)- (2.9). The critical major and minor strains are plotted to construct the forming limit curve (FLC) for tubular material.

#### 3.3.1 Digital Microscope

A Digital Microscope that shown in Figure 3.15.is used to take snapshots of the deformed grids, which are later measured for true major and minor strains. After the bulge tests, the measured major and minor strains on the tube surface are used to construct the forming limit curve. A grid is captured by Dino Capture Software and measure the diameter of deformed grids as show in Figure 3.16



**Figure 3.15** Digital Microscope (Dino-Lite)

This material is reserved for educational use only, not allowed for commercial use.

Forbidden to modify the content, and cite the document when use.

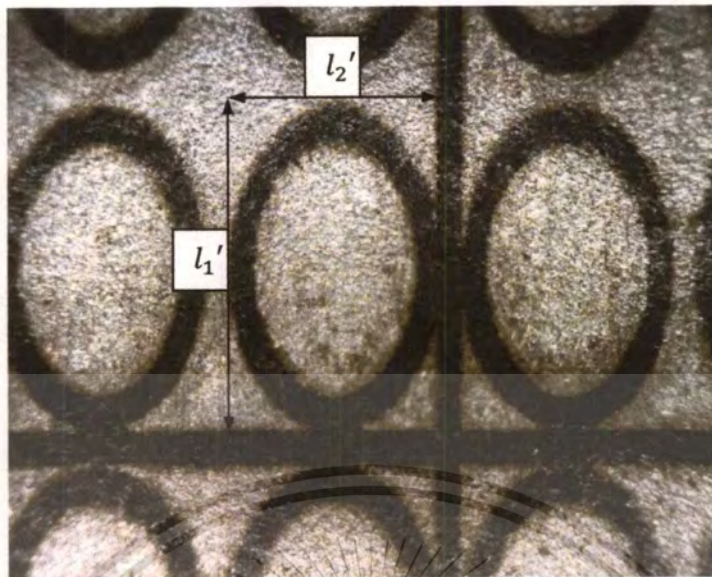


**Figure 3.16** The deformed grids measured using Dino Capture Software

### 3.3.2 Grid Curvature

As specimen are tubular and final form are bulge shape, the captured grid from Digital Microscope are projected from real deformed grids; therefore, corrective curve is important to achieve the real deformed grid diameter and FLC. The curvature has two radii,  $r_{\phi P}$  is meridian radius of curvature at the pole as shown in figure 3.17 and  $r_{\theta P}$  is circumferential radius of curvature at the pole as shown in figure 3.18. meridian and circumferential radii of curvature at the pole



**Figure 3.17**  $r_{\phi P}$  is meridian radius of curvature at the pole



**Figure 3.18**  $r_{\theta P}$  is circumferential radius of curvature at the pole

This material is reserved for educational use only, not allowed for commercial use.

Forbidden to modify the content, and cite the document when use.

The digital camera with macro lens is used to capture the shape of bulge tube, see in figure 3.19 and approximate the curve by CAD software, see in figure 3.20.

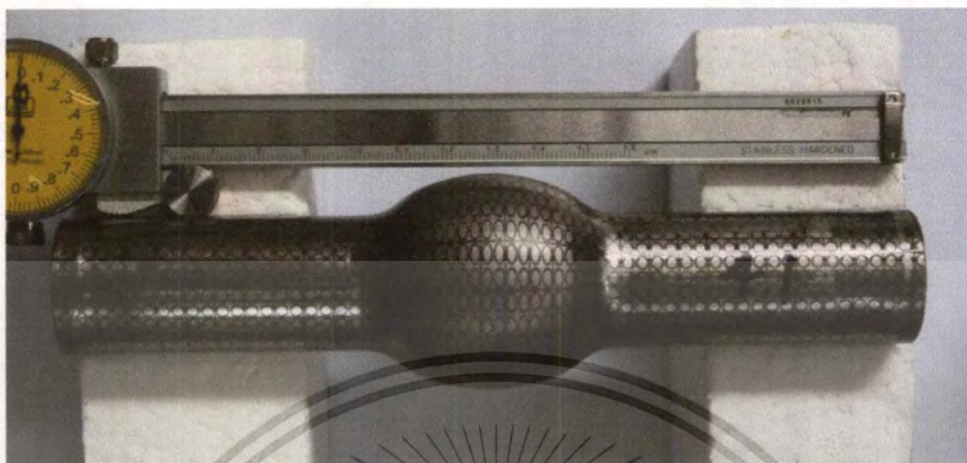


Figure 3.19 A photo of bulged tube for curvature measurement

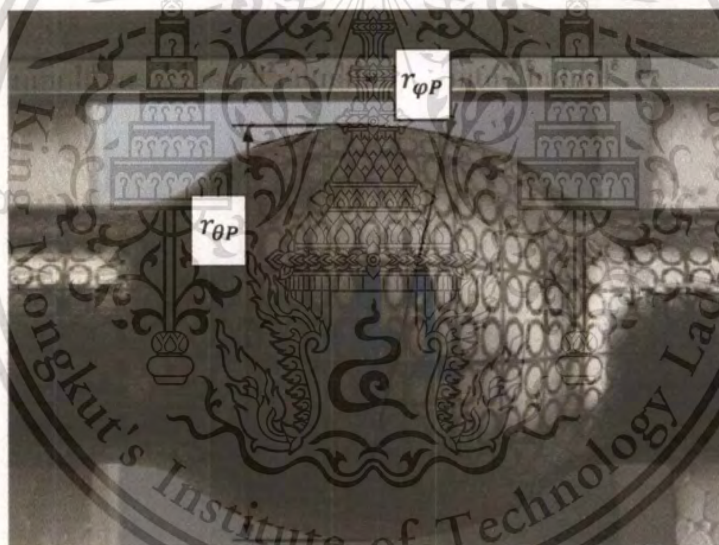


Figure 3.20 Approximation of the curve by CAD software

Then, one can calculate the real deformed grid diameter by following equations.

$$l_1 = 2r_{\theta P} \sin^{-1} \left( \frac{l_1'}{2r_{\theta P}} \right) \quad (3.1)$$

$$l_2 = 2r_{\phi P} \sin^{-1} \left( \frac{l_2'}{2r_{\phi P}} \right) \quad (3.2)$$

Where  $l_1 =$  Major deformation

$l_2 =$  Minor deformation

$l_1' =$  Captured major deformation

$l_2' =$  Captured minor deformation

This material is reserved for educational use only, not allowed for commercial use.

Forbidden to modify the content, and cite the document when use.

## CHAPTER 4

### EXPERIMENTATION AND RESULTS

This chapter explains experimentation and results of the experiments. A hydroforming test machine with axial feeding is designed for the left-hand side data in the forming limit diagram, in which tensile and compressive strains occur. Figure 4.1 shows a hydroforming test machine with axial feeding tooling set. A bulge test apparatus with a fixed bulge length without axial feeding as shown in Fig. 4.2 is used to implement the forming limit experiments to obtain the strain path on right side of the forming limit diagram. This test machine consists of three main parts for supporting the tooling; a hydraulic power system for providing the pressure source of the internal pressure and the feeding punches; and a control system.

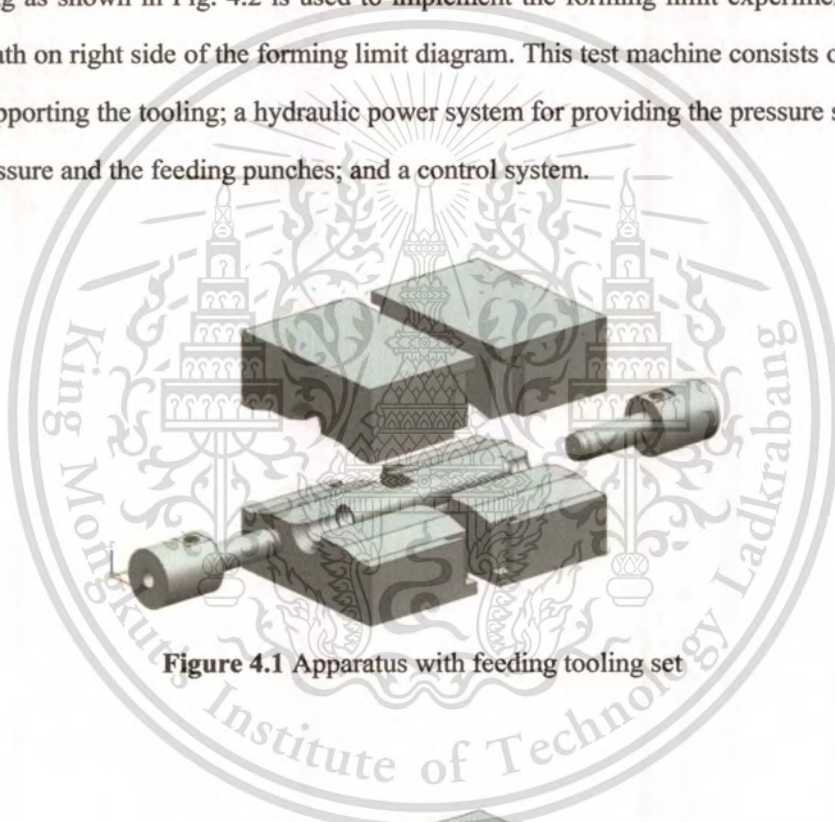


**Figure 4.1** Apparatus with feeding tooling set

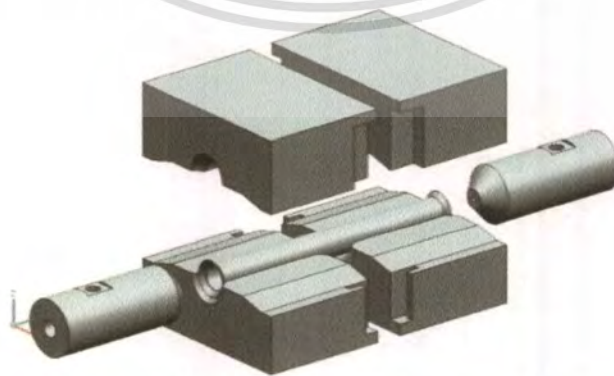


**Figure 4.2** Apparatus without feeding tooling set

### 4.1. Tube Hydraulic Bulge Test

A control system is used to control the forming pressure and the left and right axial feeding distances of the test machine according to the loading paths shown in Figure 4.3-4.4 and tryout in actual process.

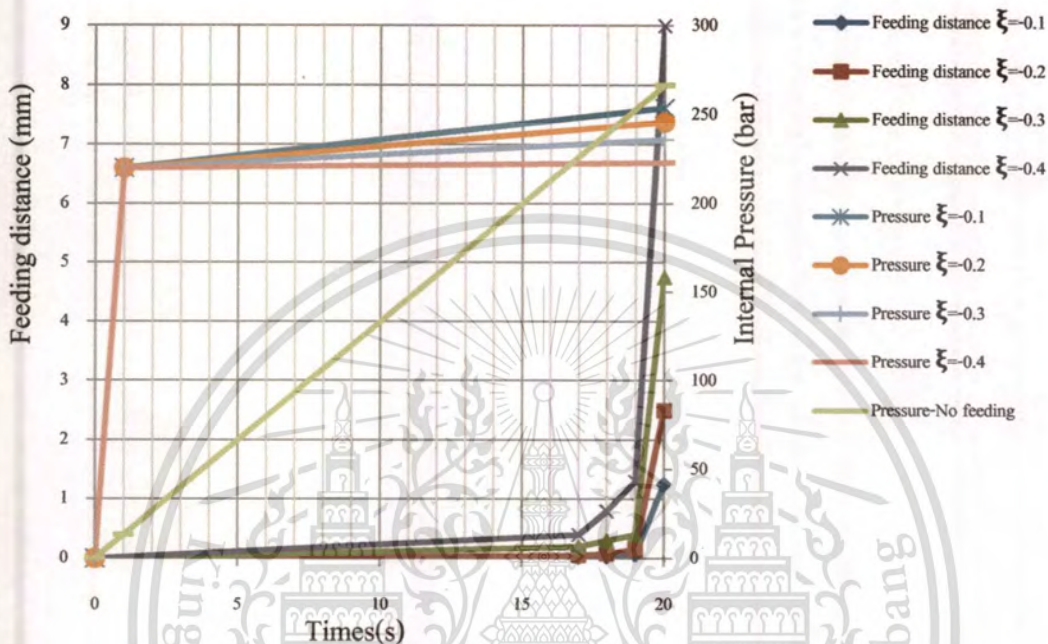


Figure 4.3 Loading path, Feeding distance (mm) and Internal pressure (bar) with time(s)

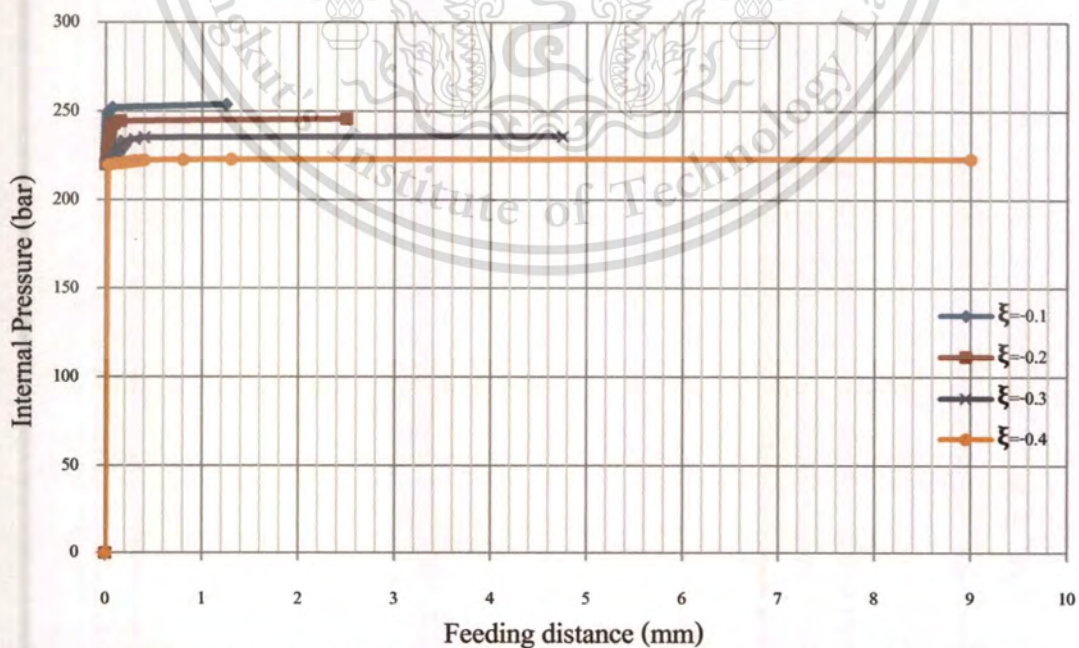


Figure 4.4 Loading path, Feeding distance (mm) with Internal Pressure (bar)

#### 4.1.1. Forming limit experiments with axial feeding

The actual responses of the forming pressures and axial feeding distances during the forming limit experiments are observed and recorded by computer PC-based data logger. Then, grouped correspond actual loading path specimen and separated off the non-corresponding actual loading path specimen. The actual responses are showed in Figure 4.6 and the results of the products after bulge tests with axial feeding for different strain ratios are shown in Figure 4.7. It is known that cracks or bursting lines occur around the pole of the bulged tubes and the maximum bulge height increases with the increase of the absolute value of the strain ratio

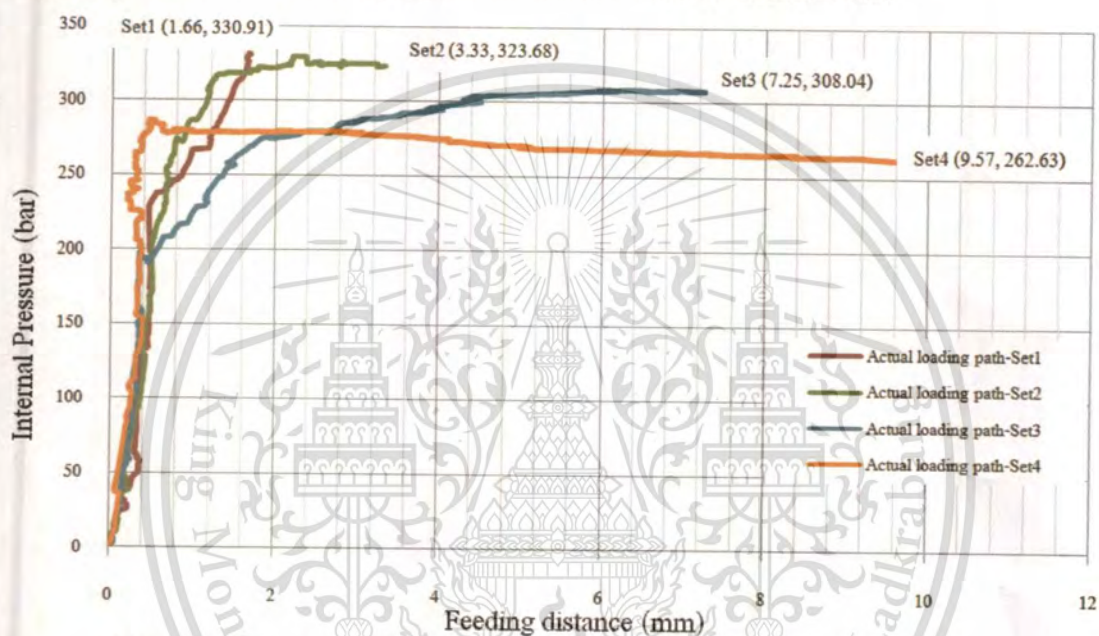


Figure 4.5 Loading path, Feeding distance (mm) with Internal Pressure (bar)

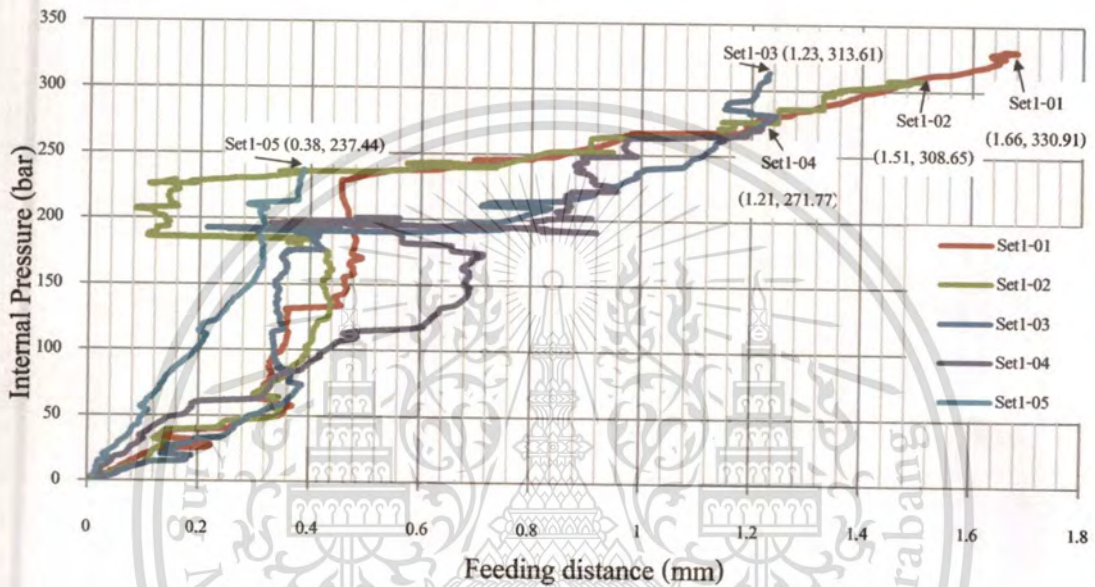


Figure 4.6 Results of the formed product for different strain paths.

This material is reserved for educational use only, not allowed for commercial use.

Forbidden to modify the content, and cite the document when use.

In order to consider the strain path, several forming runs were conducted with the same loading path but were stopped at different deformed states. The set 1-4 loading paths of different deformed state are showed in Figure 4.7-4.10 respectively. First experiment, Feeding distance 1.66 mm is applied at the ends of tube and actual pressure up to 330 bars which is more than expandability of the welding seam; thus the tube burst at welding seam before localized necking occurred. Due to small feeding distance, it was hard to control the end feeding distance and corresponding pressure as results shown in Figure 4.7.



a.) loading path of the formed product of different deformed state-Set1

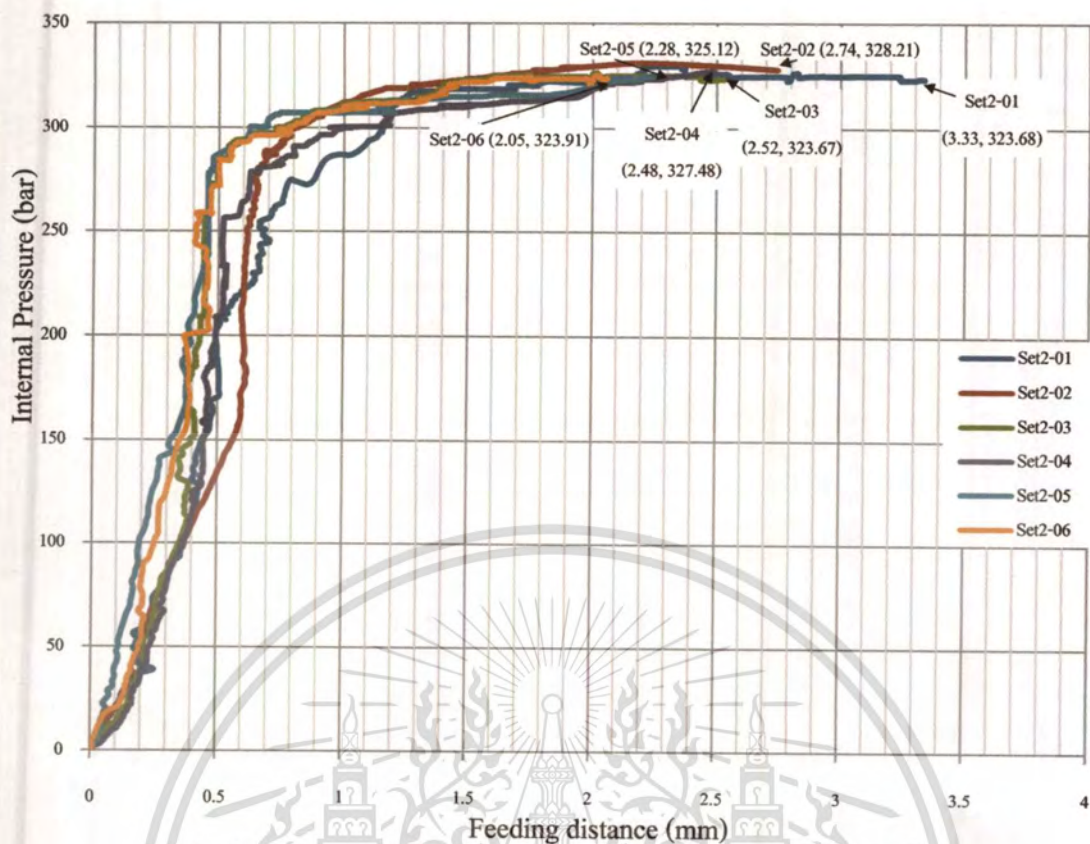


b.) Results of the formed product of different deformed state-Set1

**Figure 4.7** loading path and Results of the formed product of different deformed state-Set1

This material is reserved for educational use only, not allowed for commercial use.

Forbidden to modify the content, and cite the document when use.

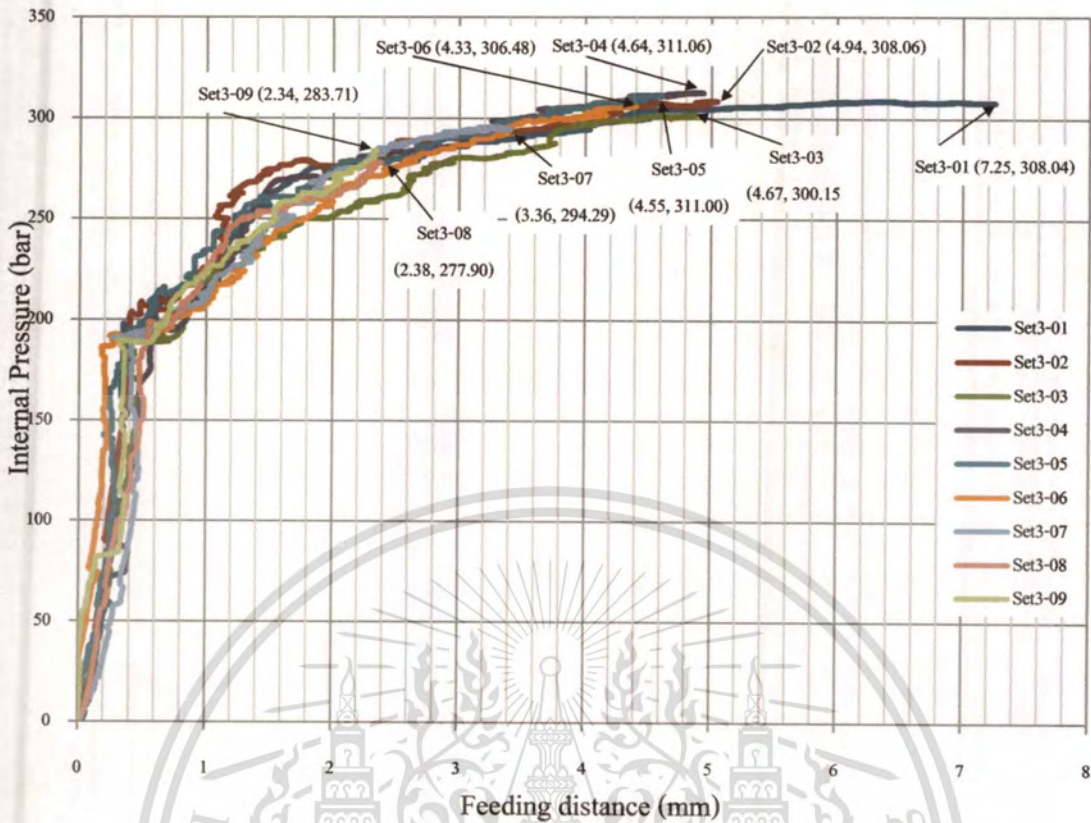


a.) loading path of the formed product of different deformed state-Set2



b.) Results of the formed product of different deformed state-Set2

**Figure 4.8** loading path and Results of the formed product of different deformed state-Set2

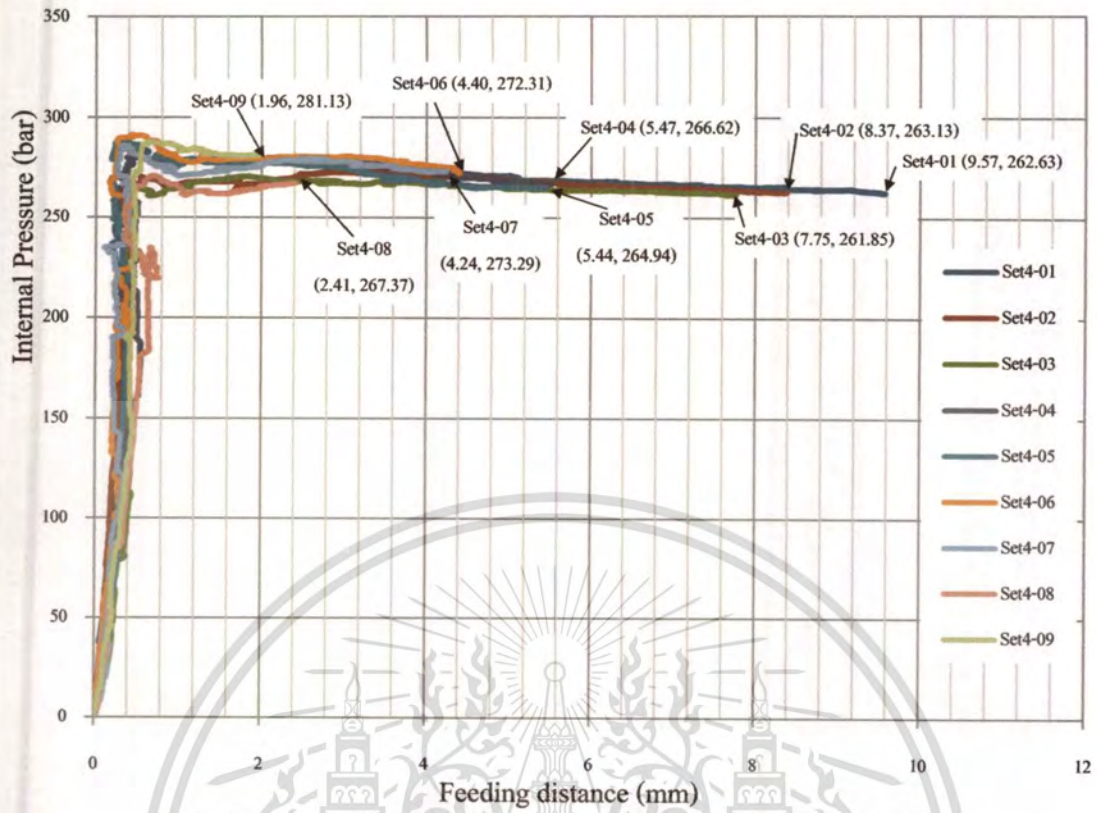


a.) loading path of the formed product of different deformed state-Set3

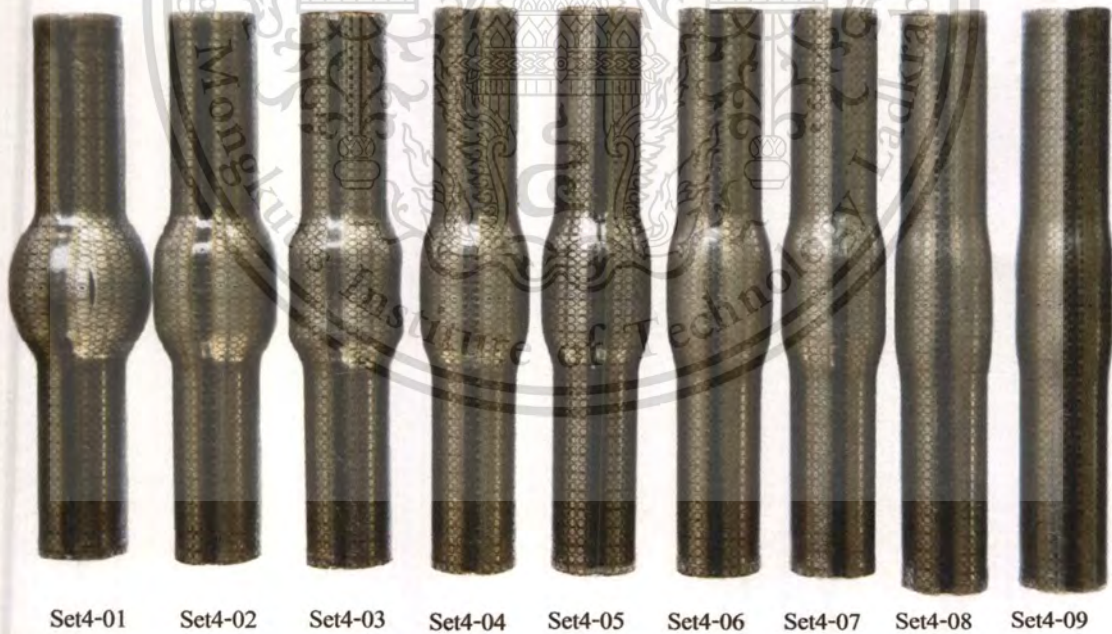


b.) Results of the formed product of different deformed state-Set3

**Figure 4.9** loading path and results of the formed product of different deformed state-Set3



a.) loading path of the formed product of different deformed state-Set4



b.) Results of the formed product of different deformed state-Set4

**Figure 4.10** loading path and Results of the formed product of different deformed state-Set4

#### 4.1.2. Forming limit experiments without axial feeding

A bulge test apparatus with a fixed bulge length without axial feeding are installed for running experiment. The actual responses are showed in Figure 4.11 and corresponding specimen are showed in Figure 4.12

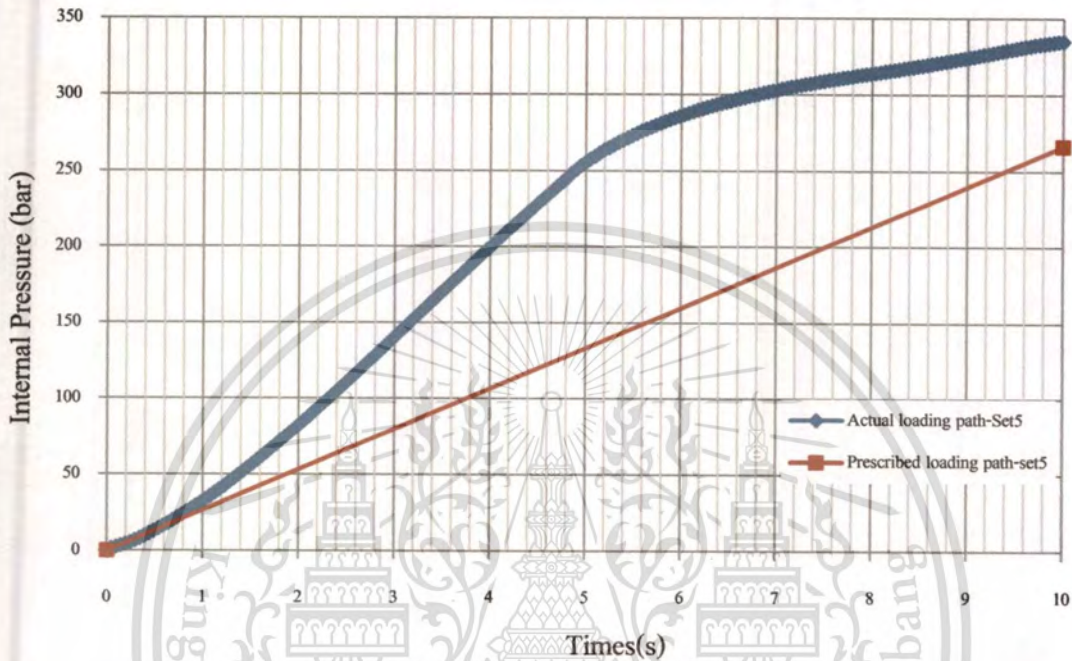
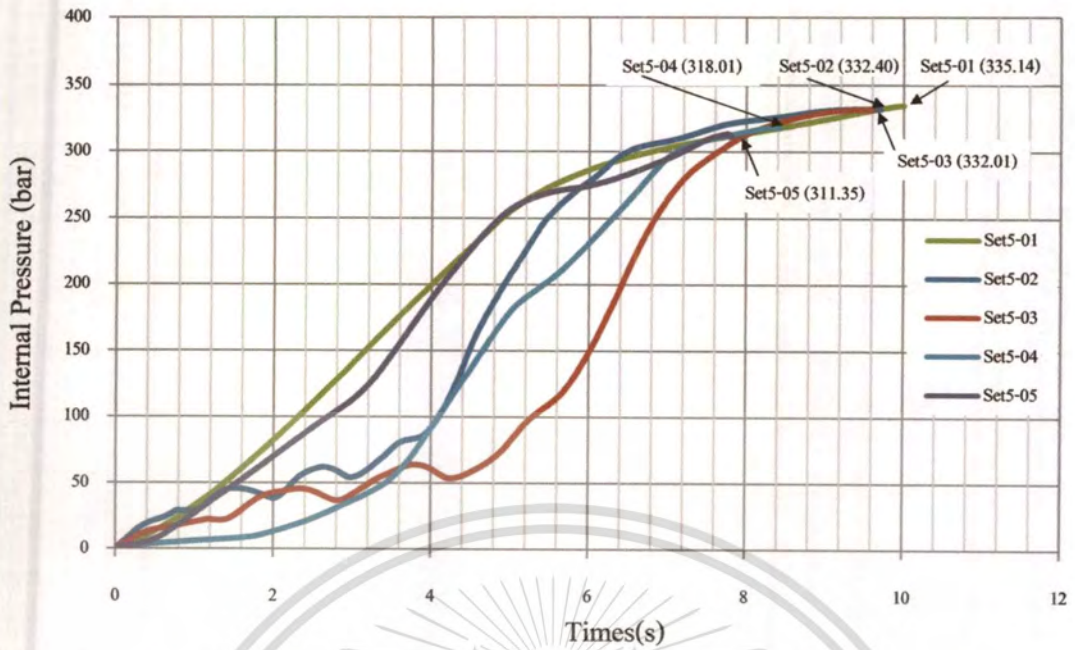


Figure 4.11 Loading path, Internal Pressure (bar) with times(s)



Figure 4.12 Results of the formed product without axial feeding.

In order to consider the strain path, several forming runs were conducted with the same loading path but were stopped at different deformed states. The set 5 loading path of different deformed state are showed in Figure 4.13.



a.) loading path of the formed product of different deformed state-Set5



b.) Results of the formed product of different deformed state-Set5

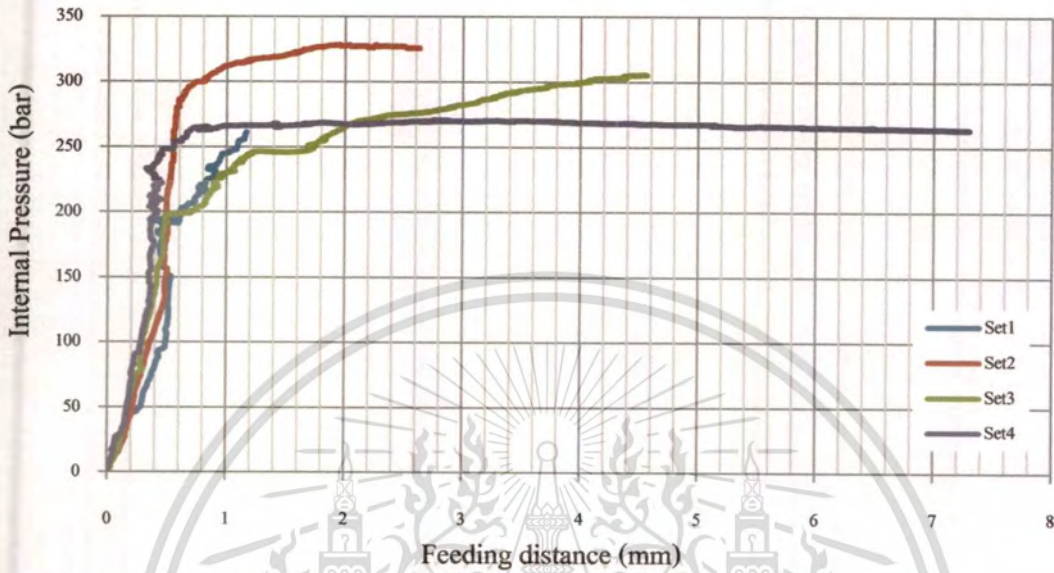
**Figure 4.13** loading path and Results of the formed product of different deformed state-Set5

This material is reserved for educational use only, not allowed for commercial use.

Forbidden to modify the content, and cite the document when use.

#### 4.1.3. Forming limit of welded seam

During ERW tube production, the two edges are welded together by electrical resistance welding (ERW). Because of low quality control of electrical resistance welding process, some specimens burst at welded seam as show in figure 4.14.



a.) loading path of the formed product of specimens that burst at welded seam



Set1

Set2

Set3

Set4

b.) Results of the formed product of specimens that burst at welded seam

**Figure 4.14** The specimens that burst at welded seam and corresponding load path.

## 4.2. Grid Measurement

In order to measure the real deformed length, the grid curvatures are investigated. The digital camera with macro lens is used to capture the shape of bulge tube, which is later used to approximate the curve by CAD software as the result is showed in Table 4.1.

Table 4.1 Grid curvature

Set	Run	$r_{\varphi P}$	$r_{\theta P}$
1	1	95.2175	36.8570
	2	111.8699	35.5000
	3	260.1080	32.7015
	4	863.1291	30.7527
	5	1456.1444	30.3203
2	1	54.6678	40.5605
	2	88.6139	36.5553
	4	157.6746	34.7538
	5	173.8332	33.9585
	3	360.0374	32.0960
	6	514.7792	32.0887
3	1	51.39249147	43.2423
	2	86.16709075	38.2036
	3	83.61262799	38.1561
	4	150.5854701	36.294
	5	105.4080411	37.373
	6	765.8	34.6598
	7	314.9241262	34.416
	8	598.1552901	32.1596
	9	927.0110544	32.0876
4	1	38.49829642	47.425
	2	81.53996599	42.3095
	3	298.443686	38.0171
	4	68.16383701	37.7564
	6	234.4953112	37.7758
	7	511.2414966	35.301
	8	191.229983	36.8714
	9	371.9837746	33.4005
	10	392.3137255	32.3129
5	1	17.3043	86.01104
	2	17.3024	86.21883
	3	18.5348	86.23345
	4	16.3601	259.3944
	5	15.7954	863.2979

This material is reserved for educational use only, not allowed for commercial use.

Forbidden to modify the content, and cite the document when use.

The deformed grid is measured  $\pm 45$  degrees around the welding line as shown in Figure 4.15.

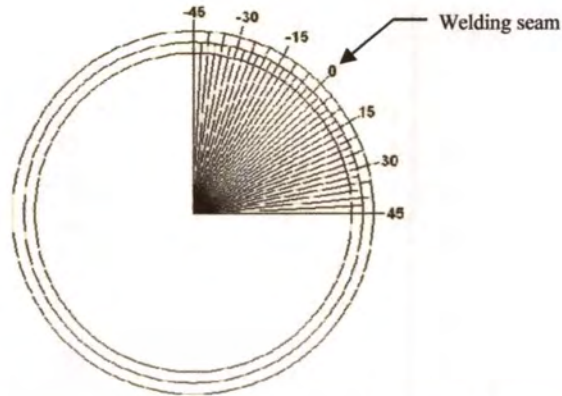


**Figure 4.15** Measure zone covering  $\pm 45$  degrees from welding seam

### 4.3. Construction of the Forming Limit Curve(FLC)

The critical major and minor strains are plotted to construct the forming limit curve (FLC). Figure 4.16 show forming limit curve and the major and minor strains of all specimens covering  $\pm 45$  degrees from the weld line.

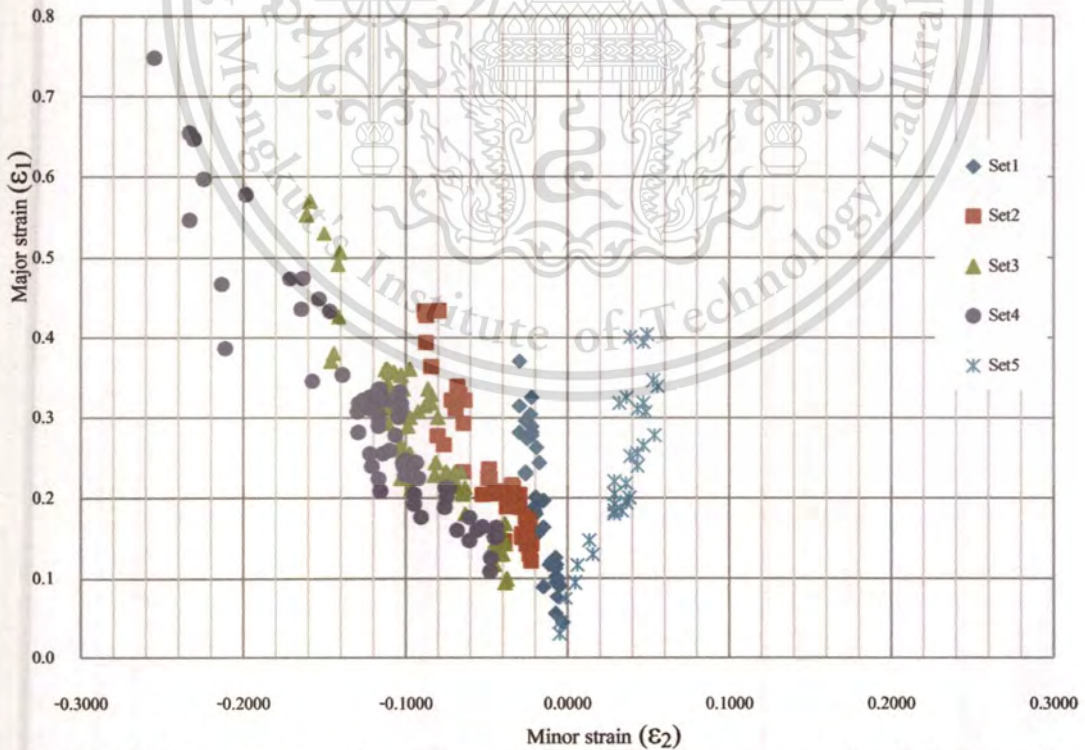
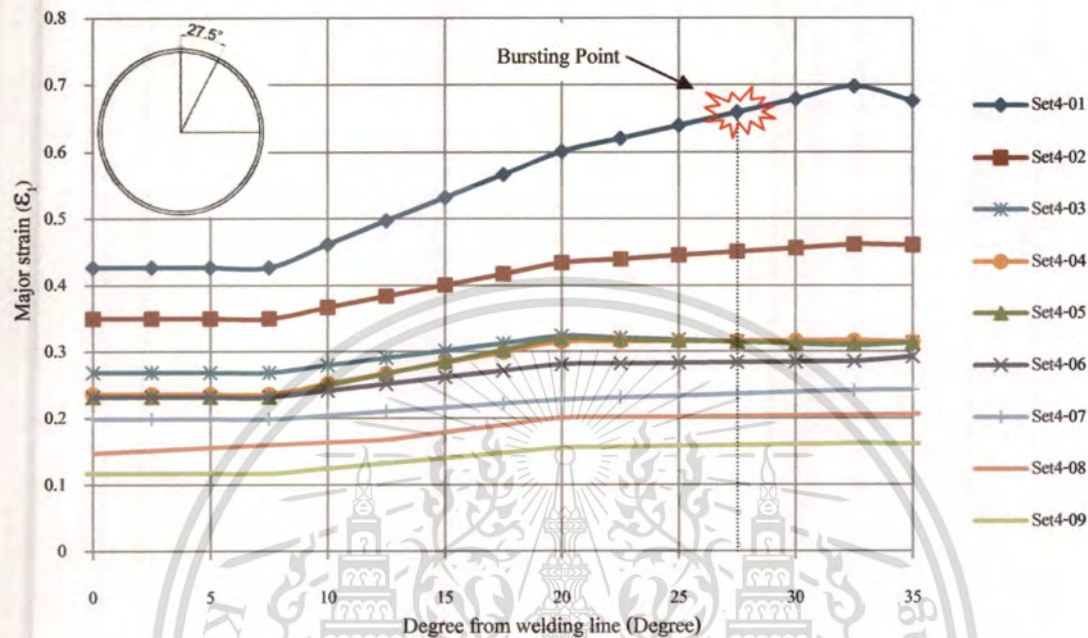


**Figure 4.16** FLC with the major and minor strains of all specimens covering  $\pm 45$  degrees from welding seam

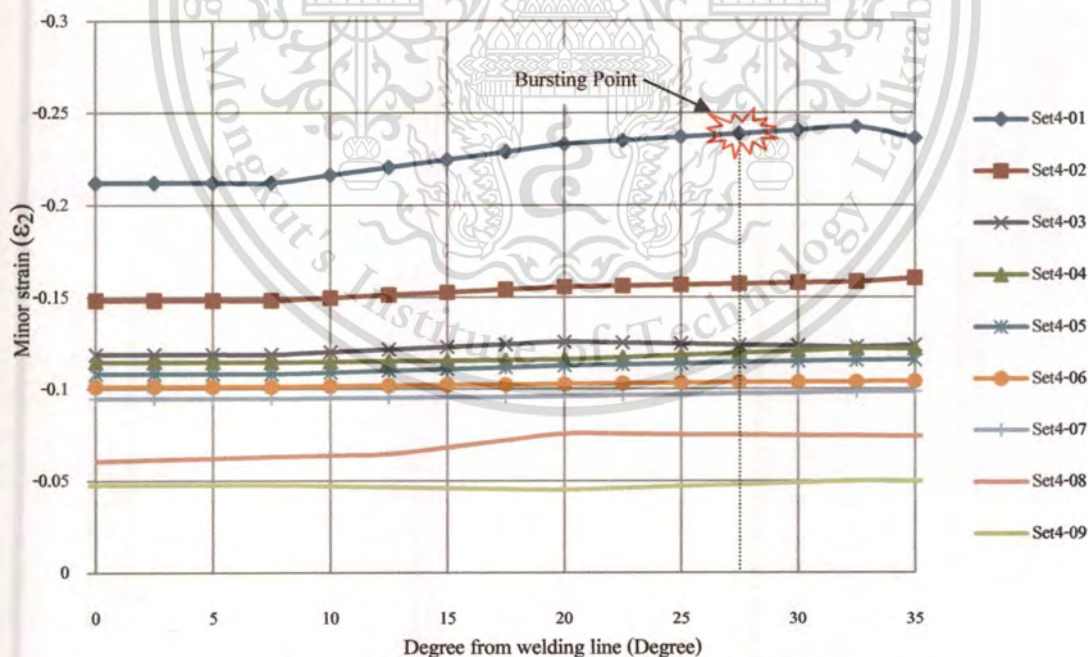
This material is reserved for educational use only, not allowed for commercial use.

Forbidden to modify the content, and cite the document when use.

The deformed characteristic of specimens from welding line to 35 degrees is showed in Figure 4.17. The major and minor strains are smallest at 0-7.5 degrees from welding line, then increasing at 7.5-20 degrees and maintain at 20-35 degree. As a result, the maximum strain between 20 and 35 degree is the representation of strain between 35 and 90 degrees.



a.) The Set4 major strain with degree from welding line



b.) The Set4 minor strain with degree from welding line

**Figure 4.17** The major and minor strain with degree from welding line of Set4

Several researchers (Jieshi Chen, Xianbin Zhou and Jun Chen, 2009) have shown experimentally that non-linear strain path can change the shape and location of the FLC. Nevertheless, to an extent, this effect on the FLC can be minor if the non-linearity is kept small. In order to obtain a standardized assessment of the forming limit curve, the strain path at the apex of the bulged sample has to be controlled as linear as possible (i.e., constant strain ratio). The strain paths at the pole of the forming tube for different strain ratios are shown in the figures 4.18-4.22.

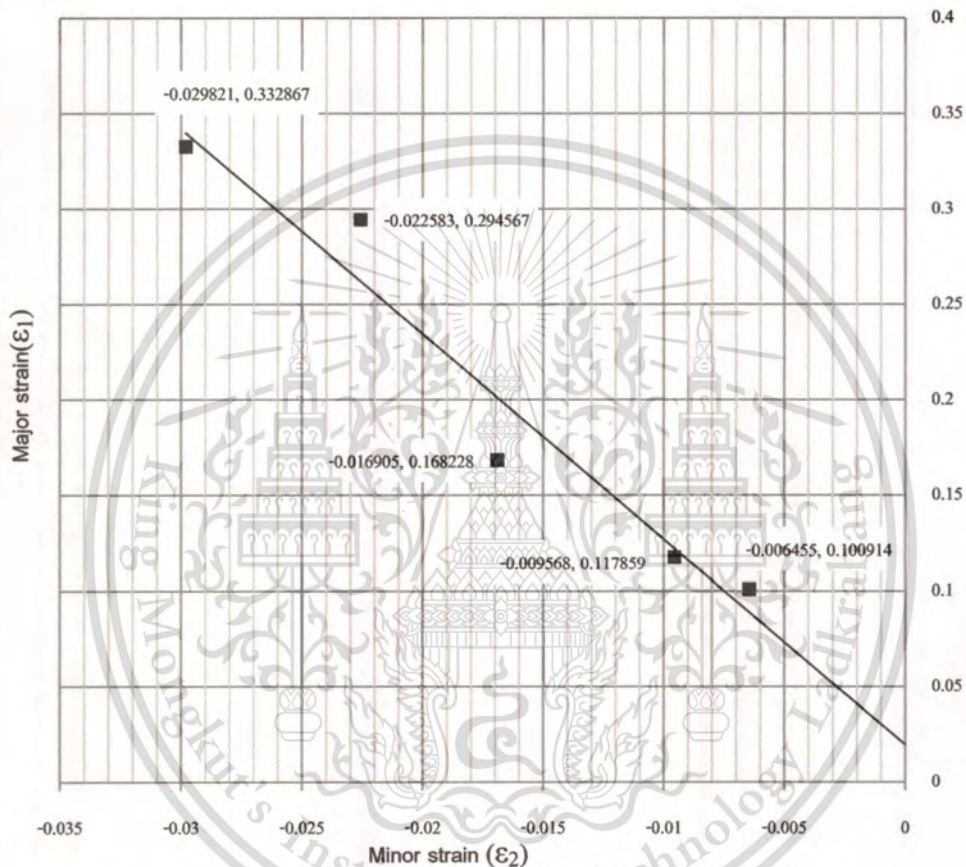


**Figure 4.18** Set1 strain path at 30 degree

Apparently, the least feeding distance used to express the excessive pressure which more than expandability of welding line, consequently the burst appeared at the welding line before a material localized necking appeared; therefore, the critical strain at above condition could not reach to real critical strain.

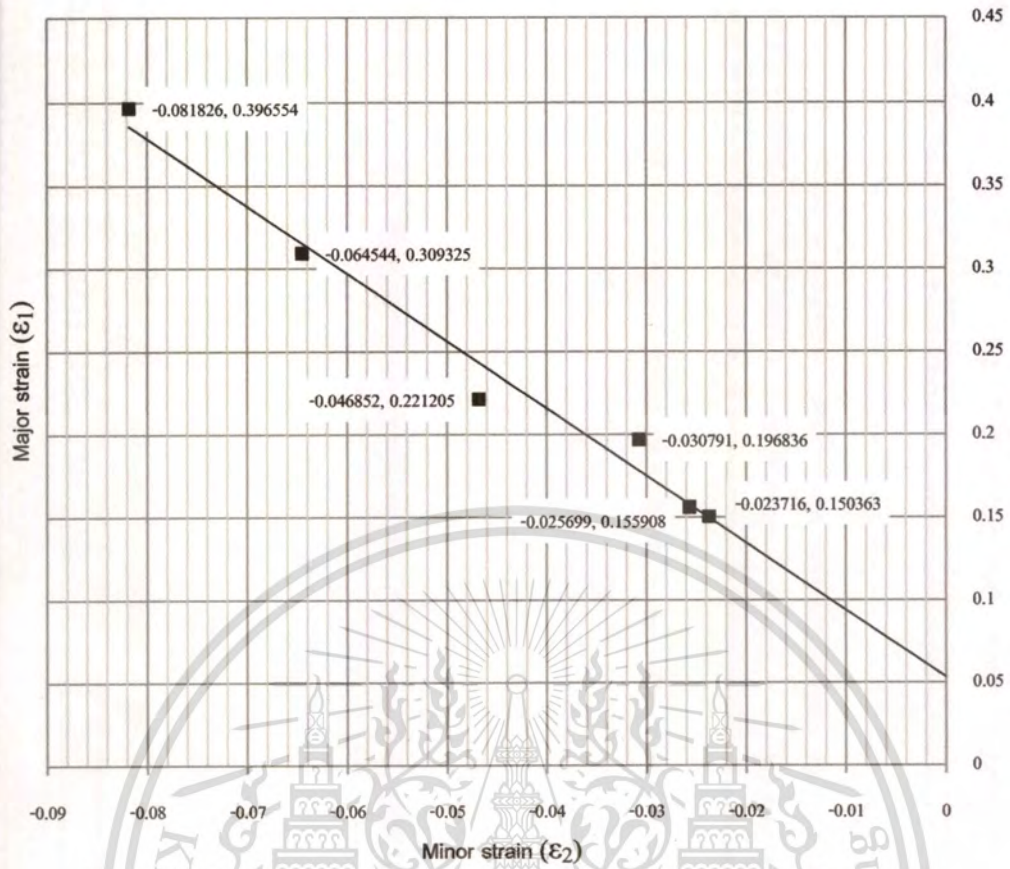


Figure 4.19 Set2 strain path at burst degree (20 Degree) from welding line

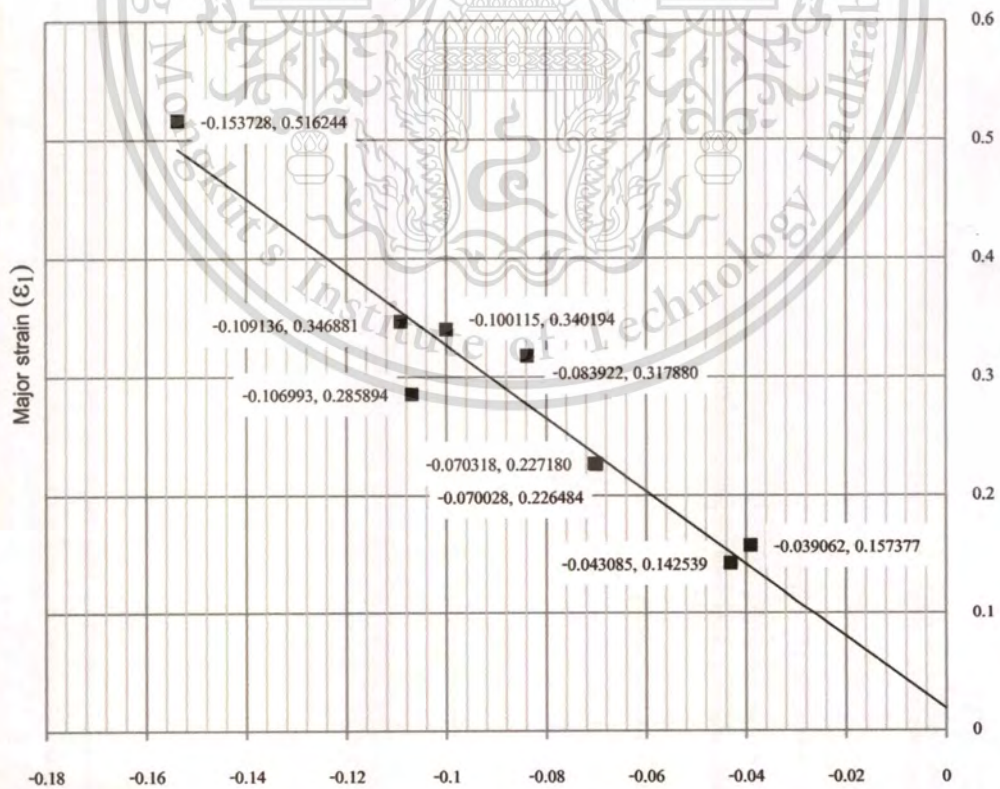
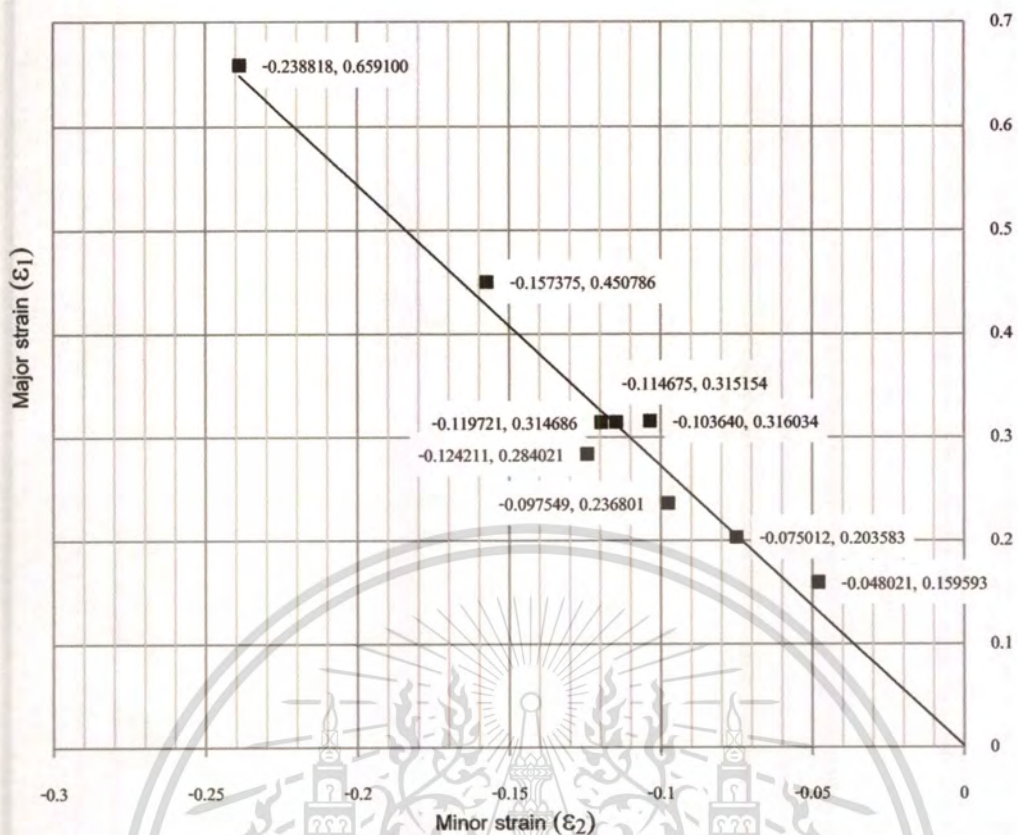


Figure 4.20 Set3 strain path at burst degree (22.5 Degree) from welding line

This material is reserved for educational use only, not allowed for commercial use.

Forbidden to modify the content, and cite the document when use.



**Figure 4.21** Set4 strain path at burst degree (27.5 Degree) from welding line

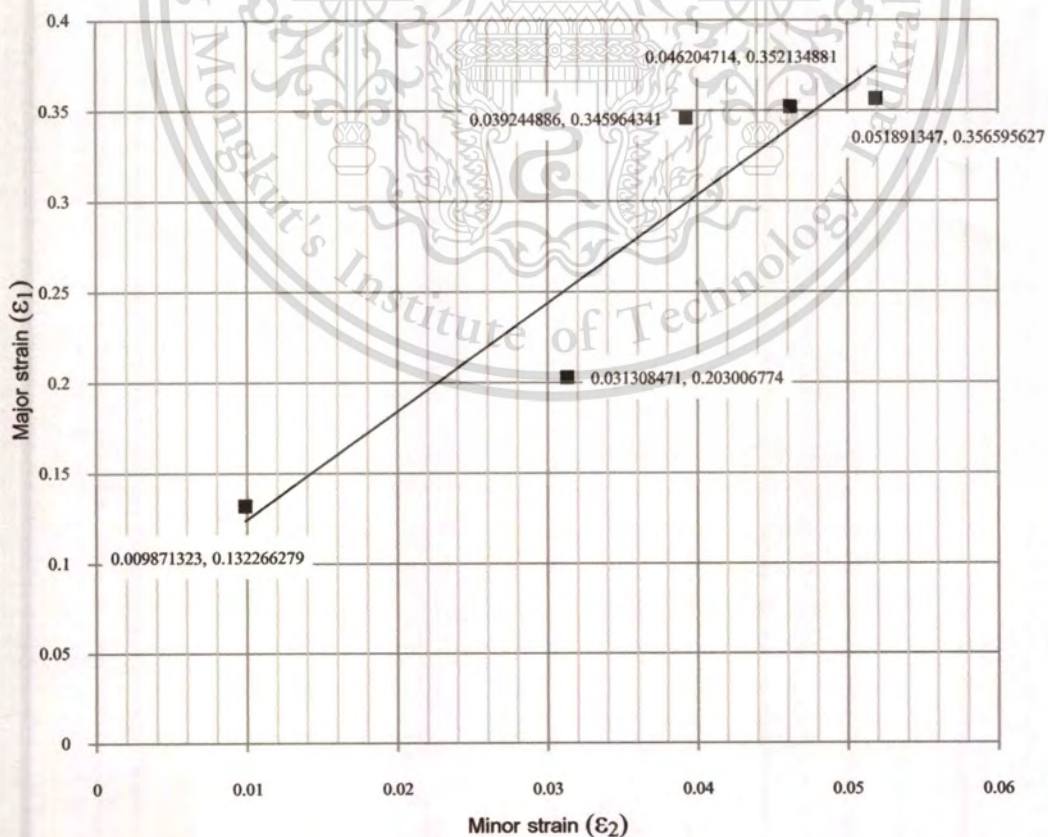


**Figure 4.22** Set5 strain path at burst degree (25 Degree) from welding line

This material is reserved for educational use only, not allowed for commercial use.

Forbidden to modify the content, and cite the document when use.

From the experimental data, the FLD and forming limit curves (FLC) of STKM 11A tubes are constructed as shown in Figure 4.23. The strain paths at the pole of the forming tube for different strain ratios are also shown in the figure. The four strain paths are obtained from experimental data. As the approximate trend lines, the strain paths at the pole of the forming tube for different strain ratios have a trend line of data as linear. The critical strain from the experimental data and the analytical results, the FLD and forming limit curves (FLC) of STKM 11A tubes are constructed as shown in Figure 4.23.

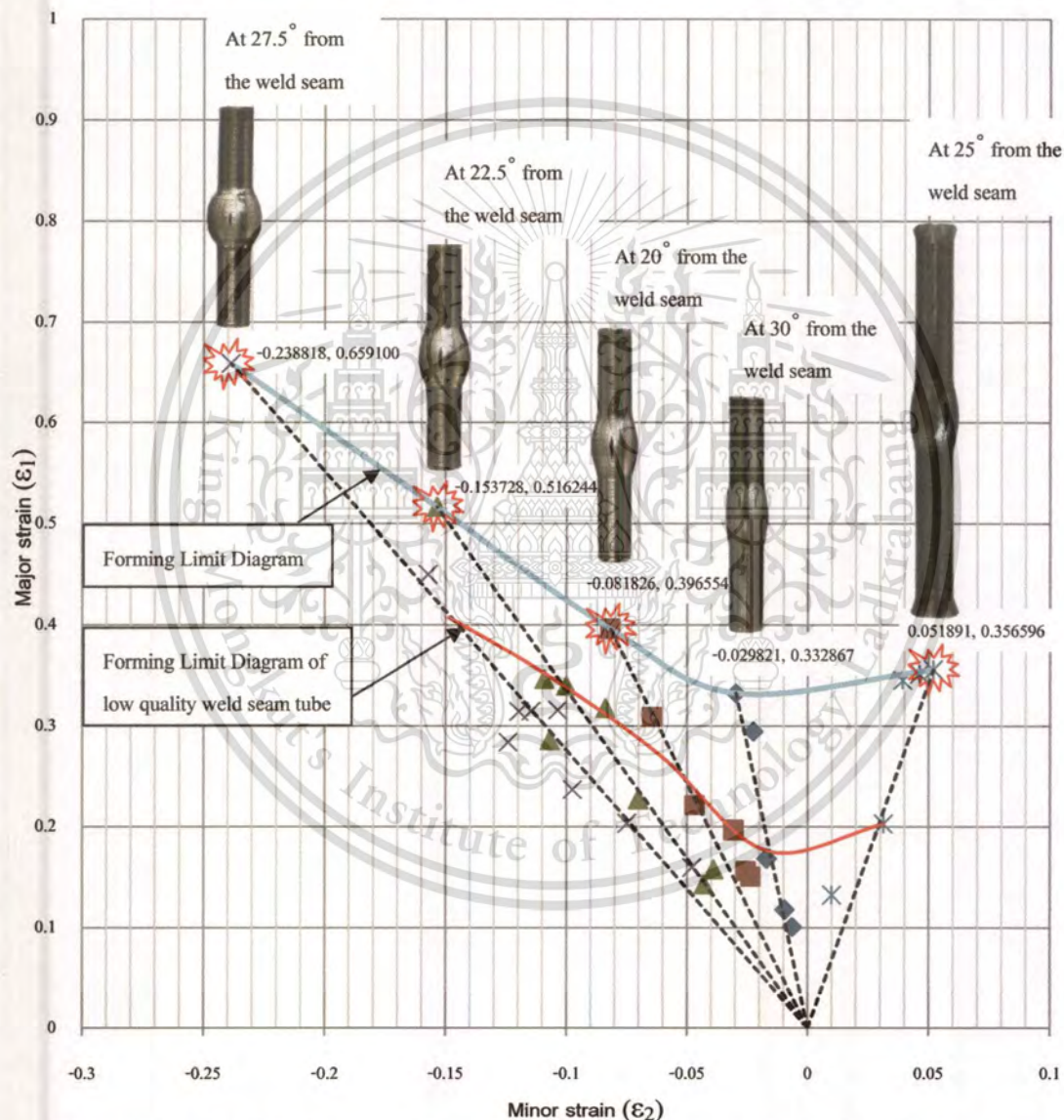


**Figure 4.23** The Experimental FLD and forming limit curves (FLC) of STKM 11A tubes

The weld seam in a tube leads to an obvious non-homogeneity in material properties, and the formability of the weld seam and its heat-affected zone is usually lower than that of the tube, so that tube failures occur closely or on the weld line as shown in Figure 4.23.

This material is reserved for educational use only, not allowed for commercial use.

Forbidden to modify the content, and cite the document when use.

## CHAPTER 5

### COMPARISON AND VERIFICATION

#### 5.1 Empirical FLC, Analytical FLC and Experimental FLC

The formulation of plastic instability criteria and Keeler's formula are analytical FLC and empirical FLC which are used to compare with the experimental FLC, see Figure 5.1. The formulations used are given in chapter 2. The  $n$  value of the flow stress obtained from tensile tests is used to construct the analytical and empirical FLC of STKM 11A tubes. From the chart, the experimental FLC is quite close to the Keeler's formula. The Formulation of plastic instability criteria gives the lowest FLC.

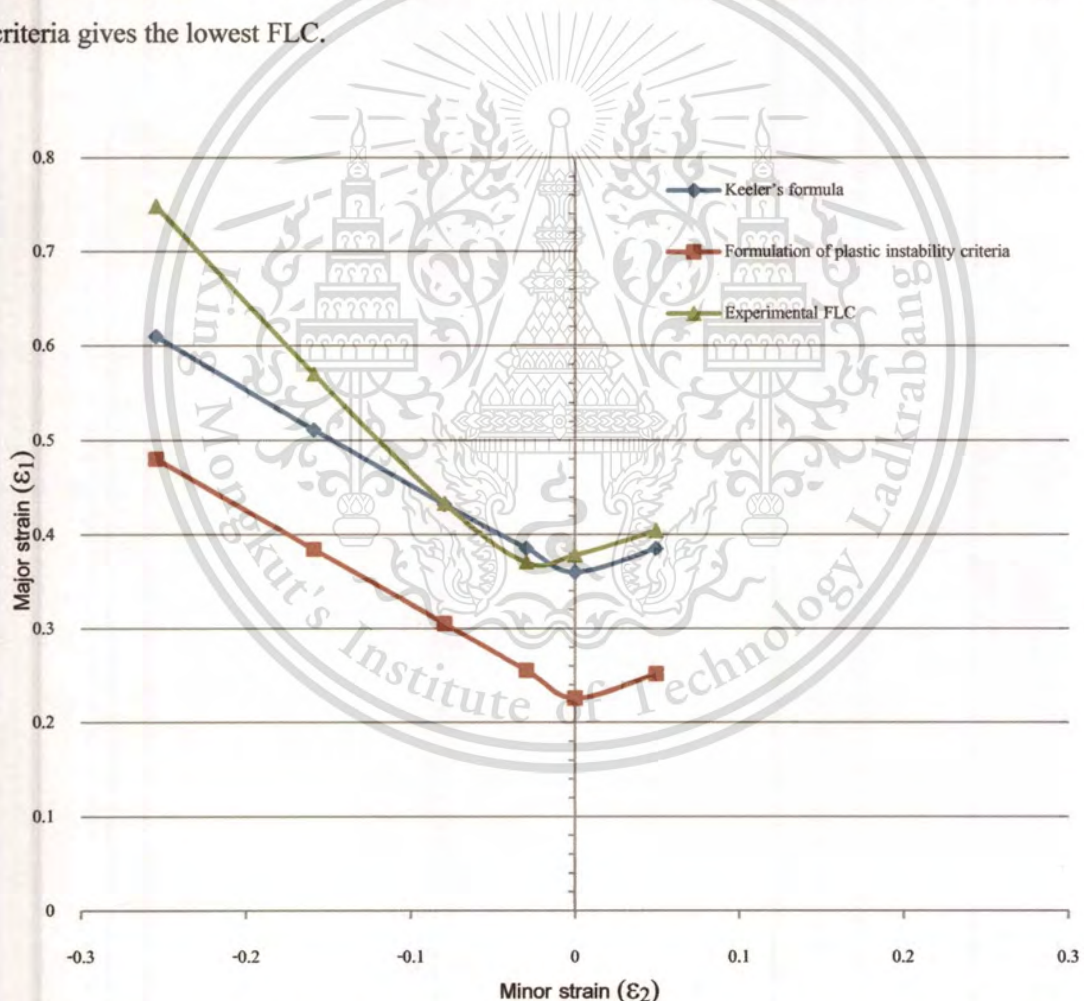


**Figure 5.1** Comparison of predicted forming limit strains with the experimental forming limit strains for low carbon steels STKM 11A.

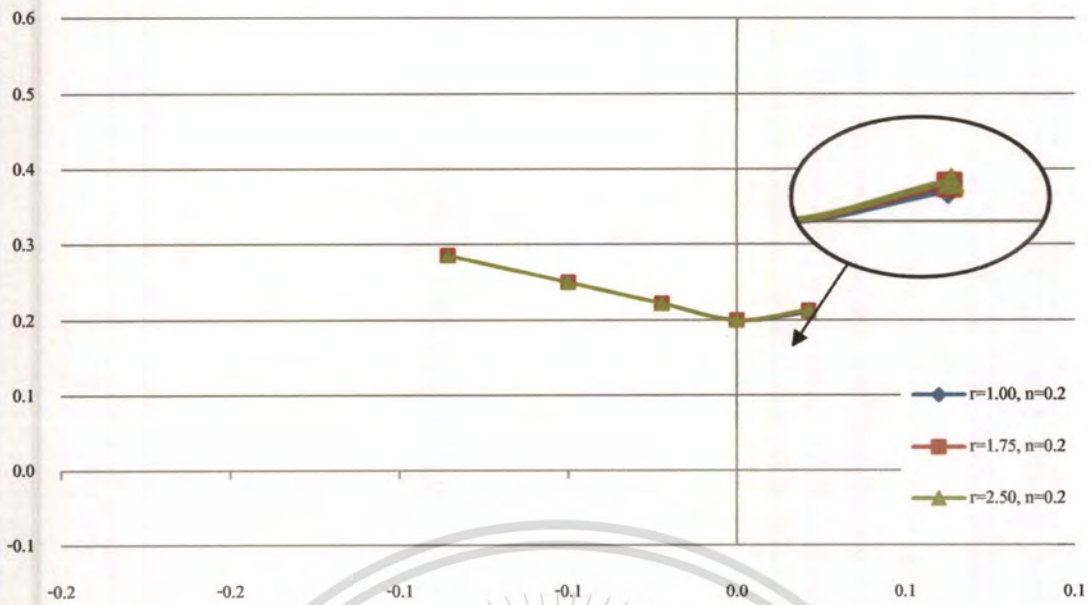


**Figure 5.2** Effects of the  $r$  value on the forming limit curve with Hill's non-quadratic yield function.

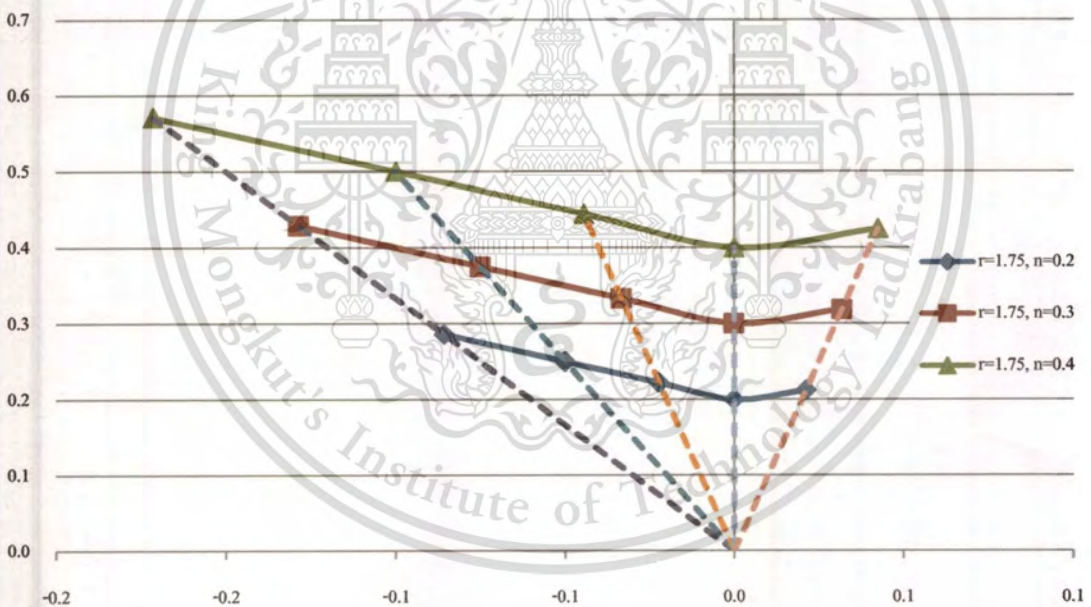


**Figure 5.3** Effects of the  $n$  value on the forming limit curve with Hill's non-quadratic yield function.

Analytical and empirical FLC can be influenced significantly by material properties used. Figure 5.2 shows the effect of the normal anisotropy of the material,  $r$ , on the forming limit curve, using Hill's non-quadratic yield function with  $m=2.0$  and  $n=0.2$ . A larger  $r$  value can give a small raise to the forming limit curve in the tensile–tensile strain region as shown in Figure 5.2. In the tensile–compressive strain region, however, the forming limit curves are not influenced by the

This material is reserved for educational use only, not allowed for commercial use.

Forbidden to modify the content, and cite the document when use.

r value. It seems that the forming limit curves in the tensile–compressive strain region using Hill’s localized necking criterion are not influenced by the m and r values in the Hill’s non-quadratic yield function.

Figure 5.3 shows the effects of the strain-hardening exponent of the tube material, n, on the forming limit curves using Hill’s nonquadratic yield function with  $m=2$  and  $r=1.75$ . It is apparent that the forming limit curves are influenced significantly by the n value. A material with a larger n value undergoes larger plastic deformation before necking occurs, accordingly a larger n value raises the forming limit curves. Based on its formulation, however, it is apparent that the forming limit curve by the formulation of plastic instability criteria is not dependent on the material thickness.

As a result of Comparison of predicted forming limit strains with the experimental forming limit strains for low carbon steels STKM 11A, the Keeler’s FLC lies above the formulation of plastic instability criteria and lies below the experimental FLC. Swift’s diffused necking criterion and Hill’s localized necking criterion associated with Hill’s non-quadratic yield function are developed to derive the critical principal strains at the onset of plastic instability, while the predicted strains at the onset of necking are always smaller than the values measurable or invisible of the neck size. In practical manufacturing, only visible defects are monitored. For this reason, the formulation of plastic instability criteria FLC always underestimates the tube’s visible formability and is over conservative to evaluate the forming severity of parts.

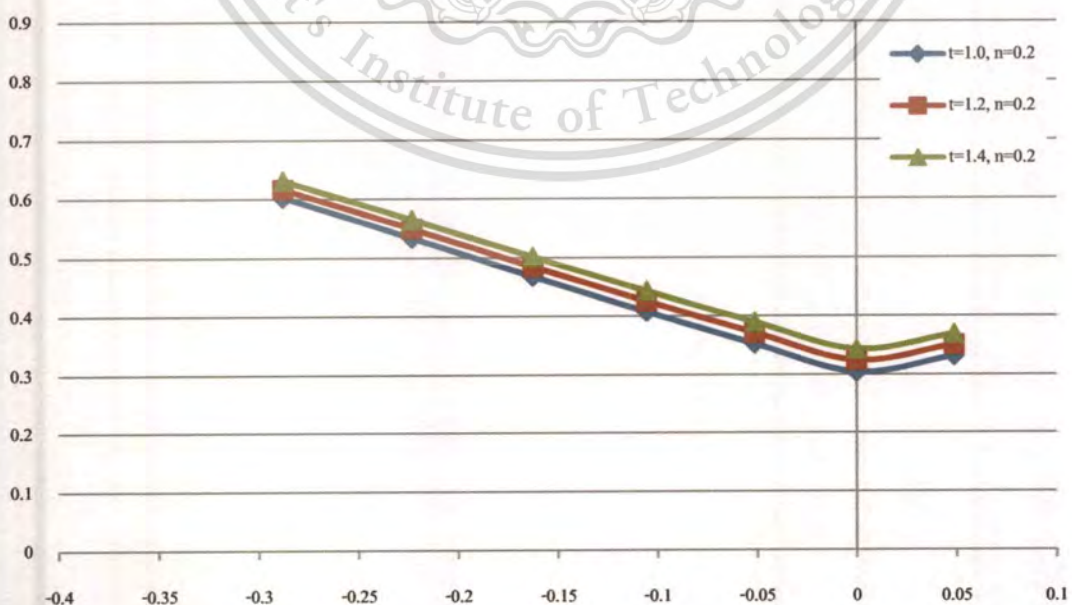
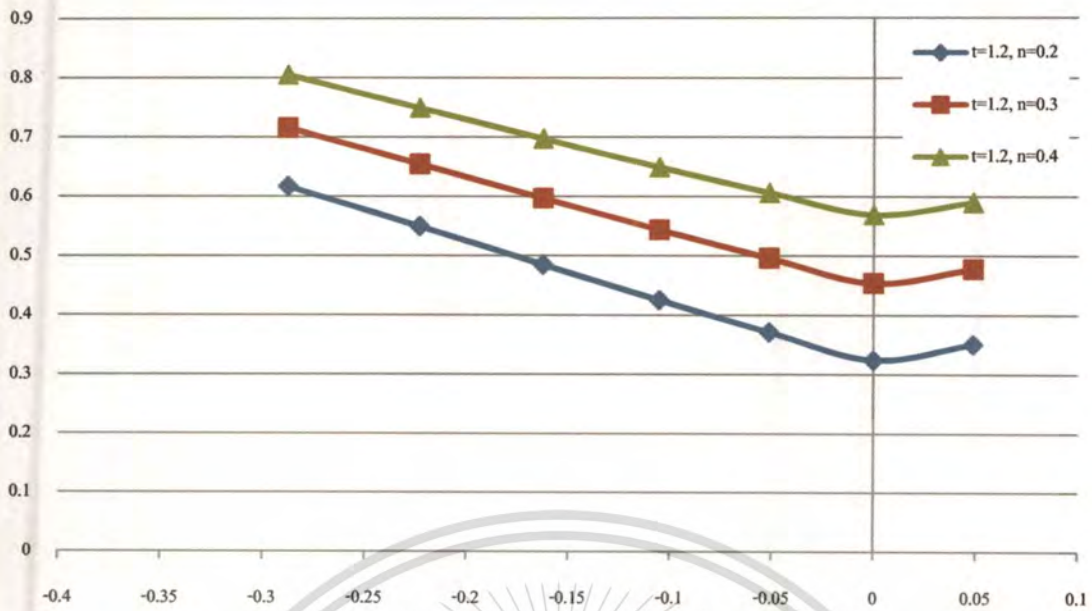


Figure 5.4 Effects of the t value on forming limit curve with Keeler’s formula.



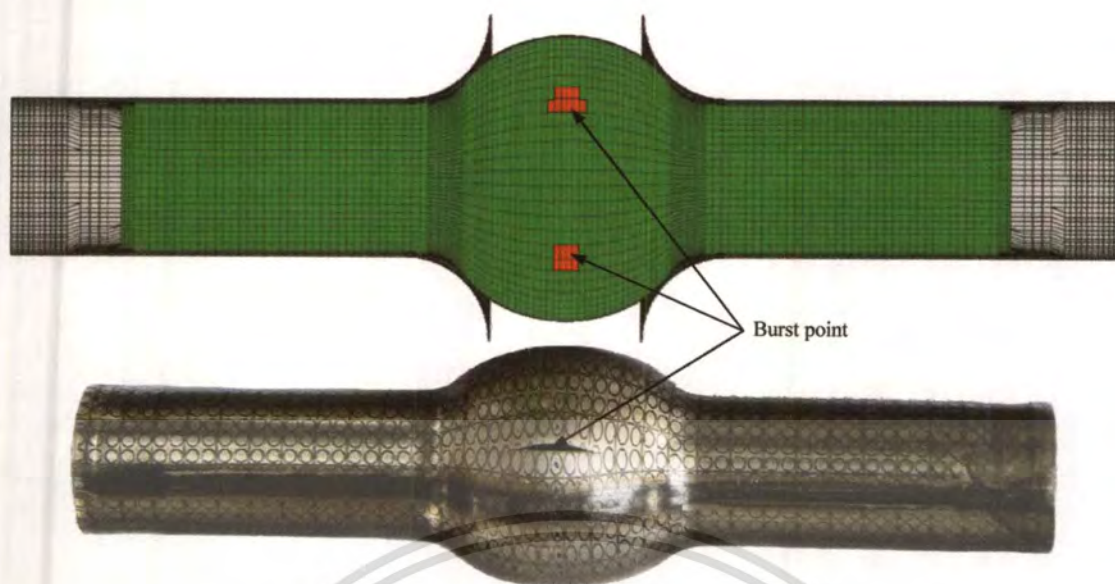
**Figure 5.5** Effects of the  $n$  value on the forming limit curve with Keeler's formula.

Figure 5.4 shows the effects of the thickness,  $t$ , on the forming limit curve, using Keeler's formula with  $n = 0.2$ . Accordingly, a larger  $t$  value can raise the position of forming limit curve as shown in Figure 5.4. Figure 5.5 shows the effects of the strain-hardening exponent of the tube material,  $n$ , on the forming limit curves using Keeler's formula  $t = 1.2$ . It is apparent that the forming limit curves are influenced significantly by the  $n$  value.

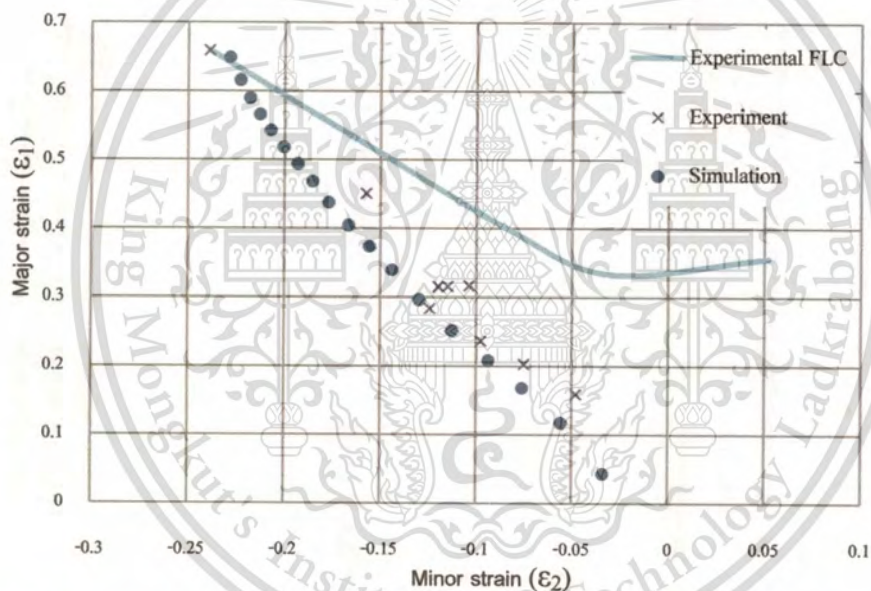
## 5.2 Verification of Experimental FLC

### 5.2.1 Verification of experimental FLC with actual bulge test load path

A specimen in set 4 run number 01 was selected to verify the experimental FLC. An actual load path and real material properties (Experimental FLC,  $k$ ,  $r$  and  $n$  value) were put to test in numerical simulation (Finite Element software: DYNAFORM). The results were found that the final tube in numerical simulation is closely shaped with the formed tube in real experiment as shown in figure 5.6.



a.) Results of the formed product for experiment and numerical simulation



b.) Comparison of major and minor strain for experiment and numerical simulation

**Figure 5.6** Results of comparison for experiment and numerical simulation

During simulations, an elastic-plastic material model considering strain hardening obtained from tensile tests is used. Symbols (X) and (O) represent the major and minor principal strains of the mesh where the real experiment and numerical simulation (Finite Element software: DYNAFORM), respectively. It can be seen that simulated strains closely follow the measured strains. Therefore, FE model can reasonably simulate hydroforming process.

### 5.2.2. Verification of Experimental FLC with a real automotive part

The forming limit curves determined for these tubular materials were put to test in formability evaluations of test parts forming in both real experiment and numerical simulation (Finite Element software: DYNAFORM ). A real automotive part, i.e. a fuel filler pipe (see Figure 5.7), was considered in this study to design proper process parameters.

First, FLC of comparable steel sheet available in DYNAFORM was used to conduct all the simulation runs and burst, shown in Figure 5.8.



**Figure 5.7** A fuel filler pipe geometry.



**Figure 5.8** A final product of fuel filler pipe.

An actual fuel filler pipe load path was put to test in numerical simulation (Finite Element software: DYNAFORM). The results were found that the final tube in numerical simulation is closely shaped with the formed tube in real experiment as show in figure 5.9. Figure 5.10 provides a correlation between data points measured experimentally from strain grid of fuel filler pipe. The predicted FLCs provided from plastic instability criteria and Keeler's formula is plotted in the true axial strain versus the true circumferential strain space. The experiment data

and simulation data of strain grid analysis for fuel filler pipe are plotted as discrete points in the same figure. As observed in Figure 5.10, the experiment data is close to simulation data and close to the experimental FLC. It can be seen that all the measured strains near the crack site are located above the experimental FLC. Also, none of the critical strains (Crack) lie between the experimental FLC and Keeler's FLC. Therefore, from this comparison, the experimental FLC seems to be the best FLC to estimate a necking (i.e. crack) of this particular tubular steel material.



Figure 5.9 A simulation model of fuel filler pipe.

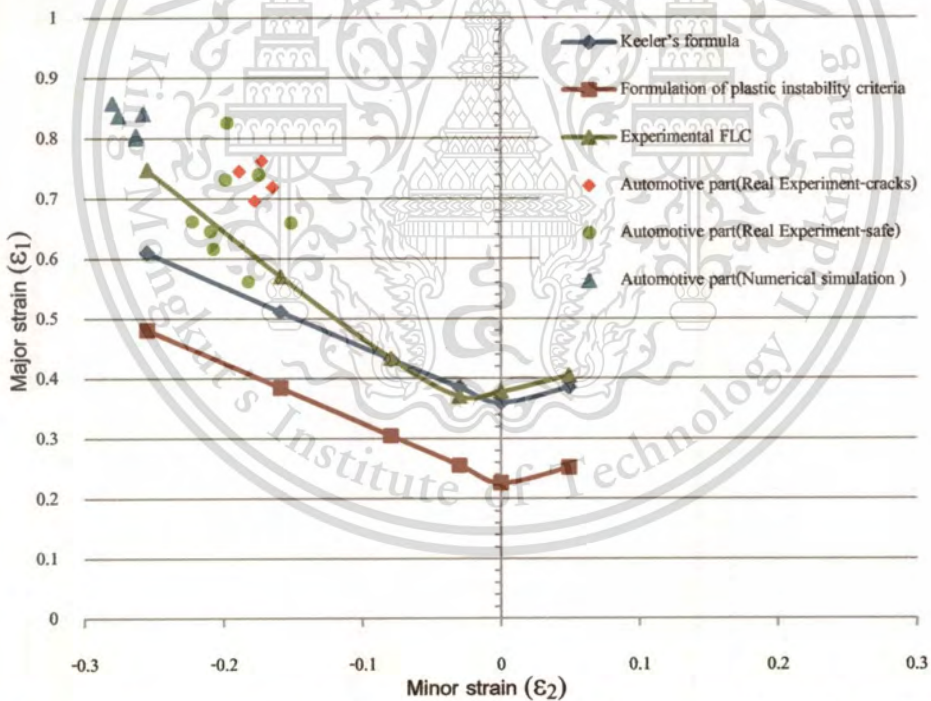


Figure 5.10 Comparison of predicted forming limit strains with measured experimental data.

## CHAPTER 6

# CONCLUSIONS AND SUGGESTIONS

### 6.1 Conclusions

In this study, FEA was used to investigate and determine proper FLC testing die insert geometry, i.e. die entry radius and bulge length, in relation to tube sample geometry, i.e. outer diameter and tube thickness. It was found that the proper die geometry does not depend on sample thickness but only on outside diameter of the sample. A FLC testing apparatus has been designed for commonly used STKM 11A tubing in Thailand. Testing process parameter (loading profiles) were also determined for conducting the test that guarantees linear strain paths in the deforming samples. This knowledge can be applied to design proper FLC testing die inserts for other tubing dimensions. Forming limit curves to be generated using this testing apparatus will be of great usefulness for Thai industry in designing and producing high strength-to-weight ratioed parts using tube hydroforming technology.

FEA was also used to determine the loading paths to be implemented by the hydraulic machine with axial feeding and pressure followed the prescribed loading paths that correspond to the strain paths with a constant strain ratio at the pole of the forming tube. A forming limit diagram from forming limit experiments was successfully using an experimental apparatus with fixed bulge length and a test machine with axial feeding. Analytical forming limit curves were also constructed using Swift's diffused and Hill's localized necking criteria associated with Hill's non-quadratic yield function, and Keeler's formula. From the comparison between the experimental, analytical, empirical FLCs, it was concluded from using a real THF part that the experimental FLC seemed to be able to predict the necking best. The main conclusions from this work can be made as follow.

- A bulge forming apparatus of fixed bulge length and a hydraulic test machine with axial feeding are designed and used to carry out the bulge tests.
- The loading paths of four different strain paths can generate strain paths with a linear strain path at the pole of the forming tube.
- The forming limit curve (FLC) of tubular material low carbon steels commonly used in Thai industry, namely STKM 11A is determined

This material is reserved for educational use only, not allowed for commercial use.

Forbidden to modify the content, and cite the document when use.

- The forming limit curve (FLC) is verified with real part forming experiments for actual application accurately seems to be not appropriate for THF.
- The welding line quality of ERW tube in Thai industry is low quality.

## 6.2 Suggestions for Future Work

Although this work is finished, there are some suggestions to the work for further study determination of forming limit curves of tubular materials for hydroformability evaluation of automotive parts

- Study effect of weld line expandability on formability in hydroforming of ERW tubes.
- Improvement of steel tubing production toward proper usage for THF technology.



## REFERENCES

1. Ahmetoglu M. **Tube hydroforming: current research, applications and need for training.** Journal of Materials Processing Technology 98 (2000) 224-231
2. Altan T. **Evaluation of tube formability and material characteristics.** Journal of Materials Processing Technology 98 (2000).
3. Asnafi N. **Theoretical and experimental analysis of stroke-controlled tube hydroforming.** Materials Science and Engineering A279 (2000) 95–110
4. Chen J. **Sheet metal forming limit prediction based on plastic deformation energy.** Journal of Materials Processing Technology (2009)
5. Chu E. **Influences of generalized loading parameters on FLD predictions for aluminum tube hydroforming.** Journal of materials processing technology 196 (2008) 1–9
6. F. Dohmann **Hydroforming - a method to manufacture light-weight parts.** Journal of Materials Processing Technology 60 (1996) 669-676
7. Hwang Y.M. **Analysis of tube bulge forming in an open die considering anisotropic effects of the tubular material.** International Journal of Machine Tools & Manufacture 46 (2006) 1921–1928
8. Hwang Y.M. **Forming limit diagrams of tubular materials by bulge tests.** Journal of Materials Processing Technology (2009).
9. Kang S.B. **Analytical and numerical approach to prediction of forming limit in tube hydroforming.** International Journal of Mechanical Sciences 47 (2005) 1023–1037
10. Koc M. **Hydroforming for advanced manufacturing.** Woodhead publishing in materials
11. Koc M. **On the characteristics of tubular materials for hydroforming experimentation and analysis.** International Journal of Machine Tools & Manufacture 41 (2001) 761–772
12. Koc M. **Prediction of forming limits and parameters in the tube hydroforming process.** International Journal of Machine Tools & Manufacture 42 (2002) 123–138
13. Lei P.L. **Bursting failure prediction in tube hydroforming processes by using rigid-plastic FEM combined with ductile fracture criterion.** International Journal of Mechanical Sciences 44 (2002) 1411–1428
14. Nefussi G. **Coupled buckling and plastic instability for tube hydroforming.** International Journal of Mechanical Sciences 44 (2002) 899–914

This material is reserved for educational use only, not allowed for commercial use.

Forbidden to modify the content, and cite the document when use.

15. Sonobe O. **Effect of Mechanical Properties on Formability in Hydroforming of ERW tubes.** JFE STEEL Corp., Steel Research Labs., JAPAN
16. Takuda H. **Finite element analysis of limit strains in biaxial stretching of sheet metals allowing for ductile fracture.** International Journal of Mechanical Sciences 42 (2000) 785-798
17. Takuda H. **Prediction of forming limit in bore-expanding of sheet metals using ductile fracture criterion.** Journal of Materials Processing Technology 92-93 (1999) 433-438
18. Takuda H. **The application of some criteria for ductile fracture to the prediction of the forming limit of sheet metals.** Journal of Materials Processing Technology 95 (1999) 116-121
19. Vollertsen F. **On possibilities for the determination of the coefficient of friction in hydroforming of tube.** Journal of Materials Processing Technology 125-126 (2002) 412-420.
20. Xing H.L. **Numerical analysis and design for tubular hydroforming.** International Journal of Mechanical Sciences 43 (2001) 1009-1026
21. Yannis P. **Inflation and burst of anisotropic aluminium tubes for hydroforming applications.** International Journal of Plasticity 24 (2008) 509-543
22. Yoshida K. **Effect of strain hardening behavior on forming limit stresses of steel tube subjected to nonproportional loading paths.** International Journal of Plasticity 23 (2007) 1260-1284

**APPENDIX A**  
**2<sup>nd</sup> INTERNATIONAL CONFERENCE ON GREEN  
AND SUSTAINABLE INNOVATION 2009**

**Appendix A-1:** Determination of forming limit curves of tubular materials for  
hydroformability evaluation of automotive parts



This material is reserved for educational use only, not allowed for commercial use.

Forbidden to modify the content, and cite the document when use.

## Determination of forming limit curves of tubular materials for hydroformability evaluation of automotive parts

Ramil Ketvorakul<sup>1</sup> ; Suwat Jiratheranat<sup>2</sup> ; Naoto Ohtake<sup>3</sup> ; Monsak Pimsarn<sup>4</sup>

TAIST Tokyo Tech Automotive Engineering (International Program)

National Metal and Materials Technology Center, Thailand, Pathumthani, Thailand

International College, King Mongkut's Institute of Technology Ladkrabang, Ladkrabang, Bangkok, Thailand

Email: pupay\_kmitl@hotmail.com, Tel: 08-6505-0968, +66-2329-8056, +66-2326-4729 Fax: +66-2329-8261

### Abstract

Tube hydroforming technology is a new forming process used to form automotive parts out of tubular blank materials such as low carbon steel tubes. The aim of this research is to design proper die insert geometry and testing process parameters for experimental determination of Forming Limit Curves (FLC) of steel tubes commonly used in Thai Industry. Finite element analyses (FEA) are conducted to determine proper FLC test die entry radius and bulge length that allow the test samples to deform with linear strain path—a necessary requirement for FLC determination. In this work a common carbon steel tubing grade STKM 11A, with 28.6 mm outer diameter and 1.2 mm thick is studied. An FLC test die set and test samples are designed. The testing procedure is described in this paper. Design of process parameters is also carried out using FEA for hydroforming of a fuel filler pipe to demonstrate the use and significance of FLC.

**Keywords:** Tube hydroforming process; Forming limit curve; FLC; Tube Bulge Test

### 1. Introduction

Transportation of people and goods has always been one of the sectors that consume most of energy resources and continuing to increase the consumption level at a rapid rate. Design and production of high strength-to-weight ratioed automotive parts is now encouraged or even enforced in most developed countries. Tube hydroforming technology is a promising new forming process that produces tubular automotive parts with significant weight reduction.

Tube hydroforming is a tubular material-forming process that uses a pressurized fluid in place of hard tooling, i.e. punch, to plastically deform a given blank material into a desired shape. With this technique, more complex shapes with increased strength and reduced weight can be manufactured as compared with stamping, forging or casting processes

The forming limit diagram (FLD) of tubular materials should be established, because it directly influences the formability of the

hydraulic forming processes. A few studies concerning the loading paths or the forming limit of tubes and sheets have been reported. For example, Jieshi Chen (2009) study Sheet metal forming limit prediction based on plastic deformation energy, the sheet metal forming limit is calculated by fitting curve from experimental data. The forming limit curves determined for these sheet materials were put to test in formability evaluations of test parts forming in both real experiment and numerical simulation that in this study he selected sheet material ST14 with 0.8 and 0.85 mm thick. Yeong-Maw Hwang (2008) uses bulge tests to establish the forming limit diagram (FLD) of tubular material AA6011 are compared with the forming limits from the analytical FLCs using the  $n$  values obtained by tensile tests and bulge tests. E. Chu and Yu Xu (2008) show summarizes the Investigators which investigated the prediction of forming limit diagrams (FLDs) for tube hydroforming and present their study. Calculated and plotted to FLD and Comparison of predicted forming limit strains with measured experimental data for 6061-T4 seamless extruded tubes.



Fig. 1 Example tube hydroformed parts: a 2004 Ford F-150, chassis frame

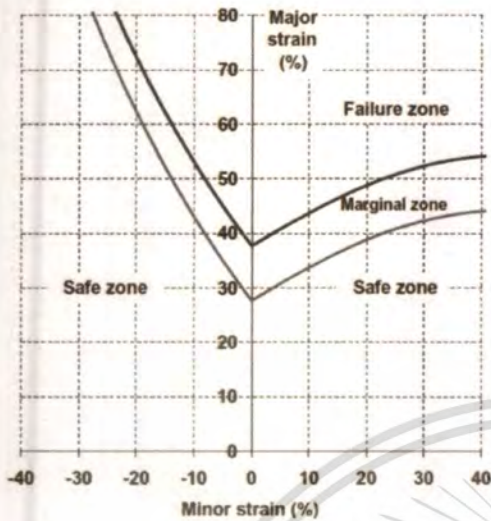
From the literatures reviewed, it is clear that experiment determination of FLC using a hydraulic bulging tube apparatus is necessary for accurate tube hydroforming part and process design. However, the development of such apparatus is still unclear. Therefore, this study focuses on the design and development of FLC testing die insert and proper testing process parameters. A commonly used low carbon steel tubing, STKM 11A, is chosen to be the target material of this study.

## 2 Strain-based forming limit curve

The concept of a forming limit for sheet metal alloys was pioneered by Keeler and Backofen (1963) and Goodwin (1968). They experimentally determined forming limits by measuring the principal surface strains on sheet specimens formed to the onset of localized necking. Keeler and Goodwin also generated forming limit diagrams (FLD) in principal strain space in which a forming limit curve (FLC) represents the boundary beyond which there is a risk of necking for a given sheet metal. Therefore, combinations of principal surface strains that place below the FLC lead to a safe forming operation, whereas those that place above it lead to failure. (Muammer Koç, 2008)

Circular grids are electrochemically etched onto the surface of sheet steel samples. After the tests, Dimensions of the grid circles at the pole will be measured to calculate true major and minor strains by Eqs. (1)-(2), Fig. 3. The critical major and minor strains are plotted to construct the forming limit curve (FLC) for sheet steel material.

Since many tubes used for hydroforming applications are roll-formed from rolled sheet, it was argued that the concept of the FLD (i.e. from



sheet steel) equally applies to tubes. There are important reasons why the standard FLC is not generally applicable to tubular hydroformed parts. One of them being the fact that the roll – forming process of a sheet steel into a tube will incur pre – strained conditions onto the fresh tube. This is known to affect FLC even in the steel sheet forming

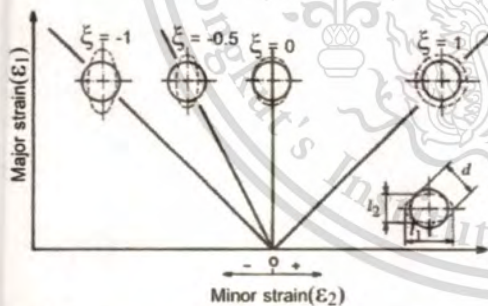


Fig. 2 Typical FLD for low-carbon sheet steel. (Muammer Koç, 2008)

Fig. 3 FLD with difference principle strain ratio

$$\varepsilon_1 = \ln \frac{l_1}{d} \quad \text{Eqs. (1)}$$

$$\varepsilon_2 = \ln \frac{l_2}{d} \quad \text{Eqs. (2)}$$

## 2.1 The empirical FLCs

The empirical FLC used in this paper is based on Keeler's model, which is implemented in DYNAFORM

m exponent of the yield function	6.0
n strain-hardening exponent	0.226
r <sub>0</sub> normal anisotropy	1.45
r <sub>45</sub> normal anisotropy	1.1
r <sub>90</sub> normal anisotropy	1.73

The critical major and minor strains are calculated by the FEA software using to above material properties and plotted to construct the forming limit curve (FLC), as show in Fig. 4.

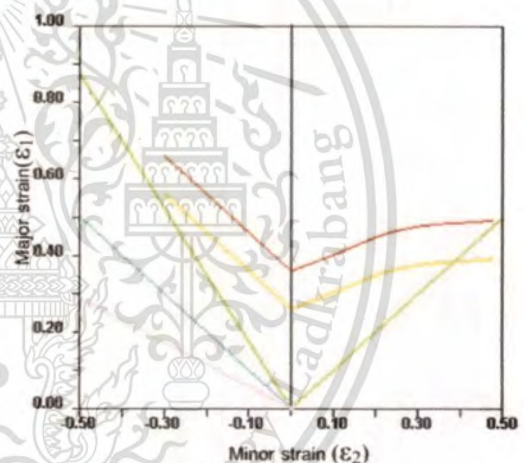


Fig. 4 FLD obtained by FEA Software

## 3 Design of FLC test die insert and testing parameters

### 3.1 test die insert and process parameter

Several researchers (Jieshi Chen, Xianbin Zhou and Jun Chen, 2009) have shown experimentally that non-linear strain path can change the shape and location of the FLC. Nevertheless, to on extent, this effect on the FLC can be minor of the non - linearity is kept small. In order to obtain a standardized assessment of the forming limit curve, the strain path at the apex of the bulged sample has to be control as linear

as possible (i.e., constant strain ratio). In this work, it was necessary to design proper testing die insert geometry – 1) die entry radius ( $r_d$ ) and 2) bulge length ( $L$ ), as show in Fig. 5.

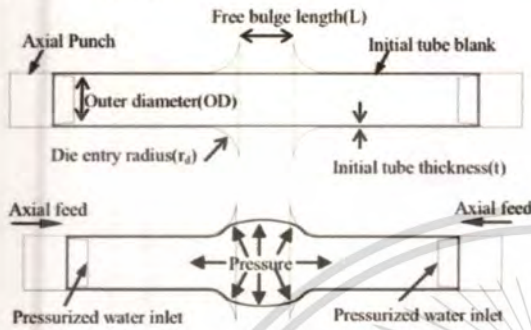


Fig.5 Schematic diagram of the test die insert parameter

It was found that only properly designed die insert geometry relative to tube sample geometry – 1) tube outer diameter (OD) and 2) tube sample thickness ( $t$ ) will allow the linear strain path during testing. A series of simulation were conducted with various die insert geometry and tube sample dimensions, see table 1, to determine the proper testing die insert geometry. Two geometry parameters were used to investigate, namely 1)  $L/OD$  and 2)  $r_d/t$ .

Table 1 Designed of Simulation running

Model	L/OD	rd/t	L	OD	rd	t	Results
RUN01	1	5	25.4	25.4	5	1	Non-linear
RUN02	1	15	25.4	25.4	15	1	Linear
RUN03	1	25	25.4	25.4	25	1	Non-linear
RUN04	2	5	50.8	25.4	5	1	Non-linear
RUN05	2	15	50.8	25.4	15	1	Non-linear
RUN06	2	25	50.8	25.4	25	1	Non-linear
RUN07	3	5	76.2	25.4	5	1	Non-linear
RUN08	3	15	76.2	25.4	15	1	Non-linear
RUN09	3	25	76.2	25.4	25	1	Non-linear

An FEA software (DYNAFORM) was used to conduct all the simulations in this work. Due to its symmetry, only one half of the testing

die inserts and tube sample were model, see Fig. 7. In each case of simulation run, several process parameters (i.e. fluid flux and axial feed distance) were tried in an attempt to form the sample with linear strain paths.



Fig. 7 Results of the formed simulation-Run02 show in half model

Four strain ratios ( $\xi = \epsilon_2/\epsilon_1$ ) -0.1, -0.2, -0.3 and -0.4 were the slopes of each strain path under investigation in this work. It no possible fluid flux and axial feed distance were found to fulfill the constant strain ratios then it was concluded that the specific die insert geometry is not proper. Table 1 summarizes the results of this simulation finding. Only die insert geometry in simulation RUN02 yields the satisfying linear strain path requirement (i.e. constant strain ratio  $\xi \pm 0.01$ ). Fig 8 compares strain paths at strain ratio -0.4 obtained from RUN01, 02 and 05. It can be seen that only RUN02 is able to keep the strain ratio of -0.4 constant (i.e. linear) all the way to the fracture limit, FLC.

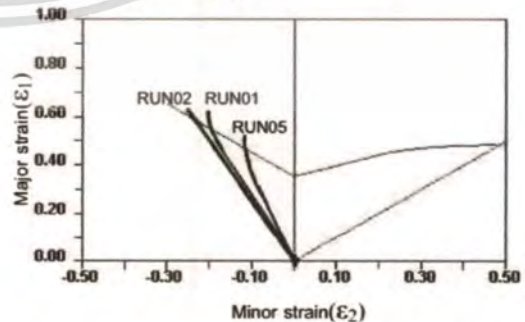


Fig. 8 Comparison between strain path of RUN02 and some another model then try to control strain path as  $\xi = -0.4$ .

The corresponding loading paths to the four strain paths to be used to control the fluid flux and the feeding distance in the forming limit experiments are shown in Fig. 9.

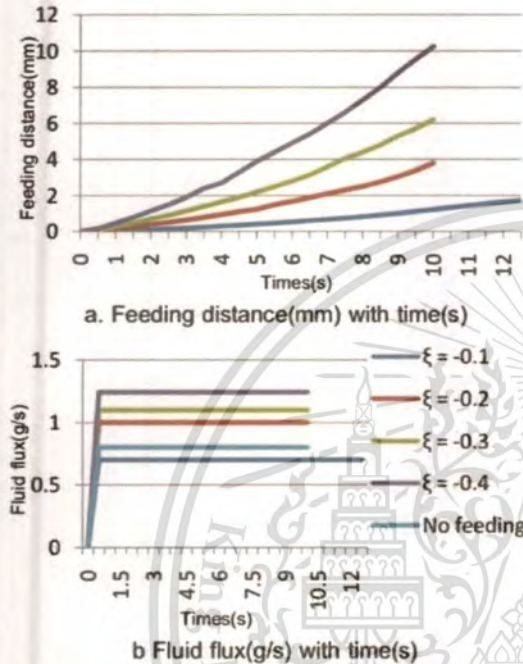


Fig. 9 Feeding distance and Fluid flux with times

The ratio of Model Run02 were put to test in another outer diameter and thickness of tube sample. It was found the tool geometry that can keep the strain ratio constant is not dependent on the thickness but dependent on only OD of the tube, as given in Eqs. (3)-(4).

$$L = OD \quad \text{Eqs. (3)}$$

$$r_d = \frac{15 \times OD}{25.4} \quad \text{Eqs. (4)}$$

### 3.2 FLC testing apparatus

The specimen tubes of tubular material low carbon steels commonly used in Thai industry, namely STKM with 1.2 mm thickness and 28.6 mm outer diameter. Circular grids with a diameter of 5mm are electrochemically etched on the tube surface before the experiments. A bulge test apparatus with a fixed bulge length without axial feeding as shown in Fig. 10 is used to implement

the forming limit experiments to obtain the strain path on right side of the FLD. The specimen 280mm initial tube length are expanded at both the end of the tube by swaging process and fix by punch during forming.

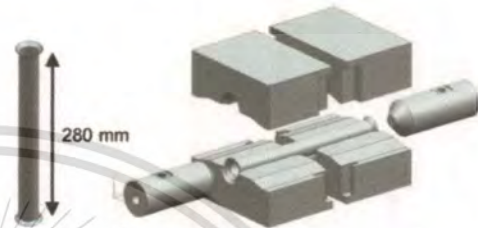


Fig. 10 The experimental apparatus for bulge tests without axial feeding.

A hydroforming test machine with axial feeding is used to conduct the experiments to obtain the strain path on the left side of the FLD, in which tensile and compressive strains occur as shown in Fig. 11.



Fig. 11 The experimental apparatus for bulge tests with axial feeding.



Fig. 12 Schematic diagram of the experimental apparatus for bulge tests

#### The testing procedure

- Cutting of tubular blanks to approximate size.
- Filler pieces, rounding off of any sharp edges in the tubular blanks.
- Swaging at the both end of tube in order to fix by punch during forming. (for bulge tests without axial feeding.)
- Circular grids were electro chemically etched onto the surface of tube samples.
- The surface of the tool is lubricated.
- Running bulge tests
- After bulge tests, Dimensions of the grid circles at the pole were accurately measured to obtain engineering major and minor strains.
- The critical major and minor strains are plotted to construct the forming limit curve (FLC) for tubular material.

#### 4 Sensitivity study on effect of process parameters

A real automotive part, i.e. a fuel filler pipe (see Fig. 13), was considered in this study to design proper process parameters. FLC of comparable steel sheet available in DYNAFORM was used to conduct all the simulation runs. A typical process loading profile (i.e. internal pressure versus axial feed distance) for this part was found through several simulation runs, Fig. 14. It was concluded that this particular part was prone to fracture due to the effect of loading profile during "Forming 2" period. Therefore, five move simulations were carried out to investigate various loading profiles, see Fig. 14.

Fig. 15 shows some snapshot from the tube hydroforming simulation using loading profile 3(220 bar). It can be seen that the part can be hydroformed successfully without any fracture because the part is formed under the forming limit curve (FLC) at all of the forming steps. For this

particular part, when the pressure level during the "forming 2" period is decreased below 225 bar. This is evident by comparing FLD from loading profile 1 to that from loading profile 5, Fig. 16. This information will help reduce the time spent during real part tryout.



Fig. 13 A fuel filler pipe geometry.

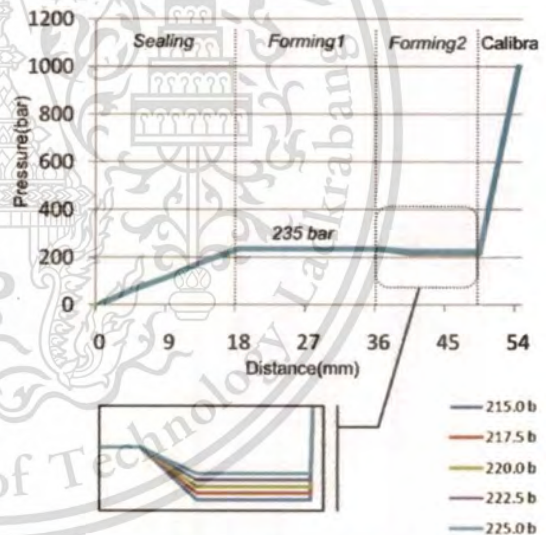


Fig. 14 Feeding distance(mm) and Fluid flux(g/s) with time(s)

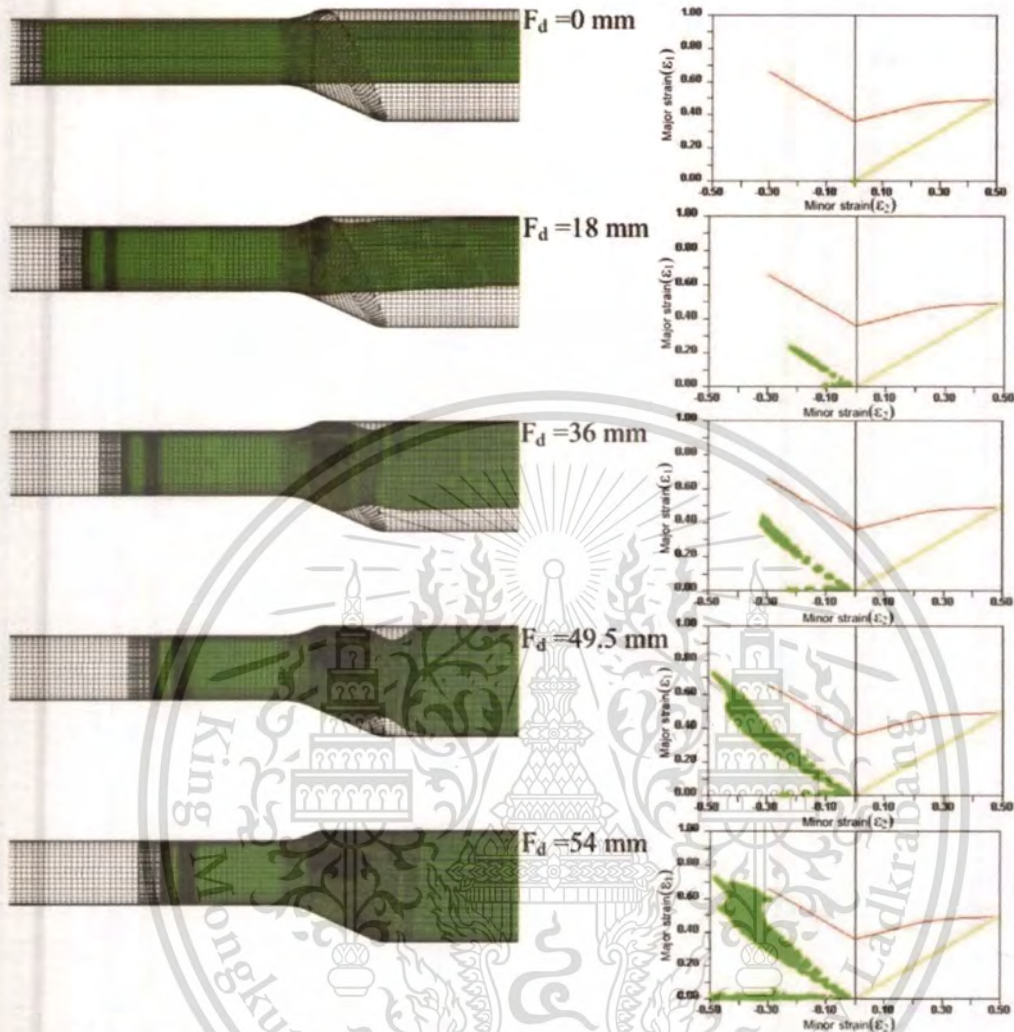


Fig. 15 Intermediate forming steps and their corresponding Forming Limit Diagram (FLD)

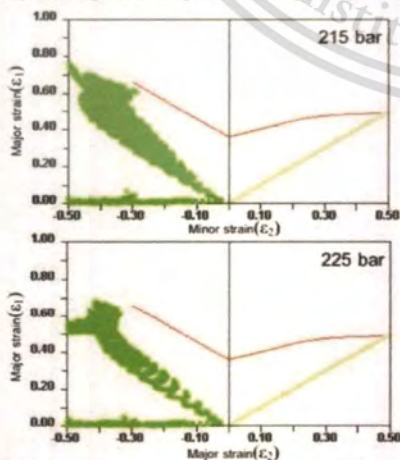


Fig. 16 Comparison of FLD when the pressure level during the "forming 2" is 215 and 225 bar.

## 5 Conclusions

In this case, FEA was used to investigate and determine proper FLC testing die insert geometry, i.e. die entry radius and bulge length, in relation to tube sample geometry, i.e. outer diameter and tube thickness. It was found that the proper die geometry does not depend on sample thickness but only on outside diameter of the sample. A FLC testing apparatus has been designed for commonly used STKM 11A tubing in Thailand. Testing process parameter (loading profiles) were also determined for conducting the test that guarantees linear strain paths in the

deforming samples. This knowledge can be applied to design proper FLC testing die inserts for other tubing dimensions. Forming limit curves to be generated using this testing apparatus will be of great usefulness for Thai industry in designing and producing high strength-to-weight ratioed parts using tube hydroforming technology.

#### **Acknowledgements**

The authors would like to extend their thanks to National Science and Technology Development Agency, King Mongkut's Institute of Technology Ladkrabang, Tokyo Institute of Technology and wish to thank Dr. Suwat Jirathearnat, Assoc.Prof. Naoto Ohtake and Dr. Monsak Pimsarn for their kind help at various stages of the work.

#### **References**

- [1] Hwang, Y.M., Lin, T.C., Chang, W.C., 2009. Forming limit diagrams of tubular materials by bulge tests
- [2] Nefussi, G., Combescure, A., 2002. Coupled buckling and plastic instability for tube hydroforming.
- [3] Korkolis, Y.P., Kyriakides, S., 2008. Inflation and burst of anisotropic aluminum tubes for hydroforming applications.
- [4] Xing, H.L., Makinouchi, A., 2001. Numerical analysis and design for tubular hydroforming.
- [5] Jieshi Chena, Xianbin Zhoub, Jun Chena, 2009. Sheet metal forming limit prediction based on plastic deformation energy.
- [6] E. Chu, Yu Xu, 2008. Influences of generalized loading parameters on FLD predictions for aluminum tube hydroforming.
- [7] M. Koc. Hydroforming for Advanced Manufacturing.
- [8] Chan T. Technology of sheet metal forming.

This material is reserved for educational use only, not allowed for commercial use.

Forbidden to modify the content, and cite the document when use.

## APPENDIX B

### DATA ANALYSIS

#### Curve Correction

$$l_1 = 2r_{\theta P} \sin^{-1} \left( \frac{l_1'}{2r_{\theta P}} \right)$$

$$l_2 = 2r_{\varphi P} \sin^{-1} \left( \frac{l_2'}{2r_{\varphi P}} \right)$$

Where  $l_1$  = Major deformation

$l_2$  = Minor deformation

$l_1'$  = Captured major deformation

$l_2'$  = Captured minor deformation

$r_{\varphi P}$  = Meridian radius of curvature at the pole

$r_{\theta P}$  = Circumferential radius of curvature at the pole

Strain

$$\varepsilon_1 = \ln \frac{l_1}{d}$$

$$\varepsilon_2 = \ln \frac{l_2}{d}$$

Where  $\varepsilon_1$  = Major strain

$\varepsilon_2$  = Minor strain

$d$  = Initial grid length

## Set1

No.	$r_{\theta P}$	$r_{\varphi P}$	Position	L1'	L2'	L	L1	L2	$\varepsilon_1$	$\varepsilon_2$	$\xi$
1	18.43	95.22	-47.5	3.573	2.653	2.72	3.5786	2.6531	0.2743	-0.0249	-0.0908
			-35	3.6	2.64	2.72	3.6057	2.6401	0.2819	-0.0298	-0.1058
			-22.5	3.72	2.64	2.72	3.7263	2.6401	0.3148	-0.0298	-0.0947
			-10	3.427	2.65	2.72	3.4320	2.6501	0.2325	-0.0260	-0.1120
			2.5	3.42	2.65	2.72	3.4249	2.6501	0.2304	-0.0260	-0.1130
			15	3.627	2.66	2.72	3.6329	2.6601	0.2894	-0.0223	-0.0770
			30	3.933	2.64	2.72	3.9405	2.6401	0.3707	-0.0298	-0.0805
			42.5	3.653	2.65	2.72	3.6590	2.6501	0.2966	-0.0260	-0.0878
2	17.75	111.87	-37.5	3.587	2.66	2.72	3.5931	2.6601	0.2784	-0.0223	-0.0800
			-25	3.601	2.66	2.72	3.6072	2.6601	0.2823	-0.0223	-0.0789
			-12.5	3.533	2.668	2.72	3.5389	2.6681	0.2632	-0.0193	-0.0733
			0	3.294	2.67	2.72	3.2987	2.6701	0.1929	-0.0185	-0.0961
			15	3.467	2.673	2.72	3.4725	2.6731	0.2443	-0.0174	-0.0713
			27.5	3.68	2.658	2.72	3.6866	2.6581	0.3041	-0.0230	-0.0758
			40	3.76	2.66	2.72	3.7671	2.6601	0.3257	-0.0223	-0.0684
3	16.35	260.11	-40	3.307	2.68	2.72	3.3127	2.6800	0.1971	-0.0148	-0.0751
			-27.5	3.2	2.68	2.72	3.2051	2.6800	0.1641	-0.0148	-0.0902
			-15	3.32	2.667	2.72	3.3257	2.6670	0.2011	-0.0197	-0.0978
			-2.5	2.973	2.68	2.72	2.9771	2.6800	0.0903	-0.0148	-0.1640
			10	3.281	2.665	2.72	3.2865	2.6650	0.1892	-0.0204	-0.1079
			22.5	3.254	2.667	2.72	3.2594	2.6670	0.1809	-0.0197	-0.1087
			35	3.173	2.67	2.72	3.1780	2.6700	0.1556	-0.0185	-0.1192
			45	3.267	2.665	2.72	3.2725	2.6650	0.1849	-0.0204	-0.1105
4	15.38	863.13	-37.5	3.053	2.69	2.72	3.0580	2.6900	0.1171	-0.0111	-0.0947
			-25	3.055	2.693	2.72	3.0600	2.6930	0.1178	-0.0100	-0.0847
			-12.5	3.08	2.7	2.72	3.0852	2.7000	0.1260	-0.0074	-0.0586
			0	2.872	2.7	2.72	2.8762	2.7000	0.0558	-0.0074	-0.1322
			12.5	3.08	2.7	2.72	3.0852	2.7000	0.1260	-0.0074	-0.0586
			25	3.067	2.694	2.72	3.0721	2.6940	0.1217	-0.0096	-0.0789
			37.5	3.04	2.7	2.72	3.0450	2.7000	0.1129	-0.0074	-0.0654
5	15.16	1456.14	-37.5	3.053	2.701	2.72	3.0582	2.7010	0.1172	-0.0070	-0.0598
			-25	3.008	2.701	2.72	3.0130	2.7010	0.1023	-0.0070	-0.0685
			-12.5	3	2.704	2.72	3.0049	2.7040	0.0996	-0.0059	-0.0592
			0	2.84	2.712	2.72	2.8442	2.7120	0.0446	-0.0029	-0.0660
			12.5	2.933	2.703	2.72	2.9376	2.7030	0.0770	-0.0063	-0.0815
			25	2.987	2.701	2.72	2.9919	2.7010	0.0953	-0.0070	-0.0736
			35	2.977	2.707	2.72	2.9818	2.7070	0.0919	-0.0048	-0.0521

## Set2

No.	$r_{\theta P}$	$r_{\varphi P}$	Position	L1'	L2'	L	L1	L2	$\varepsilon_1$	$\varepsilon_2$	$\xi$
1	20.28	54.67	-45	3.908	2.5	2.72	3.9141	2.5002	0.3639	-0.0843	-0.2315
			-35	3.6	2.64	2.72	3.6057	2.6401	0.2819	-0.0298	-0.1058
			-22.5	3.72	2.64	2.72	3.7263	2.6401	0.3148	-0.0298	-0.0947
			-10	3.427	2.65	2.72	3.4320	2.6501	0.2325	-0.0260	-0.1120
			2.5	3.42	2.65	2.72	3.4249	2.6501	0.2304	-0.0260	-0.1130
			15	3.627	2.66	2.72	3.6329	2.6601	0.2894	-0.0223	-0.0770
			30	3.933	2.64	2.72	3.9405	2.6401	0.3707	-0.0298	-0.0805
2	17.75	111.87	42.5	3.653	2.65	2.72	3.6590	2.6501	0.2966	-0.0260	-0.0878
			-37.5	3.587	2.66	2.72	3.5931	2.6601	0.2784	-0.0223	-0.0800
			-25	3.601	2.66	2.72	3.6072	2.6601	0.2823	-0.0223	-0.0789
			-12.5	3.533	2.668	2.72	3.5389	2.6681	0.2632	-0.0193	-0.0733
			0	3.294	2.67	2.72	3.2987	2.6701	0.1929	-0.0185	-0.0961
			15	3.467	2.673	2.72	3.4725	2.6731	0.2443	-0.0174	-0.0713
			27.5	3.68	2.658	2.72	3.6866	2.6581	0.3041	-0.0230	-0.0758
3	16.35	260.11	40	3.76	2.66	2.72	3.7671	2.6601	0.3257	-0.0223	-0.0684
			-40	3.307	2.68	2.72	3.3127	2.6800	0.1971	-0.0148	-0.0751
			-27.5	3.2	2.68	2.72	3.2051	2.6800	0.1641	-0.0148	-0.0902
			-15	3.32	2.667	2.72	3.3257	2.6670	0.2011	-0.0197	-0.0978
			-2.5	2.973	2.68	2.72	2.9771	2.6800	0.0903	-0.0148	-0.1640
			10	3.281	2.665	2.72	3.2865	2.6650	0.1892	-0.0204	-0.1079
			22.5	3.254	2.667	2.72	3.2594	2.6670	0.1809	-0.0197	-0.1087
4	15.38	863.13	35	3.173	2.67	2.72	3.1780	2.6700	0.1556	-0.0185	-0.1192
			45	3.267	2.665	2.72	3.2725	2.6650	0.1849	-0.0204	-0.1105
			-37.5	3.053	2.69	2.72	3.0580	2.6900	0.1171	-0.0111	-0.0947
			-25	3.055	2.693	2.72	3.0600	2.6930	0.1178	-0.0100	-0.0847
			-12.5	3.08	2.7	2.72	3.0852	2.7000	0.1260	-0.0074	-0.0586
			0	2.872	2.7	2.72	2.8762	2.7000	0.0558	-0.0074	-0.1322
			12.5	3.08	2.7	2.72	3.0852	2.7000	0.1260	-0.0074	-0.0586
5	15.16	1456.14	25	3.067	2.694	2.72	3.0721	2.6940	0.1217	-0.0096	-0.0789
			37.5	3.04	2.7	2.72	3.0450	2.7000	0.1129	-0.0074	-0.0654
			-37.5	3.053	2.701	2.72	3.0582	2.7010	0.1172	-0.0070	-0.0598
			-25	3.008	2.701	2.72	3.0130	2.7010	0.1023	-0.0070	-0.0685
			-12.5	3	2.704	2.72	3.0049	2.7040	0.0996	-0.0059	-0.0592
			0	2.84	2.712	2.72	2.8442	2.7120	0.0446	-0.0029	-0.0660
			12.5	2.933	2.703	2.72	2.9376	2.7030	0.0770	-0.0063	-0.0815
			25	2.987	2.701	2.72	2.9919	2.7010	0.0953	-0.0070	-0.0736
			35	2.977	2.707	2.72	2.9818	2.7070	0.0919	-0.0048	-0.0521

## Set2 (Cont.)

No.	$\tau_{\theta P}$	$\tau_{\varphi P}$	Position	L1'	L2'	L	L1	L2	$\varepsilon_1$	$\varepsilon_2$	$\xi$
6	16.04	514.78	-40	3.173	2.652	2.72	3.1782	2.6520	0.1557	-0.0253	-0.1626
			-25	3.2	2.654	2.72	3.2053	2.6540	0.1642	-0.0246	-0.1496
			-15	3.107	2.657	2.72	3.1119	2.6570	0.1346	-0.0234	-0.1741
			0	3.067	2.659	2.72	3.0717	2.6590	0.1216	-0.0227	-0.1865
			15	3.093	2.657	2.72	3.0978	2.6570	0.1301	-0.0234	-0.1802
			25	3.227	2.657	2.72	3.2325	2.6570	0.1726	-0.0234	-0.1358
			40	3.16	2.653	2.72	3.1651	2.6530	0.1516	-0.0249	-0.1646

## Set3

No.	$\tau_{\theta P}$	$\tau_{\varphi P}$	Position	L1'	L2'	L	L1	L2	$\varepsilon_1$	$\varepsilon_2$	$\xi$
1	21.62	51.39	-45.0	4.51	2.36	2.72	4.5152	2.3632	0.5068	-0.1406	-0.2774
			-32.5	4.61	2.34	2.72	4.6228	2.3402	0.5304	-0.1504	-0.2836
			-20.0	4.72	2.32	2.72	4.7294	2.3152	0.5532	-0.1611	-0.2913
			-7.5	3.93	2.35	2.72	3.9384	2.3502	0.3702	-0.1461	-0.3948
			5.0	3.97	2.35	2.72	3.9786	2.3542	0.3803	-0.1444	-0.3798
			17.5	4.16	2.36	2.72	4.1664	2.3612	0.4264	-0.1415	-0.3317
			30.0	4.80	2.32	2.72	4.8099	2.3202	0.5700	-0.1590	-0.2789
			42.5	4.44	2.36	2.72	4.4478	2.3602	0.4918	-0.1419	-0.2885
2	19.10	86.17	-37.5	3.88	2.44	2.72	3.8867	2.4431	0.3569	-0.1074	-0.3008
			-25.0	3.87	2.45	2.72	3.8726	2.4541	0.3533	-0.1029	-0.2912
			-12.5	3.80	2.46	2.72	3.8063	2.4571	0.3360	-0.1017	-0.3025
			2.5	3.63	2.46	2.72	3.6325	2.4641	0.2893	-0.0988	-0.3416
			15.0	3.67	2.47	2.72	3.6727	2.4671	0.3003	-0.0976	-0.3250
			30.0	3.90	2.47	2.72	3.9018	2.4671	0.3608	-0.0976	-0.2705
			42.5	3.89	2.43	2.72	3.8998	2.4301	0.3603	-0.1127	-0.3128
3	19.08	83.61	-37.5	3.83	2.43	2.72	3.8334	2.4341	0.3431	-0.1111	-0.3237
			-25.0	3.88	2.44	2.72	3.8877	2.4371	0.3572	-0.1098	-0.3075
			-12.5	3.55	2.45	2.72	3.5521	2.4531	0.2669	-0.1033	-0.3870
			0.0	3.51	2.47	2.72	3.5120	2.4671	0.2555	-0.0976	-0.3819
			12.5	3.77	2.45	2.72	3.7792	2.4541	0.3289	-0.1029	-0.3128
			25.0	3.90	2.43	2.72	3.9028	2.4331	0.3611	-0.1115	-0.3087
			37.5	3.80	2.43	2.72	3.8063	2.4331	0.3360	-0.1115	-0.3317
4	18.15	150.59	-40.0	3.72	2.44	2.72	3.7265	2.4400	0.3148	-0.1086	-0.3450
			-27.5	3.72	2.45	2.72	3.7265	2.4540	0.3148	-0.1029	-0.3268
			-15.0	3.40	2.45	2.72	3.4050	2.4540	0.2246	-0.1029	-0.4581
			-2.5	3.36	2.47	2.72	3.3648	2.4700	0.2127	-0.0964	-0.4531
			10.0	3.52	2.46	2.72	3.5255	2.4570	0.2594	-0.1017	-0.3920
			22.5	3.64	2.43	2.72	3.6461	2.4340	0.2930	-0.1111	-0.3791
			35.0	3.71	2.43	2.72	3.7145	2.4270	0.3116	-0.1140	-0.3657

## Set3 (Cont.)

No.	$r_{\theta P}$	$r_{\phi P}$	Position	L1'	L2'	L	L1	L2	$\epsilon_1$	$\epsilon_2$	$\xi$
5	18.69	105.41	-45.0	3.69	2.48	2.72	3.6990	2.4801	0.3074	-0.0924	-0.3004
			-32.5	3.72	2.49	2.72	3.7262	2.4901	0.3147	-0.0883	-0.2806
			-20.0	3.67	2.51	2.72	3.6729	2.5101	0.3004	-0.0803	-0.2674
			-7.5	3.41	2.51	2.72	3.4178	2.5051	0.2284	-0.0823	-0.3605
			7.5	3.47	2.51	2.72	3.4720	2.5071	0.2441	-0.0815	-0.3340
			20.0	3.80	2.50	2.72	3.8066	2.4951	0.3361	-0.0863	-0.2568
			32.5	3.73	2.50	2.72	3.7392	2.5001	0.3182	-0.0843	-0.2649
			45.0	3.78	2.50	2.72	3.7814	2.5001	0.3295	-0.0843	-0.2559
6	17.33	765.80	-40.0	3.43	2.52	2.72	3.4326	2.5230	0.2327	-0.0752	-0.3231
			-27.5	3.43	2.55	2.72	3.4326	2.5470	0.2327	-0.0657	-0.2824
			-15.0	3.33	2.55	2.72	3.3392	2.5490	0.2051	-0.0649	-0.3166
			0.0	3.36	2.55	2.72	3.3653	2.5530	0.2129	-0.0634	-0.2976
			12.5	3.41	2.53	2.72	3.4185	2.5270	0.2286	-0.0736	-0.3220
			27.5	3.43	2.52	2.72	3.4326	2.5230	0.2327	-0.0752	-0.3231
			40.0	3.41	2.53	2.72	3.4185	2.5270	0.2286	-0.0736	-0.3220
			7	17.21	314.92	-45.0	3.36	2.54	2.72	3.3654	2.5370
-32.5	3.40	2.53				2.72	3.4056	2.5300	0.2248	-0.0724	-0.3221
-20.0	3.40	2.54				2.72	3.4056	2.5350	0.2248	-0.0704	-0.3134
-7.5	3.25	2.55				2.72	3.2579	2.5530	0.1804	-0.0634	-0.3511
7.5	3.35	2.55				2.72	3.3523	2.5500	0.2090	-0.0645	-0.3088
20.0	3.43	2.54				2.72	3.4327	2.5370	0.2327	-0.0696	-0.2993
32.5	3.37	2.54				2.72	3.3794	2.5350	0.2171	-0.0704	-0.3245
45.0	3.39	2.53				2.72	3.3925	2.5340	0.2209	-0.0708	-0.3206
8	16.08	598.16	-40.0	3.15	2.60	2.72	3.1520	2.6020	0.1474	-0.0444	-0.3008
			-25.0	3.16	2.61	2.72	3.1651	2.6100	0.1516	-0.0413	-0.2724
			12.5	3.05	2.60	2.72	3.0586	2.6000	0.1173	-0.0451	-0.3846
			0.0	3.00	2.62	2.72	3.0044	2.6200	0.0994	-0.0375	-0.3767
			12.5	3.09	2.61	2.72	3.0978	2.6130	0.1301	-0.0401	-0.3086
			25.0	3.13	2.60	2.72	3.1380	2.6000	0.1429	-0.0451	-0.3156
			40.0	3.12	2.60	2.72	3.1249	2.5970	0.1388	-0.0463	-0.3334
			9	16.04	927.01	-45.0	3.15	2.61	2.72	3.1521	2.6140
-32.5	3.16	2.61				2.72	3.1651	2.6130	0.1516	-0.0401	-0.2648
-20.0	3.16	2.62				2.72	3.1651	2.6150	0.1516	-0.0394	-0.2597
-7.5	2.99	2.62				2.72	2.9913	2.6170	0.0951	-0.0386	-0.4060
7.5	3.09	2.61				2.72	3.0978	2.6070	0.1301	-0.0424	-0.3262
20.0	3.21	2.62				2.72	3.2184	2.6170	0.1683	-0.0386	-0.2294
32.5	3.13	2.62				2.72	3.1380	2.6170	0.1430	-0.0386	-0.2700
45.0	3.15	2.61				2.72	3.1521	2.6140	0.1474	-0.0397	-0.2696

## Set4

No.	$r_{\theta P}$	$r_{\phi P}$	Position	L1'	L2'	L	L1	L2	$\epsilon_1$	$\epsilon_2$	$\xi$
1	23.71	38.50	-45.0	4.84	2.23	2.72	4.8484	2.2303	0.5780	-0.1985	-0.3434
			-32.5	5.19	2.16	2.72	5.1974	2.1603	0.6475	-0.2304	-0.3558
			-20.0	5.23	2.15	2.72	5.2366	2.1543	0.6550	-0.2332	-0.3560
			-7.5	4.33	2.20	2.72	4.3401	2.1973	0.4673	-0.2134	-0.4567
			7.5	4.00	2.20	2.72	4.0048	2.2023	0.3869	-0.2111	-0.5458
			20.0	4.69	2.15	2.72	4.7007	2.1543	0.5471	-0.2332	-0.4262
			32.5	5.73	2.11	2.72	5.7471	2.1083	0.7481	-0.2548	-0.3406
2	21.15	81.54	-45.0	4.20	2.31	2.72	4.2069	2.3081	0.4361	-0.1642	-0.3766
			-32.5	4.25	2.33	2.72	4.2612	2.3331	0.4489	-0.1534	-0.3418
			-20.0	4.19	2.35	2.72	4.1939	2.3481	0.4330	-0.1470	-0.3396
			-7.5	3.84	2.32	2.72	3.8453	2.3231	0.3462	-0.1577	-0.4556
			7.5	3.87	2.37	2.72	3.8734	2.3671	0.3535	-0.1390	-0.3931
			20.0	4.20	2.31	2.72	4.2069	2.3071	0.4361	-0.1647	-0.3776
			32.5	4.36	2.31	2.72	4.3708	2.3101	0.4743	-0.1634	-0.3444
3	19.01	298.44	-45.0	3.76	2.41	2.72	3.7682	2.4070	0.3260	-0.1222	-0.3750
			-32.5	3.71	2.41	2.72	3.7129	2.4080	0.3112	-0.1218	-0.3915
			-20.0	3.80	2.42	2.72	3.8064	2.4230	0.3360	-0.1156	-0.3441
			-7.5	3.35	2.42	2.72	3.3513	2.4230	0.2087	-0.1156	-0.5539
			7.5	3.51	2.43	2.72	3.5120	2.4270	0.2556	-0.1140	-0.4460
			20.0	3.68	2.42	2.72	3.6858	2.4200	0.3038	-0.1169	-0.3846
			32.5	3.71	2.41	2.72	3.7129	2.4070	0.3112	-0.1222	-0.3929
4	18.88	68.16	-45.0	3.73	2.39	2.72	3.7391	2.3911	0.3182	-0.1289	-0.4050
			-32.5	3.63	2.42	2.72	3.6336	2.4201	0.2896	-0.1168	-0.4034
			-20.0	3.69	2.39	2.72	3.6989	2.3891	0.3074	-0.1297	-0.4219
			-7.5	3.45	2.41	2.72	3.4578	2.4101	0.2400	-0.1210	-0.5040
			7.5	3.40	2.42	2.72	3.4046	2.4201	0.2245	-0.1168	-0.5203
			20.0	3.51	2.41	2.72	3.5121	2.4071	0.2556	-0.1222	-0.4781
			32.5	3.60	2.39	2.72	3.6055	2.3901	0.2818	-0.1293	-0.4588
5	18.89	234.50	-45.0	3.80	2.42	2.72	3.8064	2.4200	0.3361	-0.1169	-0.3477
			-32.5	3.65	2.42	2.72	3.6597	2.4200	0.2968	-0.1169	-0.3938
			-20.0	3.75	2.44	2.72	3.7532	2.4350	0.3220	-0.1107	-0.3438
			-7.5	3.59	2.45	2.72	3.5924	2.4450	0.2782	-0.1066	-0.3831
			7.5	3.52	2.44	2.72	3.5251	2.4370	0.2593	-0.1099	-0.4237
			20.0	3.76	2.42	2.72	3.7672	2.4240	0.3257	-0.1152	-0.3537
			32.5	3.75	2.43	2.72	3.7532	2.4250	0.3220	-0.1148	-0.3565
			45.0	3.76	2.42	2.72	3.7662	2.4210	0.3254	-0.1164	-0.3578

## Set4(Cont.)

No.	$r_{\theta P}$	$r_{\phi P}$	Position	L1'	L2'	L	L1	L2	$\epsilon_1$	$\epsilon_2$	$\xi$
6	18.44	191.23	-45.0	3.72	2.45	2.72	3.7273	2.4510	0.3151	-0.1041	-0.3305
			-32.5	3.67	2.45	2.72	3.6731	2.4500	0.3004	-0.1045	-0.3480
			-20.0	3.73	2.45	2.72	3.7394	2.4540	0.3183	-0.1029	-0.3233
			-7.5	3.41	2.46	2.72	3.4189	2.4591	0.2287	-0.1008	-0.4409
			7.5	3.47	2.46	2.72	3.4721	2.4570	0.2441	-0.1017	-0.4165
			20.0	3.71	2.45	2.72	3.7153	2.4540	0.3118	-0.1029	-0.3300
			32.5	3.79	2.45	2.72	3.7947	2.4520	0.3330	-0.1037	-0.3115
7	17.65	511.24	-45.0	3.47	2.47	2.72	3.4726	2.4690	0.2443	-0.0968	-0.3964
			-32.5	3.44	2.47	2.72	3.4455	2.4690	0.2364	-0.0968	-0.4095
			-20.0	3.40	2.47	2.72	3.4053	2.4740	0.2247	-0.0948	-0.4219
			-7.5	3.33	2.47	2.72	3.3380	2.4740	0.2047	-0.0948	-0.4630
			7.5	3.29	2.47	2.72	3.2978	2.4740	0.1926	-0.0948	-0.4921
			20.0	3.43	2.47	2.72	3.4324	2.4670	0.2326	-0.0976	-0.4197
			32.5	3.48	2.46	2.72	3.4857	2.4610	0.2480	-0.1001	-0.4034
8	16.70	371.98	-45.0	3.32	2.52	2.72	3.3255	2.5240	0.2010	-0.0748	-0.3721
			-20.0	3.28	2.52	2.72	3.2853	2.5210	0.1888	-0.0760	-0.4024
			-12.5	3.19	2.54	2.72	3.1919	2.5400	0.1600	-0.0685	-0.4280
			0.0	3.15	2.56	2.72	3.1517	2.5600	0.1473	-0.0606	-0.4116
			12.5	3.24	2.56	2.72	3.2451	2.5600	0.1765	-0.0606	-0.3434
			20.0	3.36	2.52	2.72	3.3657	2.5220	0.2130	-0.0756	-0.3548
			37.5	3.36	2.53	2.72	3.3667	2.5280	0.2133	-0.0732	-0.3432
9	16.16	392.31	-45.0	3.20	2.58	2.72	3.2063	2.5800	0.1645	-0.0528	-0.3213
			-32.5	3.19	2.57	2.72	3.1922	2.5720	0.1601	-0.0559	-0.3495
			-20.0	3.19	2.60	2.72	3.1922	2.6000	0.1601	-0.0451	-0.2819
			-7.5	3.08	2.59	2.72	3.0847	2.5940	0.1258	-0.0474	-0.3770
			7.5	3.03	2.59	2.72	3.0314	2.5930	0.1084	-0.0478	-0.4411
			20.0	3.16	2.60	2.72	3.1651	2.6000	0.1515	-0.0451	-0.2977
			32.5	3.20	2.60	2.72	3.2053	2.6030	0.1642	-0.0440	-0.2678
			45.0	3.16	2.60	2.72	3.1651	2.6040	0.1515	-0.0436	-0.2876

## Set5

No.	$r_{\theta P}$	$r_{\phi P}$	Position	L1'	L2'	L	L1	L2	$\epsilon_1$	$\epsilon_2$	$\xi$	
1	17.30	86.01	-37.5	3.73	2.85	2.72	3.7413	2.8501	0.3188	0.0467	0.1466	
			-25.0	4.03	2.85	2.72	4.0361	2.8501	0.3947	0.0467	0.1184	
			-12.5	3.54	2.85	2.72	3.5462	2.8501	0.2652	0.0467	0.1762	
			0.0	3.30	2.82	2.72	3.3050	2.8211	0.1948	0.0365	0.1874	
			12.5	3.69	2.85	2.72	3.7000	2.8541	0.3077	0.0481	0.1564	
			25.0			2.72						
			37.5	3.71	2.84	2.72	3.7141	2.8401	0.3115	0.0432	0.1387	
2	17.30	86.22	-37.5	3.73	2.81	2.72	3.7403	2.8081	0.3185	0.0319	0.1001	
			-25.0	4.05	2.83	2.72	4.0623	2.8271	0.4011	0.0386	0.0963	
			-12.5	3.49	2.83	2.72	3.5000	2.8271	0.2521	0.0386	0.1532	
			0.0	3.38	2.82	2.72	3.3854	2.8201	0.2188	0.0361	0.1652	
			12.5	3.51	2.84	2.72	3.5130	2.8401	0.2558	0.0432	0.1689	
			25.0			2.72						
			37.5	3.76	2.82	2.72	3.7674	2.8211	0.3258	0.0365	0.1121	
3	18.53	86.23	-37.5	3.81	2.88	2.72	3.8198	2.8751	0.3396	0.0555	0.1634	
			-25.0			2.72						
			-12.5	3.59	2.87	2.72	3.5926	2.8701	0.2783	0.0537	0.1931	
			0.0	3.32	2.83	2.72	3.3245	2.8261	0.2007	0.0383	0.1907	
			12.5	3.45	2.84	2.72	3.4590	2.8401	0.2404	0.0432	0.1798	
			25.0	4.07	2.86	2.72	4.0752	2.8571	0.4043	0.0492	0.1217	
			37.5	3.84	2.87	2.72	3.8479	2.8681	0.3469	0.0530	0.1529	
4	16.36	259.39	-37.5	3.33	2.80	2.72	3.3388	2.8000	0.2050	0.0290	0.1414	
			-25.0	3.39	2.80	2.72	3.3931	2.8000	0.2211	0.0290	0.1311	
			-12.5	3.29	2.80	2.72	3.2986	2.8000	0.1929	0.0290	0.1503	
			0.0			2.72						
			12.5	3.25	2.80	2.72	3.2584	2.8000	0.1806	0.0290	0.1605	
			25.0	3.27	2.81	2.72	3.2725	2.8130	0.1849	0.0336	0.1818	
			37.5	3.27	2.80	2.72	3.2725	2.8000	0.1849	0.0290	0.1568	
5	15.80	863.30	-37.5	2.99	2.73	2.72	2.9915	2.7330	0.0951	0.0048	0.0501	
			-25.0	3.05	2.74	2.72	3.0578	2.7370	0.1171	0.0062	0.0532	
			-12.5	2.84	2.71	2.72	2.8438	2.7070	0.0445	-0.0048	-0.1076	
			0.0	2.80	2.71	2.72	2.8037	2.7070	0.0303	-0.0048	-0.1581	
			12.5	2.93	2.72	2.72	2.9312	2.7170	0.0748	-0.0011	-0.0148	
			25.0	3.15	2.76	2.72	3.1522	2.7570	0.1475	0.0135	0.0916	
			37.5	3.09	2.76	2.72	3.0980	2.7630	0.1301	0.0157	0.1206	

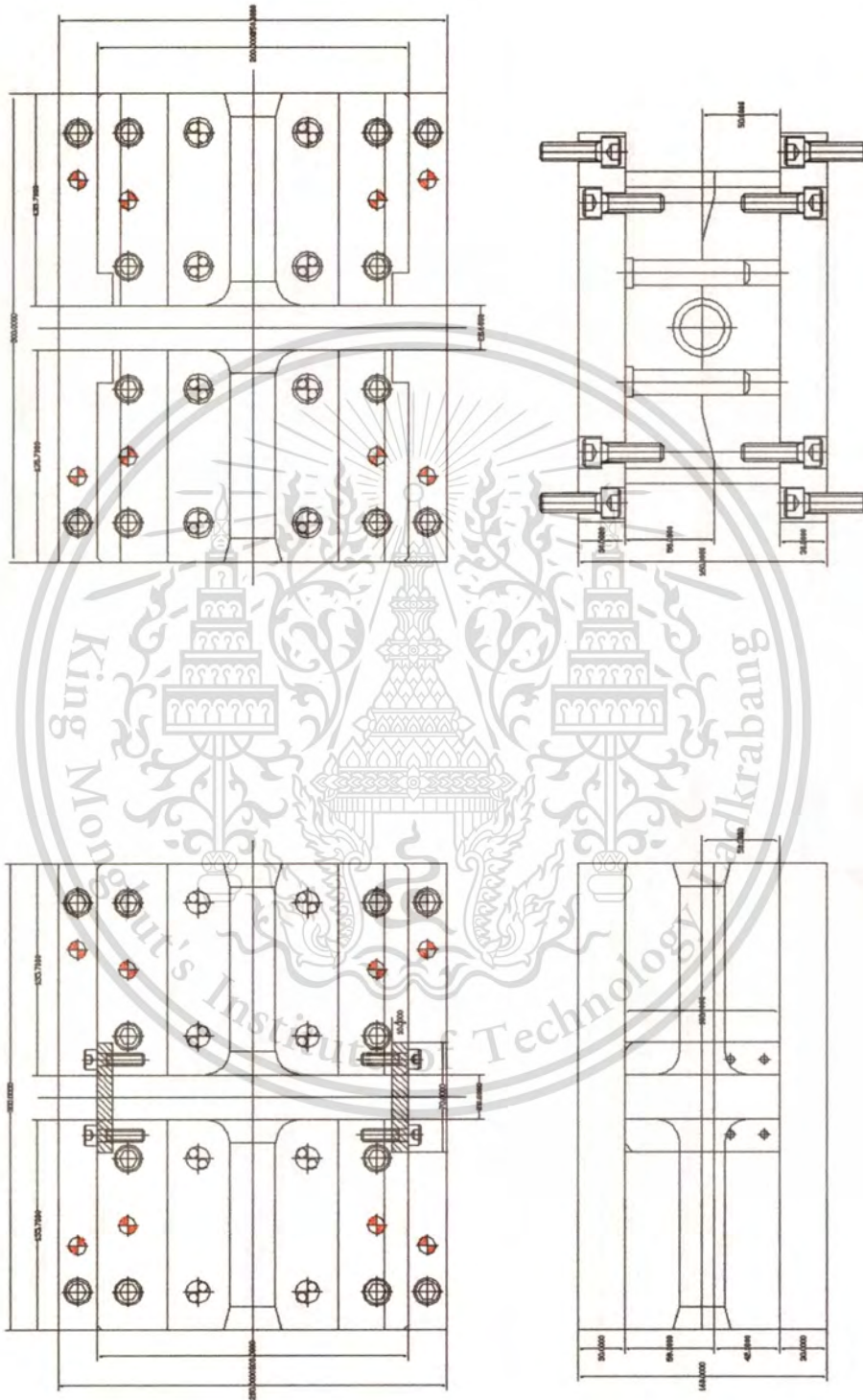
# APPENDIX C

## TOOLING SCHEMATIC

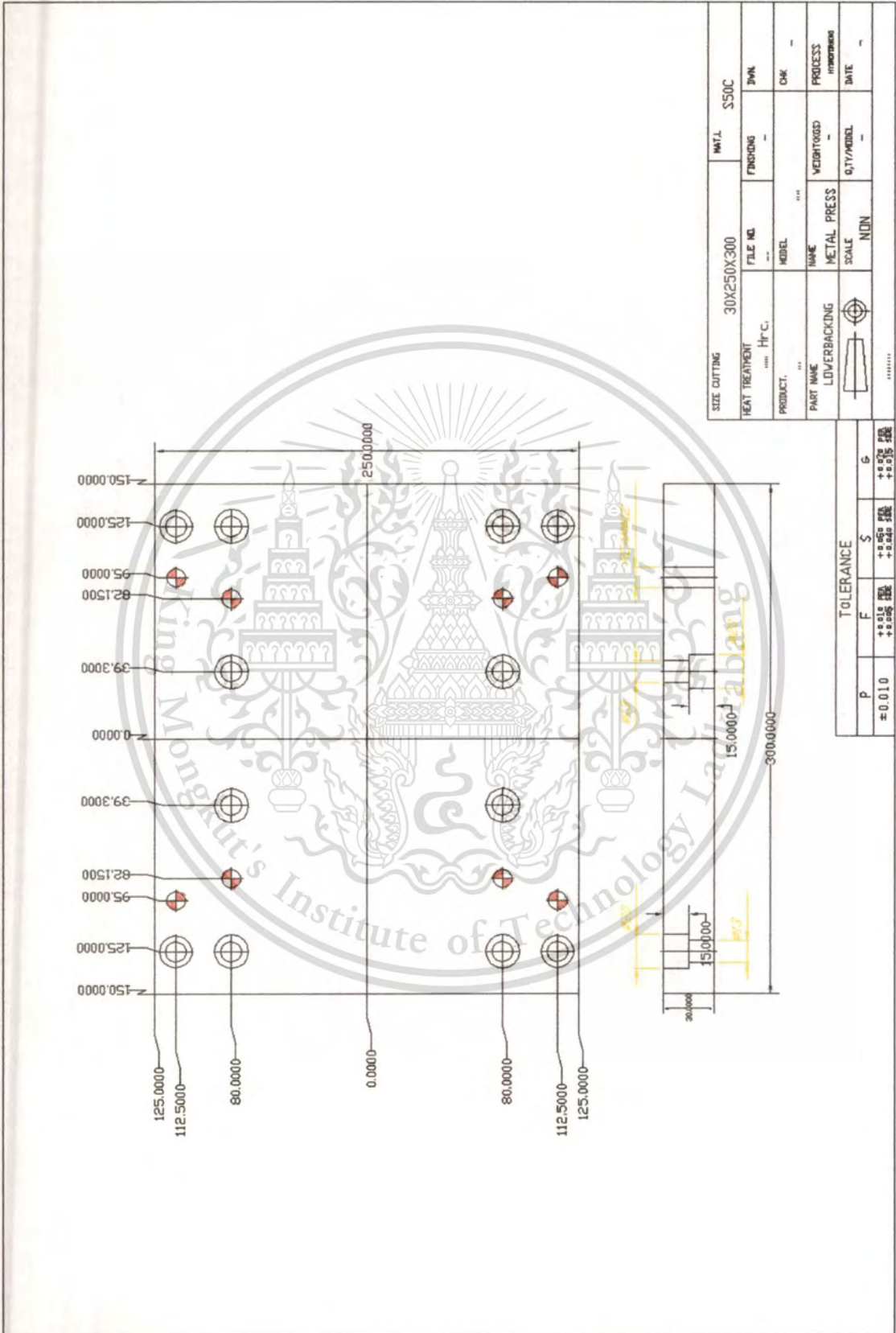


This material is reserved for educational use only, not allowed for commercial use.

Forbidden to modify the content, and cite the document when use.

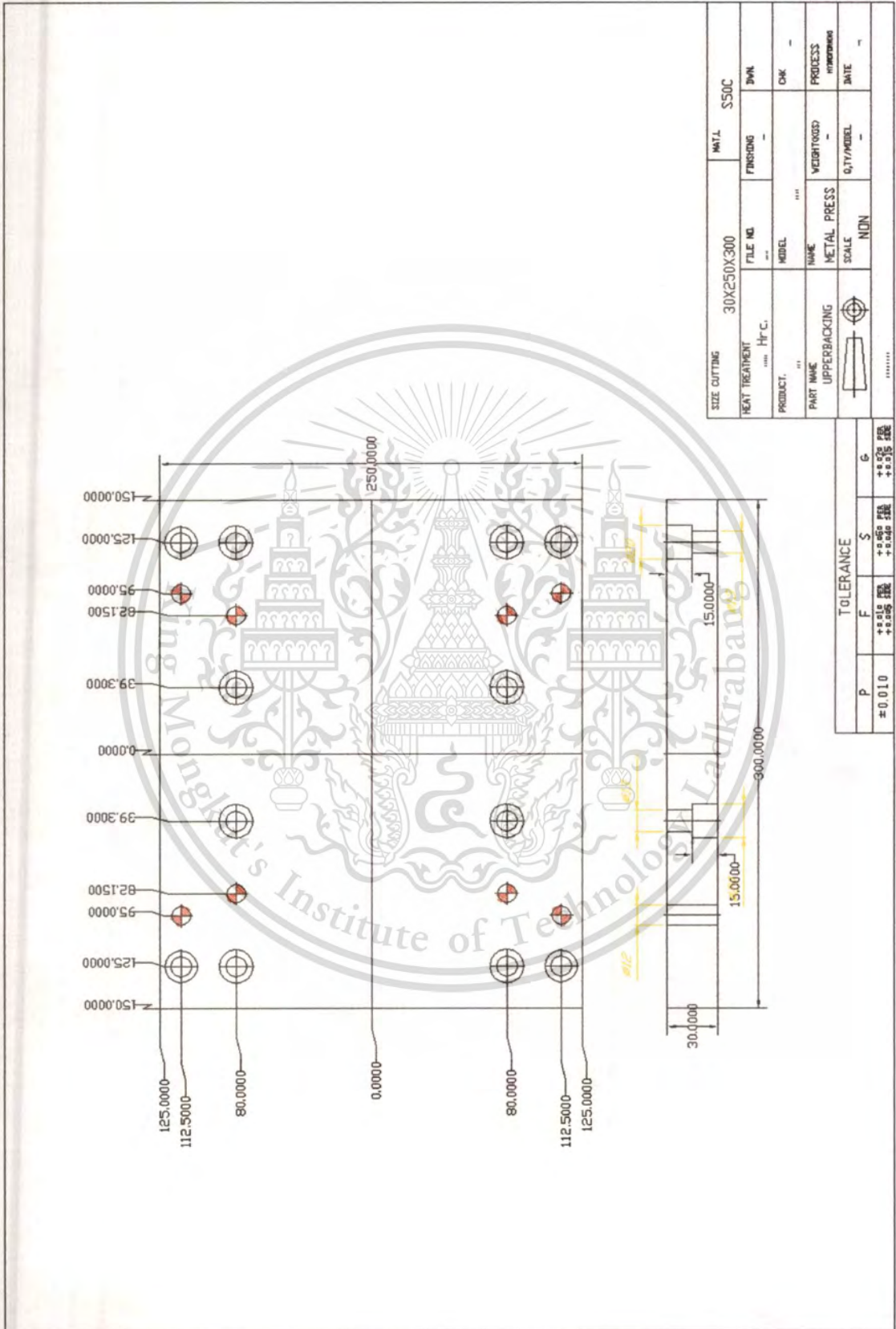


ASSEMBLY



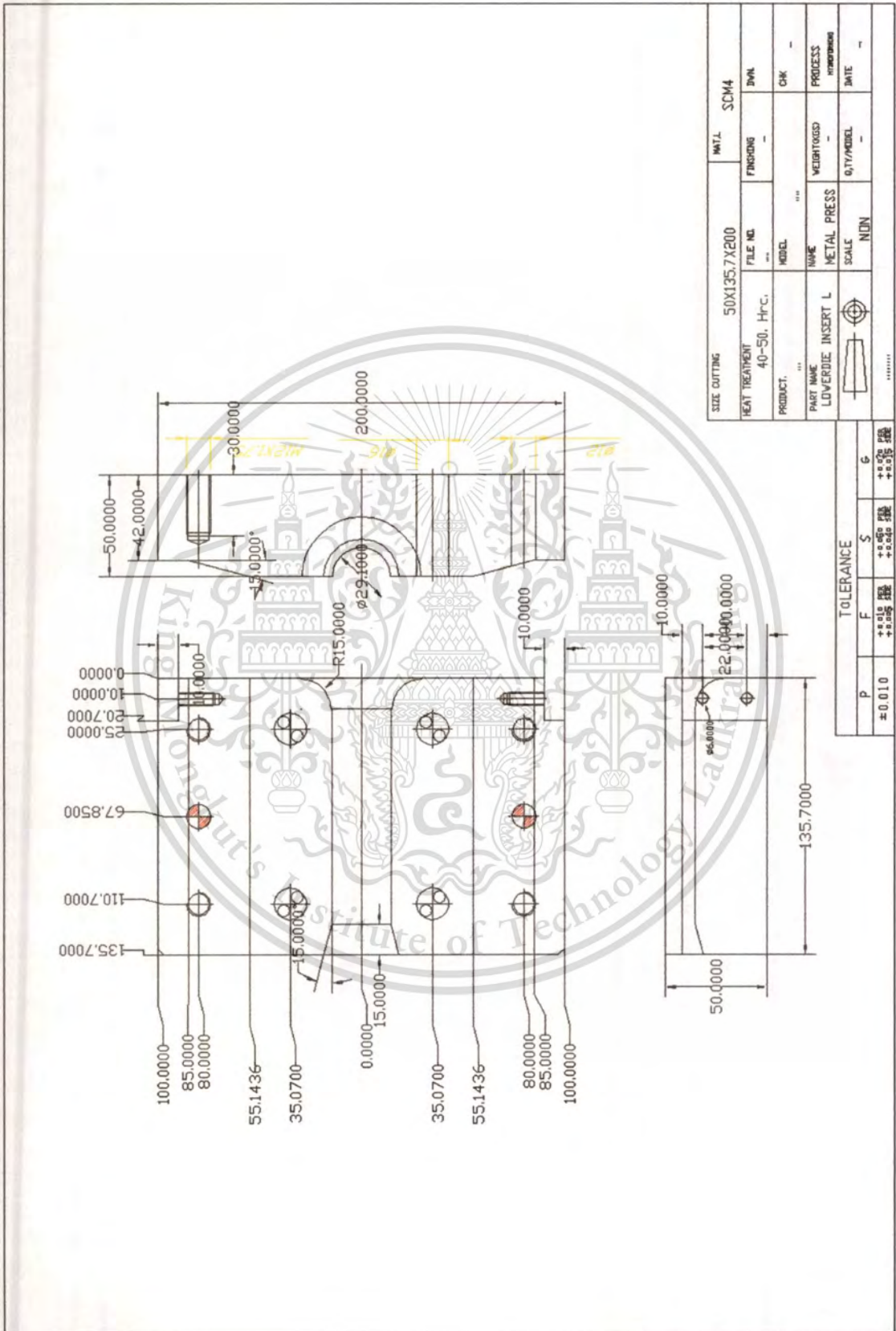
This material is reserved for educational use only, not allowed for commercial use.

Forbidden to modify the content, and cite the document when use.



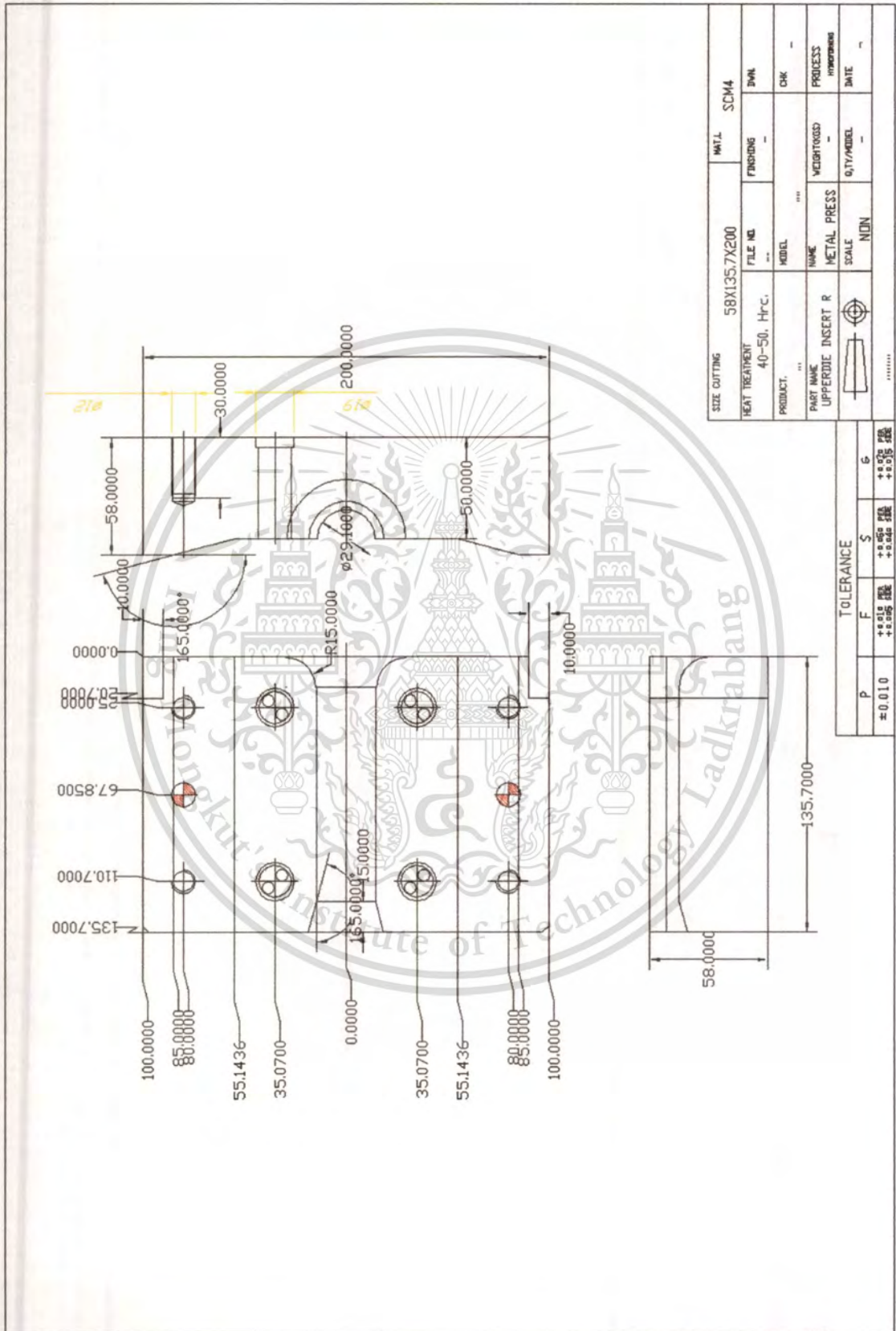
This material is reserved for educational use only, not allowed for commercial use.

Forbidden to modify the content, and cite the document when use.



This material is reserved for educational use only, not allowed for commercial use.

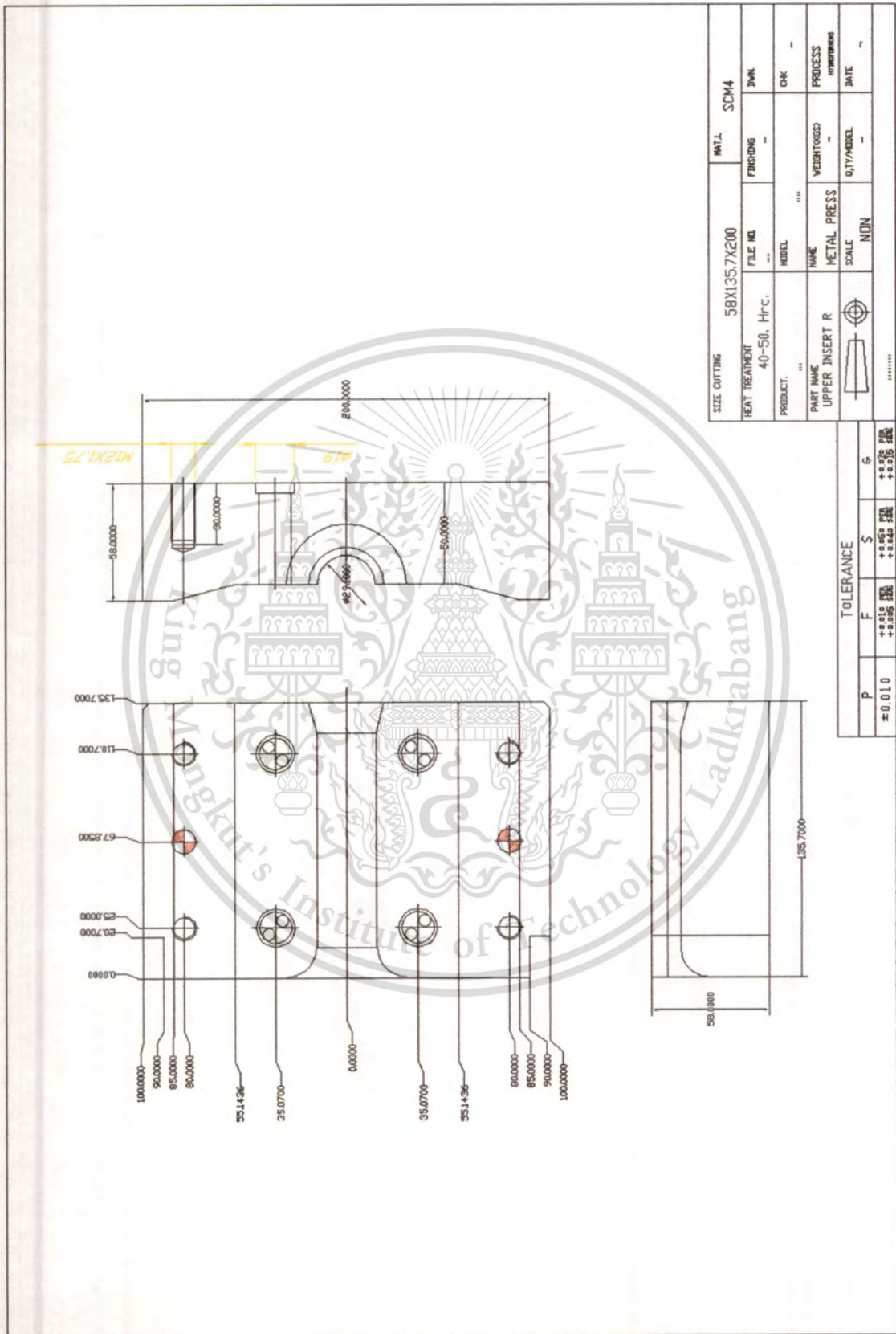
Forbidden to modify the content, and cite the document when use.



This material is reserved for educational use only, not allowed for commercial use.

Forbidden to modify the content, and cite the document when use.





This material is reserved for educational use only, not allowed for commercial use.

Forbidden to modify the content, and cite the document when use.

## BIOGRAPHY

- Name:** Mr. Ramil Kesvarakul
- Date of Birth:** November 1, 1983
- Place of Birth:** Bangkok, Thailand
- Education:**
- 2003 – 2007 B. Eng. in Industrial Engineering, Department of Industrial Engineering, Faculty of Engineering, King Mongkut's Institute of Technology Ladkrabang (KMITL)
- 2007 – 2010 M. Eng. in Automotive Engineering (International program), International College, King Mongkut's Institute of Technology Ladkrabang (KMITL)
- Scholarships:**
- 2007-2009 Full scholarship for study in the master degree from National Science and Technology Development Agency (NSTDA)
- Publications:**
- R. Kesvarakul, M. Pijmsam, S. Jirathearanat and N. Ohtake** "Determination of forming limit curves of tubular materials for hydroformability evaluation of automotive parts", Proceeding of the 3rd International Conference on Green and Sustainable Innovation 2009, Chiang Rai, Thailand, December 2<sup>nd</sup>-4<sup>th</sup>, 2009. pp 166.